Photothermal and Photoelectrical Energy Conversion in Plasmonic Nanostructures

By

Wei Li

Dissertation
Submitted to the Faculty of the
Graduate School of Vanderbilt University
in partial fulfillment of the requirements
for the degree of

DOCTOR OF PHILOSOPHY
in

Mechanical Engineering
May, 2016
Nashville, Tennessee

Approved:

Jason G. Valentine, Ph.D.

Deyu Li, Ph.D.

D. Greg Walker, Ph.D.

Sharon M. Weiss, Ph.D.

Richard F. Haglund Jr., Ph.D.

This thesis is dedicated to my parents

ACKNOWLEDGEMENTS

I would like to express the deepest appreciation to my advisor Prof. Jason Valentine. Without his guidance and persistent help this dissertation would not have been possible. When I joined the lab five years ago as a mechanical engineer, I was totally unfamiliar with nano-optics. Prof. Valentine has been a great mentor and has been patient in guiding me from learning fundamental concepts to tackling frontier challenges in the field. He taught me how to think critically and independently. And there are many things I'm stilling learning from him even after five years. Prof. Valentine has also been extremely supportive in my career development by sending me to many major conferences in the field, writing me many recommendation letters and providing me generous assistance in my postdoc applications. I will always be grateful for what he has taught me over the past five years.

I would also like to thank Prof. Deyu Li, Prof. Greg Walker, Prof. Sharon Weiss and Prof. Richard Haglund Jr. for not only serving on my dissertation committee. They have provided valuable feedback in the past years, steering my research in the right direction. I have also learned a lot from their classes and many of the knowledge have been extremely helpful in doing my research. I also want to thank Prof. Sharon Weiss for her generous help and being extremely supportive in my career development.

I want to thank all my labmates in Prof. Valentine's group for their support over past five years. In particular, I want to thank Zack Coppens for continuous help and encouragement during my time in the lab. As the two mechanical engineers in the lab, we have worked together on many great projects. The time with Zack discussing research, working in the cleanroom, building experimental setups, and doing measurements in the darkroom till midnight over the past few years have been unforgettable experiences to me. I also want to thank Parikshit Moitra, for always providing me assistance and advice on research. Outside the lab, doing darts, bowling and paintball with labmates together have been fun experiences in my graduate school life.

I want to thank all the department administrative assistants Suzanne Weiss, Myrtle Daniels and Jean Miller for helping me with registering for classes, purchasing orders, scheduling exams and many other things over the past years, especially Suzanne Weiss for helping me get my car when I needed it most. I also want to thank Dr. Anthony Hmelo, Dr. Bo Choi, Dr. Benjamin Schmidt and Dr. Robert Marvel for patiently training me on all kinds of experiment tools and providing me assistance in the cleanroom all the time.

Thanks to all my friends in Nashville for really spending some unforgettable time with me during my graduate school life. They have always been supportive even though most of them don’t know about my research. I want to thank Shuzhan, Longyun, Stanley, Minchun, Chunqing, Henry, Shuren and Kevin. We had a lot of fun time playing soccer together and wining the intramural champion has been a memorable moment. I also want to thank Chunqing, for practicing and running a Marathon with me. I also want to thank Tu for being a great roommate for over three years.

Finally, I want to thank my parents and Xueying. They have sacrificed so much so that I could pursue my dreams. Words cannot express how grateful I am for their unconditional love and support.

TABLE OF CONTENTS

Page

LIST OF FIGURES

LIST OF ABBREVIATIONS

AFM	Atomic Force Microscopy
BOE	Buffered Oxide Etchant
CD	Circular Dichroism
CMOS	Complementary Metal Oxide Semiconductor
CPL	Circularly Polarized Light
EBL	Electron Beam Lithography
FDTD	Finite Difference Time Domain
FWHM	Full Width at Half Maximum
IPA	Isopropyl Alcohol
ITO	Indium Tin Oxide
LCP	Left-handed Circularly Polarized
LH	Left-handed
LPL	Linearly Polarized Light
LSPR	Localized Surface Plasmon Resonances
MIBK	Methyl Isobutyl Ketone
MPA	Metamaterial Perfect Absorber
OPO	Optical Parametric Oscillator
PMMA	Poly(Methyl Methacrylate)
PMT	Photomultiplier Tube
RCP	Right-handed Circularly Polarized
RF	Radio Frequency
RH	Right-handed
RIE	Reactive Ion Etching
RMS	Root Mean Squared
SEM	Scanning Electron Microscopy
SPP	Surface Plasmon Polariton
TGP	Thermographic Phosphors
XPS	X-ray Photoelectron Spectroscopy
XRD	X-ray Diffraction

LIST OF PUBLICATIONS

Parts of this dissertation have been drawn from the following publications[1]–[5]**:**

1. **W. Li** and J. Valentine "Harvesting the Loss: Surface Plasmon-Based Hot Electron Photodetection" ***Nanophotonics*** (accepted)
2. **W. Li**, Z. Coppens, L. Besterio, W. Wang, A. Govorov and J. Valentine "Circularly Polarized Light Detection with Hot Electrons in Chiral Plasmonic Metamaterials," ***Nature Communications*** 6, 8379 (2015)
3. **W. Li** and J. Valentine "Metamaterial Perfect Absorber Based Hot Electron Photodetection," ***Nano Letters*** 14, 3510 (2014)
4. Z. Coppens†, **W. Li**†, G. Walker, and J. Valentine "Probing and Controlling Photothermal Heat Generation in Plasmonic Nanostructures," ***Nano Letters*** 13, 1023 (2013) (†: equally contributed first author).
5. **W. Li**, Z. Coppens, G. Walker, and J. Valentine "Electron Beam Physical Vapor Deposition of Thin Ruby Films For Remote Temperature Sensing," ***Journal of Applied Physics*** 113, 163509 (2013)

Chapter 1 Introduction

1.1 Surface Plasmons

Nobel metal nanoparticles possess intriguing optical properties causing the metal color to change with particle size. This phenomenon has been observed and utilized by human beings for thousands of years. Long before modern science, people have incorporated small metal particles into glass to create colorful stained glass windows and colorful goblets. The most notable example is the *Lycurgus cup*[6], a Roman goblet dating from the fourth century A.D. and now held in the British Museum (Fig. 1.1a). The Lycurgus cup absorbs and scatters blue and green light so that it shows a greenish hue when the white light is incident from the outside but appears red when the white light is placed inside the cup. Starting in the 1850s, the development of electromagnetic theory and experimental approaches have provided a physical understanding of the origin of this phenomenon[7]–[11], leading to the development of the research on surface plasmon polaritons. The research on surface plasmons, deemed plasmonics, has gathered an incredible amount of attention over the last few decades.

When an electromagnetic wave impinges on a sub-wavelength size metallic nanoparticle, the free electrons are coherently driven by the oscillating electric field and form a surface plasmon (Fig. 1.1b). As a result, strong resonances occur in the metal nanoparticles leading to sub-wavelength scale light confinement and strong scattering and absorption.

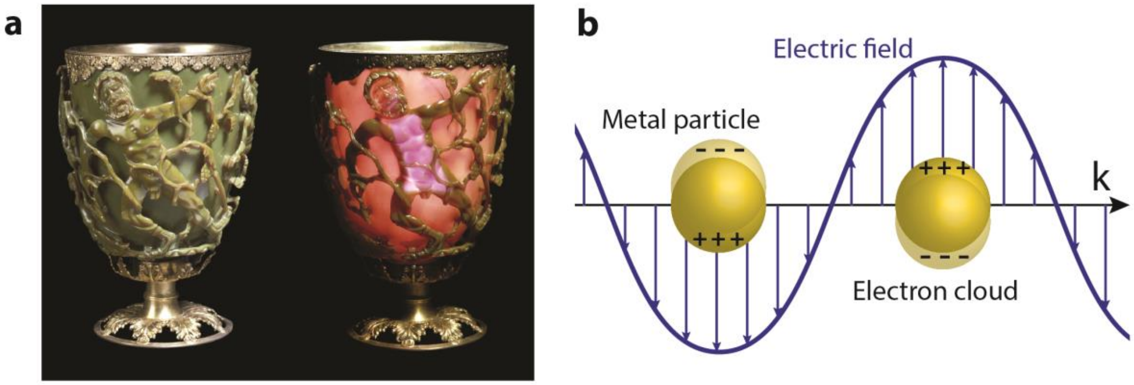

Figure 1.1. (a) The Lycurgus cup, appears green in reflected light but red in transmitted light. Pictures are obtained from the British Museum with permission. (b). Schematic of localized surface plasmon excitation in metallic nanoparticles.

Plasmon resonances can be tuned using the shape, size and surrounding medium of the particles. The development of nanoscale fabrication techniques have enabled scientists to precisely tailor, manipulate, and utilize plasmonic effects. Over the last decade, research on plasmonics has become a flourishing field[12]–[15] concerned with both a physical understanding of light-matter interaction at the nanoscale level and applications in nanoscale optics, on-chip photonics, sensing, and solar energy conversion systems.

1.2 Plasmonics: beyond the diffraction limit

Due to the ability to realize deep-subwavelength light confinement and enhancement of the optical near field, plasmonics provides a means to realize numerous techniques such as controlling light propagation, emission, concentration, and enhancing light-matter interaction at the nanoscale with numerous applications[16], [17] including metamaterials & metasurfaces[18], [19], sub-diffraction limited imaging[20], lasers[21], and cloaking[22]. Plasmonics could also be used to enhance the performance of photovoltaic devices[23], [24] , photodetectors and modulators[13], [25] and environmental sensors[26], [27]. For example, plasmonic nanostructures can be used as building blocks to create metamaterials with designer effective permittivity and permeability[18]. It has also been shown that the abrupt phase change provided by a plasmonic antenna gradient array known as metasurface can be utilized to control light bending and create ultracompact lenses and waveplates[19], [28]. On the other hand, combining a plasmonic Yagi-uda antenna and quantum dots provides a way to achieve directional light emission[29]. For light concentration, sub-diffraction-limit optical imaging has been demonstrated using a silver plasmonic superlens with a spatial resolution of one-sixth of the illumination wavelength[20]. Plasmonic bowtie antennae with feed gaps[30] can be utilized to create strong localized field enhancements and harmonic generation. The strong near field enhancement enabled by plasmonic antennae has also been demonstrated for trapping and manipulating nano-objects[31]. Plasmonics could also be used to enhance the performance of photovoltaic devices[23], photodetectors and modulators[13], [32], and environmental sensors[26].

1.3 Plasmon decay mechanism

As discussed in Section 1.1 of this chapter, surface plasmons are excited when coherent electron gas oscillations are formed in metallic nanoparticles. These electron gas oscillations can easily be damped and thus after a short existence the plasmon will start to decay. Following excitation, plasmons can either decay radiatively into re-emitted photons[33] or non-radiatively decay[34]–[36] via interband and intraband transitions, forming energetic hot electrons. An illustration of plasmon decay processes following excitation are shown in Fig. 1.2. The hot electrons will further thermalize through electron-phonon and electron-electron scattering and the energy is eventually transferred to heat.

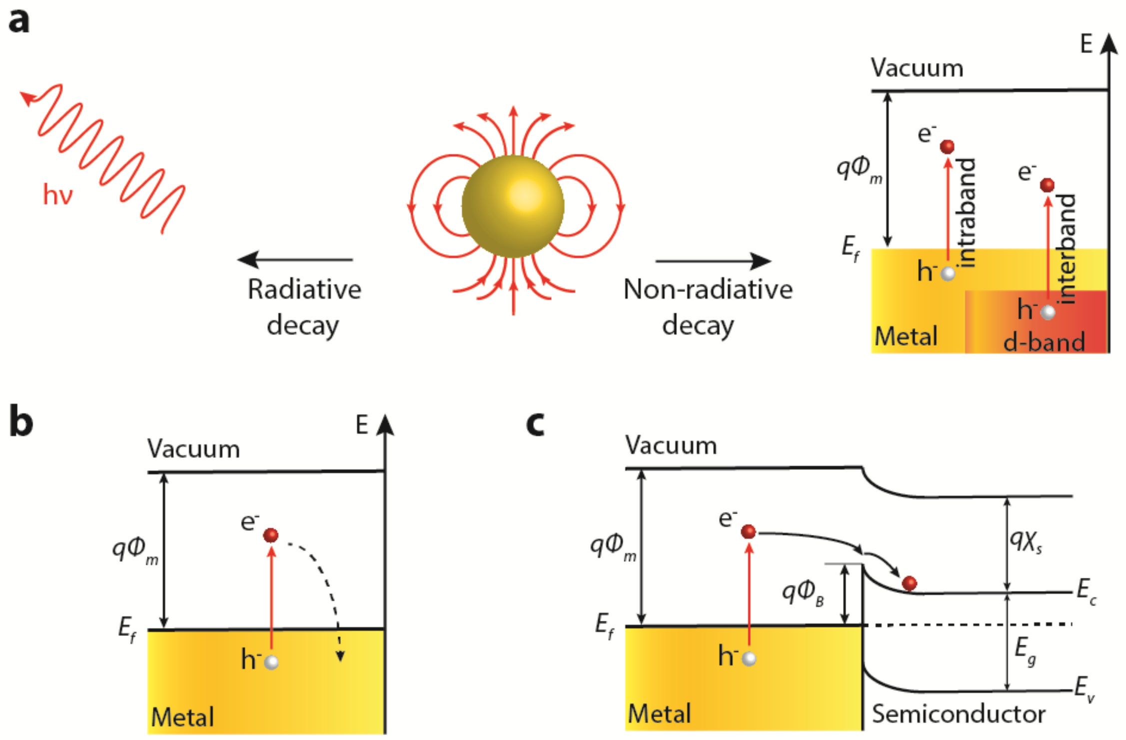

Figure 1.2. (a) Plasmon decay mechanism: the plasmon can either radiatively decay into re-emitted photons or non-radiatively decay into hot electrons. (b) Hot electrons can release their energy into thermal energy for photothermal heat generation. (c) Hot electrons can also be captured by a potential barrier such as Schottky barrier for photoelectrical conversion.

In almost all of the applications as discussed in Section 1.2, the non-radiative plasmon decay will serve as a parasitic process. For instance, in a plasmonic waveguide, the plasmon lifetime and surface plasmon propagation length will be hampered by the non-radiative plasmon decay. In plasmonic metamaterials the non-radiative decay process will lead to optical absorption in the metal and reduce the transmission or reflection. As a result, in recent years, a lot of work has been devoted to non-radiative plasmon decay mitigation such as finding alternative materials for noble metals as well as improving metal quality. However, recent research has discovered new and exciting opportunities to take advantage of surface plasmon non-radiative decay[37], [38] such as photothermal heat generation[4], [39], photovoltaic devices[12], [37], photocatalysis[40]–[42], driving material phase transitions[43], [44], photon energy conversion[45] and photodetection[2], [3], [46]–[50]. For instance, the decay of hot electrons can lead to local heating of the plasmonic nanostructures (Fig. 1.2b), making them candidates for nanoscale heat sources[4], [39] for use in cancer therapy[51], plasmonic nano-welding[52], and solar steam generation[53][54]. Understanding photothermal heat generation in plasmonic nanostructures is also important in designing near field transducers for heat-assisted magnetic recording techniques[55], [56]. On the other hand, hot electrons can be captured before thermalization by an adjacent semiconductor (Fig. 1.2c), providing a novel photoelectrical energy conversion scheme for photovoltaics or for driving chemical reactions[41], [42]. In this case, carriers excited with photon energies lower than the semiconductor bandgap can be captured, circumventing band gap limitations and opening pathways for additional energy harvesting.

1.4 Hot carrier physics

1.4.1 Internal photoemission

As discussed in Section 1.3 of this chapter, hot carriers generated in a metal can be collected by placing a semiconductor adjacent to the metal, forming a Schottky barrier. The hot carriers with energy greater than the Schottky barrier can flow into the semiconductor through an internal photoemission process, generating photocurrent. The very first attempt to quantitatively describe the photon-induced emission of electrons from metals was made by R. H. Fowler[57] in the 1930s. Later in the 1950s, the overall hot electron generation and collection process was described by W. E. Spicer with an intuitive three-step model[58], [59]: (1) hot electrons are generated in the metal through absorption of photons, (2) a portion of the hot electrons diffuse to the metal-semiconductor interface before thermalization, and (3) hot electrons with sufficient energy and the correct momentum are injected into the conduction band of the semiconductor through internal photoemission. Therefore, the efficiency of hot carrier devices depends on the initial hot carrier distribution, the transport of the carriers, as well as the carrier collection efficiency. Fowler's model is perhaps the most widely used description of hot electron injection and is based on a semi-classical model of hot electrons emitted over an energetic barrier, with the critical assumption that the photoexcited electrons in a metal have an isotropic momentum distribution and only the electrons within the momentum cone of the semiconductor can transport across the interface due to conservation of electron momentum. In the Fowler model the internal photoemission efficiency, η, is given by:

$$\eta = \frac{(\hbar\omega - \phi_b)^2}{4E_F\hbar\omega} \tag{1.1}$$

where $\hbar$ is the reduced Planck constant, ω is the photon frequency, E_F is the metal Fermi energy, and ϕ_b is the barrier height. The barrier height is determined by the work function of the metal and the electron affinity of the semiconductor but can be affected by the fabrication process employed. Experimentally measured Schottky barrier heights for numerous metals and semiconductors are presented in Table 1.1.

	Si	TiO_2	GaAs	Ge	CdSe	CdS
Au	0.8	1.0	1.05	0.59	0.7	0.8

Ag	0.83	0.91	1.03	0.54	0.43	0.56
Al	0.81	Ohmic	0.93	0.48	N/A	N/A
Ti	0.5	Ohmic	0.84	0.53	N/A	0.84
Cu	0.8	0.85	1.08	0.5	0.33	0.5
Pt	0.9	0.73	0.98	0.65	0.37	1.1
Cr	0.6	0.88	0.82	0.59	N/A	N/A

Table 1.1. Experimental reported Schottky barrier height ϕ_b (eV) for typical plasmonic materials on an n-type semiconductor. Data adapted from Refs. [46], [49], [60]–[67]. For p-type semiconductors the barrier height can be estimated by subtracting the value from the bandgap energy of the semiconductor.

In contrast with the electron-hole pair generation in semiconductors, the efficiency given by equation 1.1 predicts an increasing quantum yield at higher photon energy and many recently demonstrated hot electron photodetectors based on Schottky barriers have been shown to follow this model[3], [46], [68]. Compared with electron-hole generation and separation in a semiconductor, the internal photoemission in a bulk metal/semiconductor Schottky junction is a very inefficient process. This is mainly due to: (1) poor light absorption, (2) a broad hot electron energy distribution[69], and (3) an isotropic hot electron momentum distribution. Surface plasmons can potentially boost the efficiency of hot electron collection by addressing these issues. Plasmonic nanoparticles have an absorption cross-section much larger than the physical size of the particles[70], yielding much more efficient hot electron generation than bulk metal. Plasmonic nanoparticles also produce hot carriers at a higher average energy compared with bulk metal[71]–[74]. Lastly, the momentum distribution of hot carriers can be modified by engineering the modes of the plasmonic structures. Therefore, surface plasmons provide a powerful tool for efficient hot electron generation and extraction.

1.4.2 Hot carrier generation

Understanding initial hot electron generation and distribution, before inelastic relaxation, is critical to estimating the overall hot carrier injection efficiency. During non-radiative plasmon decay, hot electron-hole pairs are created through Landau damping on a time scale of femtoseconds[75]. Theoretical calculations of hot electron energy distribution in bulk metal, based on the electron density of states approximated by a free electron gas model, shows a broad continuous distribution of hot electron energies upon excitation[69]. This broad hot electron energy distribution sets an impediment for realizing high efficiency in the internal photoemission process as many carriers will have an energy that is below the Schottky barrier[69]. In contrast with bulk metals, it has been shown that the hot carrier energy distribution in plasmonic nanoparticles can potentially be narrowband[72]–[74], [76], [77] and is strongly dependent on the particle size[73], [74] and geometry[76]. For instance, hot carriers are more efficiently generated in small plasmonic nanoparticles compared to large ones[73]. Nanoparticle geometry including shape[76] and aspect ratio[78] also play an important role in determining the hot carrier generation and injection due to carrier confinement and surface scattering[76]. In addition, a theoretical model for the hot carrier generation process has been developed using Fermi's golden rule where the conduction electrons are described as free particles in a confined potential wall[72]. This model predicts that both the production rate and the energy distribution of the hot carriers are strongly dependent on the particle size and hot carrier lifetime. In addition to energy distribution, the hot carrier momentum distribution is also an important factor. Hot carriers are primarily generated with momentum parallel to the external field[72], which is generally parallel with the semiconductor interface in the case of an antenna, resulting in poor injection. Moreover, hot electron generation is also dependent on the plasmonic material employed[79], [77], [80], [81]. Several groups have explored the effects of the electronic structure of the metal on the generated carrier distributions[79], [80] and it has been shown that in the interband transition regime the electronic band structure of the metal plays an important role on both the energy and momentum distribution of the generated hot carriers[79]. In fact, in this regime none of the commonly used plasmonic materials including gold, silver, aluminum and copper exhibit the isotropic momentum distribution assumed in the Fowler theory[79]. Additionally, the effects of phonons and surfaces on hot carriers have also been studied[82]. Therefore, one needs to take plasmonic nanostructure geometry, size, excitation condition, hot carrier lifetime as well as material electronic band structure into account when optimizing hot carrier device efficiency.

1.5 Organization of the Thesis

In this thesis, I will present my efforts to demonstrate how plasmonic nanostructures can be engineered to take full advantage of the non-radiative plasmon decay process to enhance the efficiency of photothermal heating and photoelectrical energy conversion systems[1]–[5]. In particular,

Chapter 2 introduces design rationale of how plasmonic nanoparticles can be designed for nanoscale photothermal heat generation. I will also discuss the development of a nanoscale thermal microscopy technique based on thin film thermographic phosphors[4], [5] and how we use it to experimentally validate the proposed design rationale.

In **Chapter 3**, I will discuss how plasmon energy can be harnessed in the form of hot electrons for photoelectric conversion and photovoltaic applications. I detail an experimental demonstration of how hot electron device efficiencies can be greatly enhanced by the proposed metamaterial perfect absorber designs[3].

Chapter 4 demonstrates how one can realize an ultracompact circularly polarized light detector by combining the giant circular dichroism in chiral metamaterials with hot electron injection. I will also discuss how to design planar chiral metamaterial with near perfect circular dichroism[2].

Finally, **Chapter 5** summarizes the highlights of this work and its long-term implications. The future opportunities and challenges in harvesting plasmonic hot electrons will also be discussed.

Chapter 2 Probing and Controlling Photothermal Heat Generation in Plasmonic Nanostructures

2.1 Introduction to Thermoplasmonics

The ability of surface plasmons to confine electromagnetic energy in deep sub-wavelength volumes has attracted much attention in nanoscale science due to the large local electromagnetic fields that are generated. However, one of the drawbacks associated with surface plasmons is that the resistive heat loss within the metal structures can often limit device performance. While much effort has been devoted to minimizing this heat loss, in the emerging field of thermoplasmonics the focus has shifted toward engineering the loss to design optically-induced, nanoscale thermal sources[83]–[86]. Focusing electromagnetic energy down to nanoscale volumes results in high temperature thermal hot spots that can be used in a variety of applications including chemical catalysis[87]–[89], heat-assisted magnetic recording[55], [56], phononic circuitry[90], and medical therapy[51], [91], [92].

Currently there are two major challenges in the field of thermoplasmonics: particle design and micro/nanoscale temperature measurement. Current work in particle design has focused on understanding the thermal response of structures such as spheres, disks, core-shell structures, and rods[83]–[86], [93]. In order to fully exploit the potential of thermoplasmonics, a better understanding is needed of how more complex geometries can be used to control the magnitude of heat generation in plasmonic nanostructures. Furthermore, current work in thermoplasmonic temperature characterization has shown many promising approaches, yet a robust thermal imaging technique is still lacking. Existing techniques rely on near-field methods, such as scanning thermal microscopy[94], and far-field methods such as thermally induced refractive index change[95], Raman spectra[96], fluorescence emission[97], and polarization anisotropy[98]. However, near-field methods are inherently invasive and the far-field methods suffer from either complex calibration procedures or sensitivity to factors such a thermally induced diffusion or excitation intensity fluctuation.

In this chapter we present a thermoplasmonic design rationale that demonstrates how good electromagnetic plasmonic antennae can be converted into good thermoplasmonic antennae with large heat source density through increasing the current density within the antenna. We also develop a far-field thermal microscopy technique using thin-film thermographic phosphors (TGP) to validate our thermoplasmonic design rationale. This microscopy method utilizes temperature sensitive decay lifetime as the sensing technique and uses a solid sensing material (phosphor) making it robust against intensity fluctuations and artifacts due to high surface temperatures. The demonstrated thermoplasmonic design rationale and TGP microscopy technique offer promising tools for the further advancement of thermoplasmonic devices and applications.

2.2 Proposed Thermoplasmonic Design Rationale

Heat generation in thermoplasmonic structures is governed by Joule heating, with the heat source density (q'''[W/m^3]) given by, $q''' = \vec{E} \cdot \vec{J}$, where $\vec{E}$ is the electric field and $\vec{J}$ is the current density. This equation is most commonly expressed as a function of the incident electric field and imaginary part of the permittivity function as $q''' = \omega \varepsilon_0 Im(\varepsilon_m) \left|\vec{E}(r)\right|^2$ where ω is the angular frequency and ε_m is the permittivity of the metal[83], [85], [86]. However, in plasmonic antennae exhibiting highly localized electric fields, such as those with feed gaps, the maximum electric field intensity occurs outside the metal surface in the surrounding medium. In this case, if the surrounding medium is transparent then designing the antenna to have large local electric fields does not necessarily imply large heat source density[84], [85]. Instead we can express heat source density in terms of the current density inside the metal, which can be done using Ohm's Law, $q''' = \left|\vec{J}\right|^2/\sigma$, where σ is the electrical conductivity of the metal.

As dictated by Ohm's Law, optimizing the current density in plasmonic antennae will lead to large heat source densities. However, for most antenna design applications, controlling fields rather than current densities is perhaps more intuitive. To show how the magnetic field is related to current density, we use Ampere's law to describe current density as, $\vec{J} = \vec{\nabla} \times \vec{H}$, where $\vec{H}$ is the magnetic field. Inserting the relationship for current density into Ohm's Law allows us to express the heat source density as a function of magnetic field, $q''' = \left|\vec{\nabla} \times \vec{H}\right|^2/\sigma$. If $\vec{J}$ is one dimensional, the only component of $\vec{H}$ is the rotational magnetic field, H_θ, and therefore,

$$q''' \propto H_\theta^2 \tag{2.1}$$

The proportionality of equation 2.1 shows that enhancing the magnetic field around a nanostructure can significantly increase heat generation inside the metal. This approach provides a general guideline for designing thermoplasmonic structures in which absorption is dominated by Ohmic loss in the metal.

Different studies have shown that the magnetic field of a nanoantenna can be greatly enhanced by using the complementary configuration of a feed gap antenna[99], [100]. Based on Babinet's principle, if a structure has its metal and dielectric regions inverted and is excited with a polarization that is rotated by 90°, a complementary optical response can be expected. While this principle is rigorously valid only for perfect electrical conductors, the main features of the response are still preserved at optical frequencies where metals are no longer perfect. Following this logic, a bowtie shaped feed gap antenna, which greatly enhances the electric field through capacitive effects across its gap, can be inverted to create a diabolo antenna. This alternative structure enhances the magnetic field through charge funneling in its neck region[99], [100]. The configuration is illustrated in Fig. 2.1a-d, which shows the complementary bowtie and diabolo structures and the corresponding electric and magnetic field distributions directly above their surfaces.

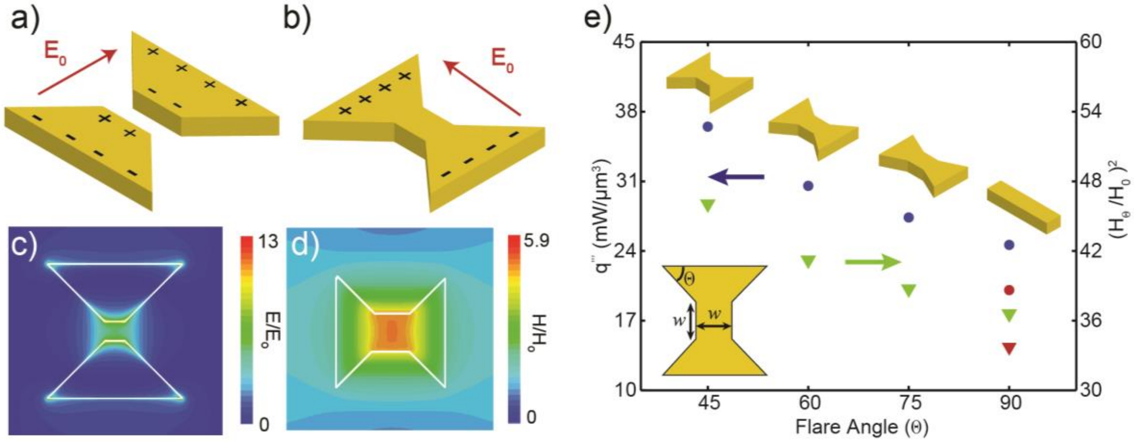

Figure 2.1. (a). Complementary antenna structures: bowtie (a) and diabolo (b) with plots of their electric (c) and magnetic (d) fields, respectively. (e) Evolution in geometry from dipole to diabolo antenna (w=50 nm). Magnetic fields were normalized to the incoming field intensity and each structure was made of gold and simulated on an Al_2O_3 substrate.

Using the diabolo structure as a reference, the proposed thermoplasmonic design rationale of equation 2.1 was tested against other antenna designs with lesser magnetic field enhancements. In Fig. 2.1e we show the simulated optical and thermal response for an evolution in nanoantenna geometries from the diabolo antenna (flare angle: 45°) to a dipole antenna (flare angle: 90°). The progressively smaller flare angle of each geometry funnels more charge through each structure's neck region, an effect that increases current density ($\vec{J}$) and rotational magnetic field (H_θ). The simulated H_θ and q''' values were collected at 5 nm above and 6 nm inside each structure, respectively. The results presented in Fig. 2.1e follow the relationship of equation 2.1, thus verifying the proposed thermoplasmonic design rationale. Furthermore, while illustrated here for the diabolo and bow-tie antennae, this approach can be applied for any feed gap based antenna to maximize heat generation within the structure.

For each structure in Figure 1e, the neck dimension (w), resonant wavelength (1064 nm), and input intensity (0.42 mW/μm^2) were held constant to isolate the effects to the varying flare angle. Consequently, equal volumes for each structure could not be maintained. To show that the increase in heat source density was not due to any volumetric effects, a dipole antenna with the same volume, resonant wavelength, and input intensity as the diabolo antenna was simulated. The results show that the dipole structure with the same volume (red markers in Fig. 2.1e) has both a decreased magnetic field and heat source density, confirming that the enhanced heating effect is not volumetric and in fact comes from carefully engineering the antenna's shape.

2.3 Thin Film Thermographic Phosphor

Because heat source density is proportional to temperature through the heat diffusion equation, we were able to experimentally validate the proposed thermoplasmonic design rationale by measuring the temperature of optically heated dipole and diabolo nanoantenna arrays. To measure the temperature of the plasmonic nanostructures, we developed a thermal microscopy technique utilizing TGPs as the temperature-sensing medium. TGPs are metal-doped ceramic materials whose photoluminescence decay time is temperature dependent[101]. These materials have long been used to probe temperatures using non-invasive optical probing and are typically used in environments with moving surfaces, high temperatures, or where thermocouple attachment is difficult[101], [102]. Because TGP temperatures are correlated with decay times, the measurement is insensitive to excitation intensity fluctuations and emitter concentration variation[103]. Also, due to the fact that the TGP is in a solid state and has a high melting temperature, large temperature ranges can be probed. In fact, phosphors of varying composition can be used to achieve temperature sensitivity from near 0 K to 1800 K[101]. Both of these aspects make the TGP temperature measurement method attractive for robust thermal microscopy.

To use TGP for measuring the temperature of plasmonic nanostructures, we deposited a thin film of TGP as the sensing layer. We then built the diabolo and dipole nanoantenna arrays directly on top of the thin TGP film, allowing for increased accuracy of the temperature measurement due to the phosphor layer's close proximity to the antenna.

2.3.1 Thin ruby film fabrication

Here we focus on thin film deposition of ruby, which consists of an aluminum oxide (Al_2O_3) host lattice and chromium (Cr) dopants as an activator. Ruby has played an important role as an active laser medium, and bulk ruby has been widely studied as a thermal sensing material[104]–[106]. Some of ruby's characteristic properties include a relatively long photoluminescence lifetime (3.5ms at room temperature[107]), visible excitation (532nm) and emission (694.4nm, 692.9nm), stability at high temperature (melting point 2317K[108]) and a large temperature sensitivity range (0K-813K[102], [109]).

To fabricate the thin ruby film, the source material for electron beam evaporation (ruby powder) was first prepared by a combustion synthesis process[110]. 3.0030g urea CH_4N_2O, 7.4278g aluminum nitrate $Al(NO_3)_3 \cdot 9H_2O$ and 0.0800g chromium nitrate $Cr(NO_3)_3 \cdot 9H_2O$ were dissolved in 5mL water in a cylindrical ceramic crucible. The chromium/aluminum ratio in reactant is set to 1.1% to achieve the strongest photoluminescence[111]. The crucible was placed on a hotplate at 350K and stirred for 5h until a green-colored gel formed, upon which it was placed in a furnace at 873K for combustion synthesis. The gel mixture combusted in about 2 minutes and resulted in a light pink-colored foam occupying the whole crucible. A post-synthesis calcine step was then performed to form a solid evaporation source by placing the crucible in a furnace at 1173K for 2h. Ruby powder was obtained by crushing this foam after cooling.

The ruby powder was used as the source material for electron beam evaporation (Angstrom Amod) of the ruby thin films. After first melting the powder using a low beam current, the power of the beam was slowly increased to reach a deposition rate of 0.2A/s, resulting in a film with minimal surface roughness. Ruby thin films with 100nm and 600nm thickness were deposited on transparent sapphire and fused silica substrates, and after deposition the films were transparent and exhibited weak photoluminescence. To improve the quantum yield of the thin ruby films, a thermal annealing process was performed by heating the as-deposited thin films in a furnace at 1373K for 2h. The thermal annealing process crystallizes the film, which is initially amorphous after electron beam evaporation. After the annealing process, films on the fused silica substrate became translucent while films on the sapphire substrate remained transparent. The photoluminescence intensity of the annealed films was also significantly improved compared with as-deposited films due to improved crystallinity. In the following sections, we examine in detail the ruby film morphology, composition, crystallinity and photoluminescence intensity and lifetime.

2.3.2 Thin ruby film morphology characterization

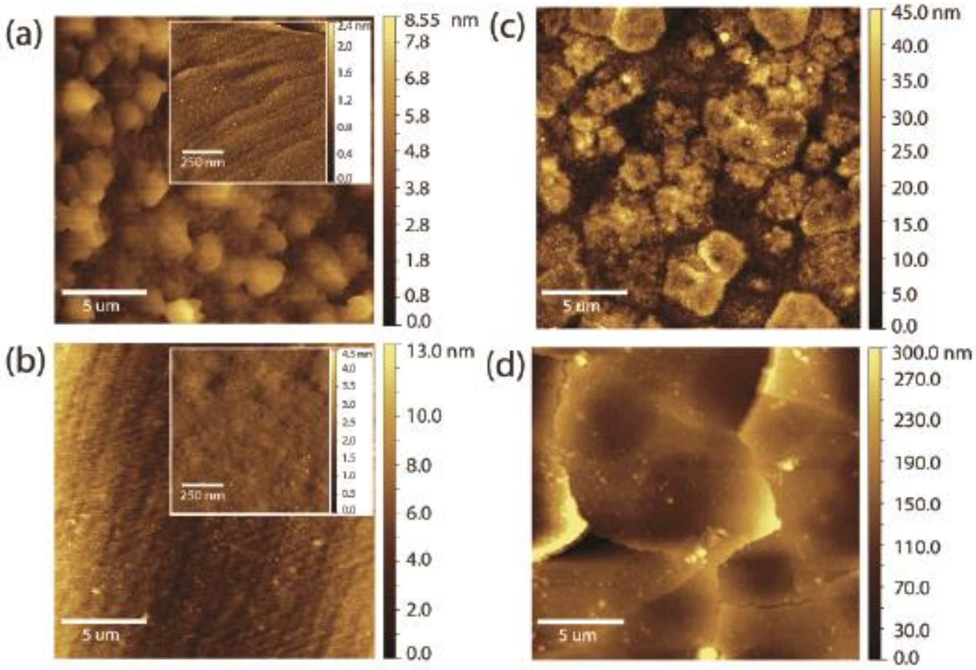

Figure 2.2. (a)-(d), AFM image of annealed ruby films. (a) 100nm film on sapphire, inset is a 1μm x 1 μm scan area, (b) 100nm film on fused silica, inset is a 1μm x 1 μm scan area, (c) 600nm film on sapphire, (d) 600nm film on fused silica.

Producing a high quality film is essential for the realization of a temperature probing platform for micro and nanoscale structures. The surface morphology of annealed ruby films measured with atomic force microscopy (AFM) is shown Fig. 2.2 Both 100nm and 600nm thick ruby films deposited on sapphire and fused silica substrates were inspected. In Fig. 2.2a, for the 100nm film deposited on the sapphire substrate, a grainy film with average feature size about 2μm is obtained. The roughness is due to the formation of polycrystalline islands during film growth[112], features similar to those found in previously studied polycrystalline α-Al_2O_3 films[113]. Root mean squared (RMS) surface roughness R_q is calculated as R_q=2.35 nm for the 100 nm thick film based on the AFM data. The low surface roughness film provides the capability for remote temperature sensing of micro/nano structures built on top of this film. For comparison, surface morphology of 100 nm films deposited on fused silica was also investigated (see Fig. 2.2b, R_q=2.20 nm). No obvious crystalline features can be observed, which lead to a smooth but weakly crystalized film. As a result, this film exhibits a much weaker photoluminescence intensity compared with the film on sapphire, which will be discussed later.

In the 600 nm thick ruby film on fused silica, it can be observed in Fig 2.2d that significant cracking occurs after the thermal annealing process. These cracks can also be confirmed by dark-field microscopy and illustrate why the films become translucent compared with the transparent as-deposited film. The cracking is due to the thermal expansion coefficient mismatch between the ruby film and fused silica. However, for the 600 nm thick film on sapphire (Fig. 2.2c), a continuous polycrystalline film is obtained due to thermal expansion match between the substrate and film. In addition to the smooth film, the lattice match between sapphire and α-Al_2O_3 also promotes the crystallization process resulting in strong photoluminescence, which will be discussed in Section 2.3.5.

2.3.3 Thin ruby film chemical composition characterization

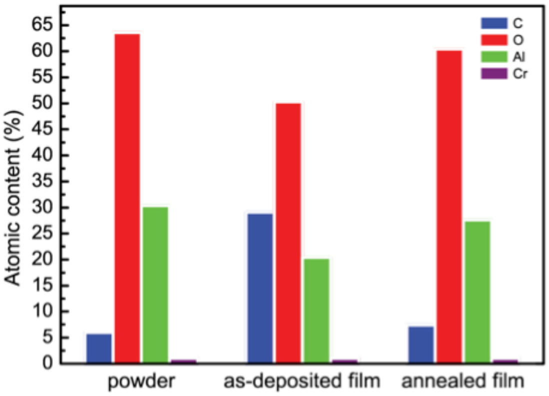

Figure 2.3. Chemical composition of synthesized powder, 100nm as-deposited film, and annealed film on a sapphire substrate.

Maintaining the stoichiometry and crystallinity of thin films compared with the source material is usually challenging during deposition processes. To gain an understanding of the stoichiometry variation during the film fabrication process, X-ray photoelectron spectroscopy (XPS) was used to analyze the composition of the synthesized powder, as-deposited films, and annealed films (Fig. 2.3). The synthesized powder has 6% carbon, 63.6% oxygen, and 30.4% aluminum and the as-deposited film shows similar composition with the exception of a significant amount of carbon (29.1%), which can be explained as contamination from the graphite crucible used during evaporation. However, the high carbon content in the as-deposited film is significantly reduced by the thermal annealing process resulting in the stoichiometry chemical composition of the annealed film being in close agreement with the ruby powder. The atomic percentage of chromium in the powder and films cannot be detected due to the sensitivity limitation of the XPS tool used. However, since strong photoluminescence is found in both the powder and annealed film, we assume that the chromium/aluminum ratio is in the range between 0.5% and 1% [111]. Also, in both the powder and the annealed film, the aluminum-to-oxygen ratio is lower than the expected ratio for Al_2O_3 (0.67), likely due to additional oxygen being partially bonded to the residual carbon atoms[114].

2.3.4 Thin ruby film crystal structure characterization

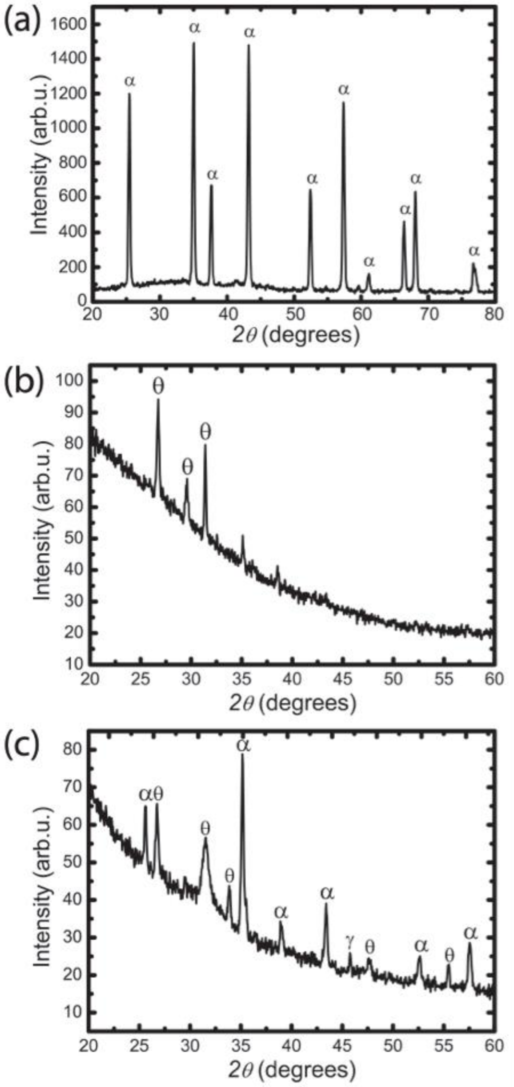

Figure 2.4. X-ray diffraction pattern of (a) synthesized powder, (b) as-deposited film and (c) annealed film. The films correspond to those deposited on sapphire.

X-ray diffraction (XRD) was used to acquire the crystal structure of the synthesized powder, as-deposited film on sapphire, and annealed film on sapphire to gain a better understanding of the role of crystallinity in dictating the photoluminescence properties of the films. As observed in Fig. 2.4, the synthesized powder shows a diffraction pattern corresponding to α-Al_2O_3[115] while the as-deposited film shows a mainly amorphous state with a few θ -Al_2O_3 peaks. While some of the θ-phase peaks are still present in the annealed film, the diffraction pattern is dominated by α-Al_2O_3. As shown in Fig. 2.4, recovering the α-Al_2O_3 is critical to preserving films with strong photoluminescence, which will be discussed in Section 2.3.5.

2.3.5 Thin ruby film photoluminescence characterization

To investigate the photoluminescence properties of thin ruby films, the samples were imaged using an optical microscope (Zeiss Axio Observer A1m) and excited with a 532nm laser modulated at 19Hz. A 50X objective is used to focus the excitation laser onto the film and to collect the emitted photons. Using the microscope allows higher excitation intensity with low laser power, increases the emission collection efficiency, and provides the capability to probe the local temperature in the excited area. The emitted photons are measured with a photomultiplier tube (PMT) with an emission band-pass filter and the time-dependent electric signal, which is proportional to the emission intensity, is recorded by a high-speed digitizer (Agilent, Model U1069A, 2Gs/s), which also reads the triggering signal from the chopper. The photoluminescence spectrum of synthesized powder, 100nm as-deposited film and annealed film on sapphire substrate are shown in Fig. 2.5.

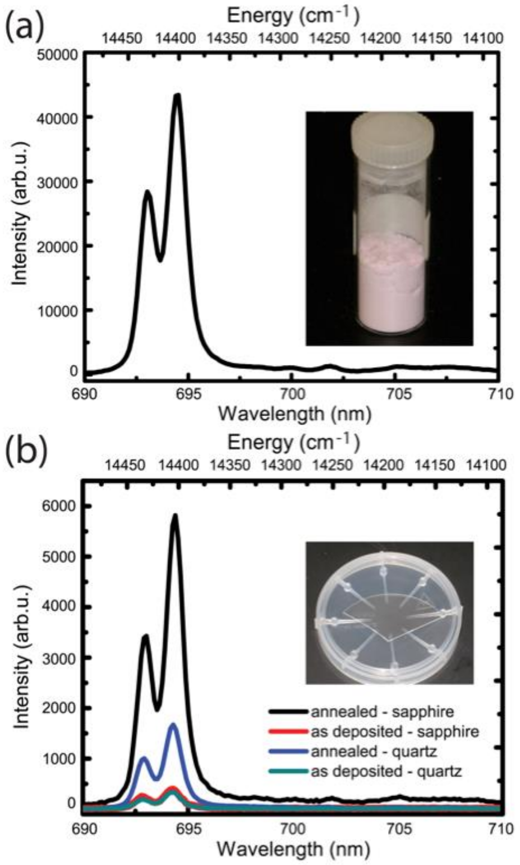

Figure 2.5. Photoluminescence spectra of (a) synthesized powder, (inset shows a photograph of ruby powder), (b) 100nm as-deposited and annealed films on sapphire and fused silica substrates, (inset shows a photograph of a transparent annealed film on a sapphire substrate).

Two ruby emission peaks (R1 line=694.4nm, R2 line=692.9nm) are found in photoluminescence spectra of the synthesized powder and films and are identical to the luminescence peaks in bulk ruby. Furthermore, the intensity of the annealed film is greatly enhanced compared with the as-deposited film. This observation further supports the XRD results that the chromium doped α-Al_2O_3 phase is dominant in the annealed films, yielding strong fluorescence. As a comparison, the photoluminescence intensity of films with the same thickness on a fused silica substrate is also given in Fig. 2.5b. Films on sapphire substrates can produce a stronger photoluminescence, which further confirms the necessity to use the lattice-matched substrate to ensure good crystal growth.

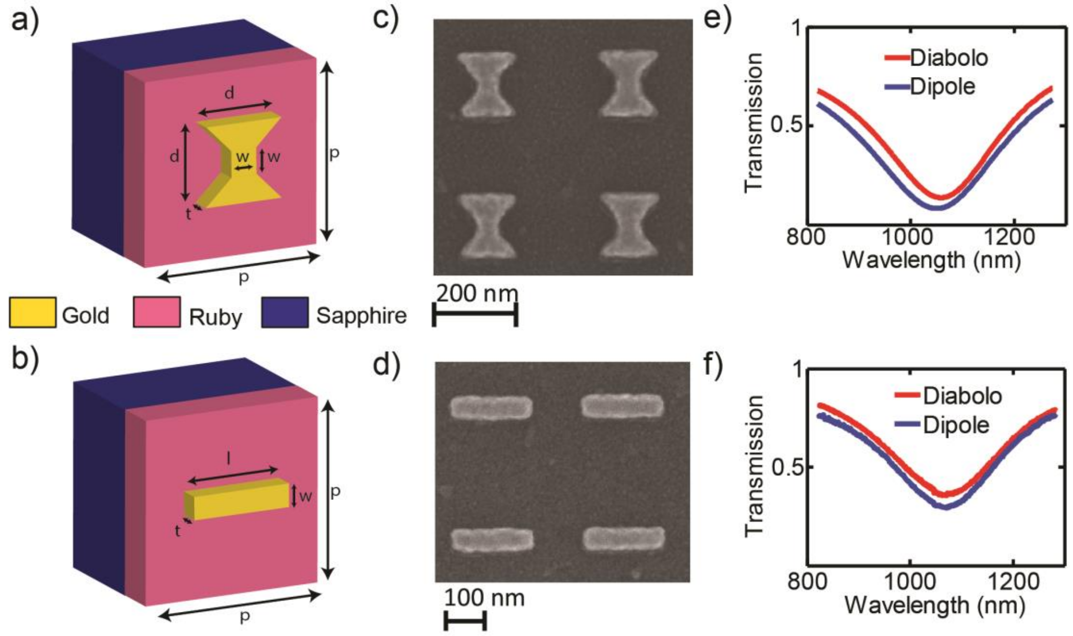

Figure 2.6. (a). Unit cell of diabolo antenna array with dimensions: p=340 nm, d=150, w=50 nm, t=50 nm. (b) SEM image of diabolo array. (c) Unit cell of dipole antenna array with dimension: l=215 nm. (d) SEM image of dipole array. (e) Simulated and (f) experimental transmission data. The dip in transmission corresponds to the resonant wavelength.

To experimentally validate the thermoplasmonic design rationale proposed in Section 2.2, here both dipole and diabolo antenna arrays with 250 x 250 unit cells, yielding patterned areas of 85 μm x 85 μm, were fabricated directly on the ruby temperature sensing layer using electron beam lithography (EBL), Cr/Au deposition, and ultrasonic lift-off. Fig. 2.6a,b shows the dimensions of each antenna array's unit cell. Fig. 2.6c,d shows scanning electron microscopy (SEM) images of the fabricated arrays and Fig. 2.5e,f shows the simulated and experimental transmission data, demonstrating good agreement with the spectral position of the resonant wavelength. The magnitude of the experimental transmission curves are slightly higher than the theory, likely due to inhomogeneities and surface roughness, effects that will serve to slightly lower heating compared to theory.

2.4 Thin Film Phosphor Lifetime Thermal Microscopy

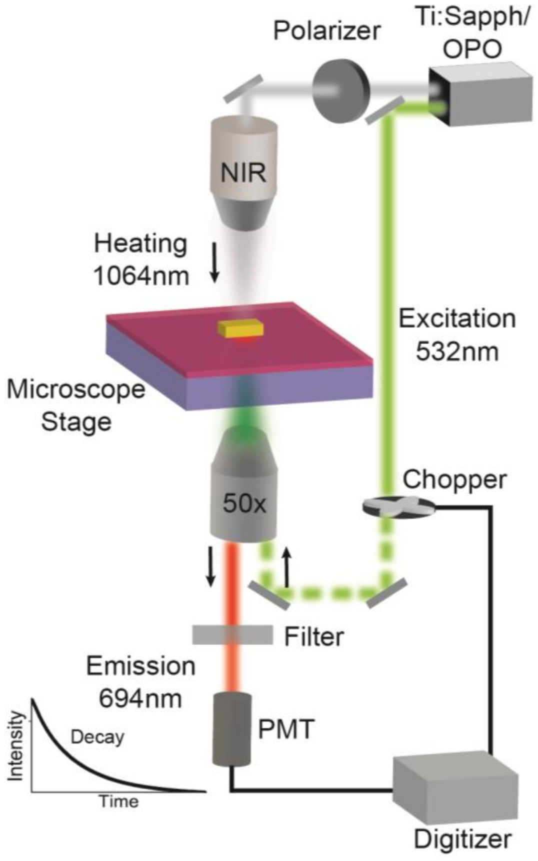

Figure 2.7. Thin-film thermographic phosphor thermal microscopy schematic.

In order to measure the local temperature of the plasmonic nanostructures, here a novel thermal microscopy based on thin-film TGP was developed. The resonant heating and thermal probing of the fabricated samples were performed with the thermal microscopy setup shown in Fig. 2.7. A Ti:Sapphire pumped optical parametric oscillator (OPO) was used to generate the infrared heating beam (1064nm) and the phosphor excitation beam (532 nm). Both beams were weakly focused through objectives and spatially overlapped on the sample to achieve uniform heating and phosphor excitation over the area of measurement. An optical chopper was used to modulate the excitation beam for measuring the lifetime of TGP emission.

The emission of the phosphor was collected from the bottom objective lens and directed through a 694 nm bandpass filter. Past the filter, the emission was routed to a fiber-coupled photomultiplier tube (PMT) to detect the phosphor decay time. A digitizer recorded and averaged 400 decay readings, each lasting for 50 ms, and the profile of the averaged decay reading was fit to a single exponential function to obtain the decay time[102]. It should be noted while 400 recordings per point are utilized in the present data to ensure an extremely low noise level for characterizing the technique, this amount of averaging is in general not needed.

Calibration of the ruby phosphor was necessary to match decay times with absolute local temperatures. To replicate the conditions of the actual measurement, the calibration was performed in the microscopy setup of Fig. 2.7. The sample was placed on an indium tin oxide (ITO) coated glass slide that acted as a transparent resistive heating element. A voltage applied to the ITO layer uniformly heated the sample and a thermocouple placed on top of the ruby layer measured the phosphor temperature. Metal objects near an emitter can drastically change the emitter's radiative and non-radiative decay rates and thus the decay time[116]–[118]. To take this effect into account, calibration measurements (Fig. 2.8a) were performed directly on the antenna array. Each decay measurement was taken at steady-state temperature, which was confirmed by taking several measurements until the decay time stabilized.

After calibrating the phosphor and allowing the sample to cool, the antenna arrays were optically heated and their temperatures were measured. For the measurements, the IR heating beam was polarized along the optical axis of the arrays and the power was set to vary from 14 mW to 125 mW. The beam was focused onto each array with a measured full-width-at-half-maximum (FWHM) of 19.5 μm resulting in 2583 antennas being heated in this region. After reaching steady-state conditions, decay times were recorded on each array and fit to the calibration curve. The resulting temperature rises under different heating beam power are displayed in Fig. 2.8b.The observed linear relationship results in temperature rises (ΔT) of 30.2°C and 23.7°C in the diabolo and dipole antenna arrays under a 125mW heating beam (0.4 mW/μm^2), respectively. This temperature rise come from the superposition of the heating contributions from each single antenna in the illuminated region. The results validate the proposed thermoplasmonic design rationale by demonstrating that the diabolo antenna, with its enhanced current density and magnetic field, generates more heat than the dipole antenna. To verify that the heating occurred through the resonant excitation of surface plasmons, the heating beam was rotated 90° to the off resonant polarization. As expected, the temperatures are only slightly increased due to non-resonant absorption in the metal nanostructures.

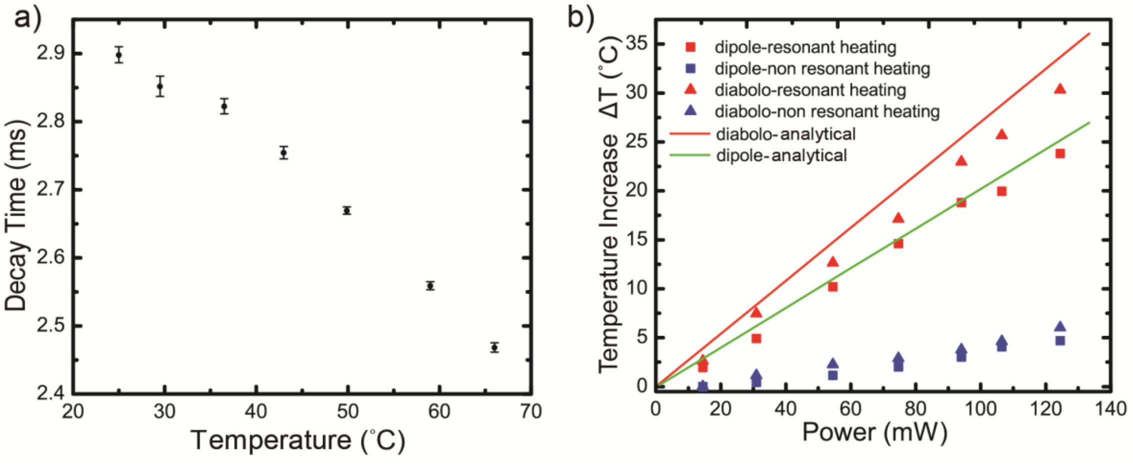

Figure 2.8. (a) Calibration curve of 100 nm ruby TGP. The error bars represent the 95% confidence interval of 10 measurements. (b) Temperature measurements of optically excited dipole (square) and diabolo (triangular) arrays versus heating beam power with non-resonant (blue) and resonant (red) polarizations. The results from the analytical model for the dipole (green line) and diabolo (red line) show good agreement with the experiment. ΔT is temperature rise over the ambient temperature.

To confirm the experimental measurements, the results were compared to an analytical, 3-D conduction model of the system. In the model, the ΔT of the arrays can be found from the equation, $q = Sk\Delta T$, where S is the conduction shape factor, k is the thermal conductivity of the substrate, and q is the heat generated by the array[119]. The model corresponds to a heated disk on a semi-infinite slab, a good approximation of the experimental conditions. For the case of a uniformly heated disk (which is the case for laser heating), $S = 3\pi^2 D/16$, where D is the heating beam diameter. Setting the conductivity of the substrate to the manufacturer specified value (25 W/mK) and using the antenna absorption loss calculated from finite difference time domain (FDTD) simulations, we obtain ΔT corresponding to the rise in the phosphor layer's average temperature over ambient. The results of the model (Fig. 2.8b) are in good agreement with the experimentally measured values, though the experimental antennae arrays exhibit a slightly lower temperature rise, as expected from the increased transmission through the arrays compared to theory.

2.5 Nanoparticle Superstructure with Plasmonic Lens

To take full advantage of the diabolo antenna's enhanced heat generation, it can be incorporated with a plasmonic lens to create a nanoantenna superstructure (Fig. 2.9a). The plasmonic lens of the superstructure allows for enhanced energy coupling to the diabolo antenna while retaining the antenna's nanoscale feature sizes and highly localized heating[93], [120]. To determine the temperature profile around the antenna, we modeled the distribution using the superposition of spherical Green's functions[121]. Because the thermal conductivity of the sapphire substrate is almost three orders of magnitude larger than air, the air/sapphire interface was assumed adiabatic and the temperature profile was mapped only in the sapphire. The heat generation input to the Green's function model was determined from FDTD simulations in which the absorption loss for the diabolo antenna as both a single structure and a superstructure were calculated. The input intensity in both simulations was 7.1 mW/μm^2.

The results of the FDTD simulations and thermal modeling show that the superstructure produces a temperature rise of 237° C while the single diabolo structure only produces a temperature rise of 45° C. This substantial difference in local temperatures is attributed to the increased energy coupling of the superstructure along with the scaling relationship in equation 2.1. The temperature maps (Fig. 2.9c,d) also show that the diabolo antenna in the superstructure still retains a highly localized thermal hotspot. It should be noted that the single antenna will yield a lower temperature increase than the antenna arrays for the same heating beam intensity. This is due to the fact that in the single antenna there is no superposition of the heating from neighboring antennas that are present in the array.

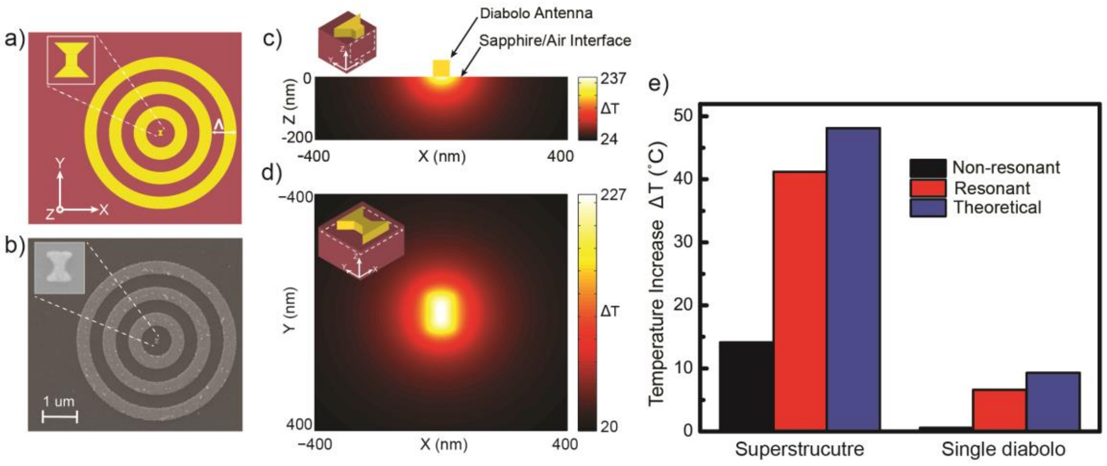

Figure 2.9. (a) Plasmonic superstructure made up of a diabolo antenna surrounded by 3 circular gratings: Λ=720 nm. Diabolo antenna dimensions are the same as Figure 2a. (b) SEM image of fabricated superstructure. (c) Temperature profile below the superstructure at the center of the neck region, taken in the X-Z plane. (d,c) Temperature profile of the superstructure 3 nm below the surface, taken in the X-Y plane. The white dotted lines in the inset indicate the planes in which the temperature profiles are plotted. (e) Experimental measured temperature rises of optically excited superstructure and single structure with non-resonant (black), resonant (red) polarizations at 110 mW and theoretical calculation (blue).

To experimentally validate the rationale of the proposed superstructure design, the superstructure and single diabolo antenna were fabricated on ruby sensing media (Fig. 2.9b) and the TGP thermal microscopy method was applied to measure the temperature of both structures. An IR heating beam with power of 110 mW was focused onto each structure with a measured FWHM of 4.44 μm resulting in a pump intensity of 7.1 mW/μm^2. The phosphor excitation beam was tightly focused onto the sample surface with a FWHM of 0.72 μm and spatially overlapped with both the structure and the heating beam. The resulting temperature rises of the superstructure (41.1°C) and single diabolo (6.6°C) are shown in Figure 2.9e.

In order to compare the theoretical and experimentally acquired antenna temperatures, the temperature profile acquired from the superposition model was averaged throughout the excited region of the TGP directly below antenna. The theoretical temperature increase of both structures shows good agreement with the experimental data, though as in the antenna arrays, the predicted temperature is slightly higher than the experimentally measured value likely due to surface roughness in the fabricated patterns. The superstructure shown here could be even further enhanced with the addition of more circular gratings to couple in more electromagnetic energy or the use of a lower thermal conductivity substrate to better insulate the bottom of the structure.

While here we have only measured single point or average array temperatures, the

TGP based thermal microscopy technique can readily be extended to 2D mapping of the temperature profiles with a resolution given by the diffraction limit of the phosphor excitation beam. In our current configuration, mapping speed is limited by the millisecond lifetime of ruby. However, the technique can readily be utilized using phosphors with nanosecond lifetimes in which case the mapping speed would be limited by the laser repetition rate. For example, with a pixel size of 0.4 μm^2, 25X decay averaging, and a 1 kHz laser, mapping of a 25µm x 25 µm area would take 40 s.

2.6 Conclusion

To summarize Chapter 2, we have developed a framework for both rational design of nanoscale heat sources as well as a technique for robust thermal microscopy. The scaling relationship in equation 2.1 provides a simple design criterion to realize both large heat source density and local temperature in thermoplasmonic structures where heat generation is dominated by Ohmic loss in the metal. The TGP thermal microscopy technique allows for probing large temperature ranges in a robust measurement scheme and could potentially see widespread adoption in micro/nanoscale science.

Chapter 3 Plasmon-induced Hot Electron Devices with Plasmonic Absorbers

3.1 Introduction

In Chapter 2, we have investigated photothermal heat generation in plasmonic nanostructures where the local heating comes from the decay of hot electrons. On the other hand, one can also use hot electrons for photoelectrical conversion by capturing the hot electron before it thermally decays. As discussed in Chapter 1, hot electron based photoelectrical conversion devices are typically formed by placing the metal surface of plasmonic structures in contact with a semiconductor[46], forming a Schottky barrier. Hot electrons generated from the non-radiative decay of SPs can transport to the metal/semiconductor interface before thermalization and be injected into the conduction band of the semiconductor, resulting in photocurrent. In this case, the device's bandwidth is limited by the Schottky barrier height, instead of the bandgap of the semiconductor. This allows one to harvest sub-bandgap photons compared with direct electron-hole pair excitation in the semiconductor, therefore can potentially provide extra photoelectrical energy conversion in photodetection, photovoltaics and photocatalysis. In particular for photodetection, this scheme allows one to do sub-bandgap photodetection, for instance photodetection in telecommunication band with silicon, at a potentially lower cost compared with existing Ge or InGaAs detectors.

Recently, hot electron detectors have been demonstrated using a variety of structures including nanorods[46], [122], nanowires[123], [124], metal gratings[48], [125], and waveguides[47], [126], [127]. However, the main drawback of previously demonstrated hot electron detectors is the low photoresponsivity, typically on the order of a few 10 to 100 μA/W[46], [123]. Recent studies[48], [125] have reported significant advances in detector efficiency by exciting propagating surface plasmon polariton (SPP) waves using metal gratings[48] or combining gratings with deep trench cavities[125]. For the latter case, the efficiency enhancement is largely due to high optical absorption and the use of thin metal layers, allowing the electrons to diffuse to the metal/semiconductor interface before thermalizing. However, due to the use of a grating, the optical absorption and photocurrent will be sensitive to the incident angle in these designs and the photodetection bandwidth is limited.

In this chapter, we will present an approach to greatly enhance photoresponsivity of hot electron detectors through the use of metamaterial perfect absorbers (MPAs). We propose a novel metamaterial perfect absorber design without the use of an optically thick ground plane. This allows us to integrate the MPA with dielectric of semiconductor layers that require high temperature processing or growth. The MPA architecture is integrated with n-type silicon (n-Si), to realize Schottky diode based hot-electron devices with high photoresponsivity in the near infrared region, well below the Si bandgap energy. We experimentally characterize numerous MPA based photodetectors with varying degrees of polarization sensitivity and response bandwidth. By taking advantage of the strong optical absorption in MPAs, combined with ultra-thin metal layers, we demonstrate photoresponsivities that are among the highest reported while also preserving an omnidirectional, polarization insensitive and broadband response. Specifically, we demonstrate a detector with an absorption FWHM up to 800 nm and a photoresponsivities larger than 1.8mA/W from 1200nm to 1500nm. This design is also scalable to arbitrary wavelengths within the solar spectrum and could potentially open a pathway for enhancing the efficiency of hot electron based photovoltaic, sensing, and photocatalysis systems.

3.2 Metamaterial Perfect Absorber Photodetector

To begin, we first examine a polarization sensitive MPA photodetector composed of 1D metal stripes, a schematic of which is illustrated in Fig. 3.1a. The MPA is composed of a pre-patterned n-type Si substrate, forming Si stripes, with a 1nm titanium adhesion layer and a 15nm gold film deposited on the surface. The metal film is naturally separated into upper and lower plasmonic stripe antennae. When the MPA is illuminated with TM-polarized light (E-field perpendicular to the stripe direction), localized surface plasmon resonances (LSPRs) are excited on the upper antennae (Fig. 3.1b). A Fabry-Perot resonance is also present in the cavity formed from the upper and lower stripe antennae. By carefully designing the antenna length *L*, cavity height *H*, and periodicity *P*, the antenna and cavity resonances can be overlapped, leading to near unity absorption as shown in Fig. 3.1c calculated from full-wave electromagnetic simulation.

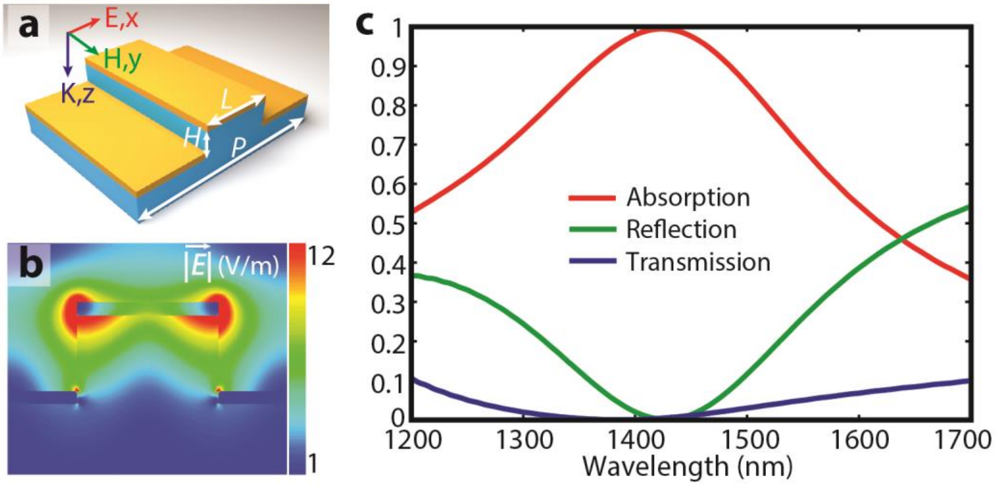

Figure 3.1. (a). Schematic of the MPA unit cell with upper and lower resonators (gold) integrated with a semiconductor (blue). (b) Simulated electric field distribution in the MPA under illumination with TM-polarized light. (c) Simulated optical reflection,

transmission and absorption for an MPA with L=160nm, P=320nm, H=120nm metallized with a 1nm thick Ti adhesion and 15nm thick Au layer.

Furthermore, the thickness of the plasmonic antenna is only 15nm, less than the hot electron diffusion length[128], ensuring that the hot electrons have a high probability of diffusing to the metal-semiconductor interface. It should be pointed out that, in contrast with most of the previously demonstrated MPA structures[129]–[131], all the metal constituents in our proposed MPA design are ultrathin and an optically thick metallic ground plane is not required here. This ensures all of the optical absorption and hot electron generation occur in the thin plasmonic antenna layers. This architecture also eliminates the need to grow a high quality semiconductor on top of a metal film, which would be challenging due to the high process temperatures required.

To experimentally characterize the photodetector, fabrication began by first defining the stripe patterns on a double side polished n-type Si wafer using poly(methyl methacrylate) (PMMA) and electron beam lithography. The MPA detectors were patterned with an overall size of 85um x 85um. The PMMA was used as a mask for patterning the underlying n-type Si using reactive-ion etching (RIE). After the RIE process, the sample was immersed in a 10:1 buffered oxide etchant (BOE) for 1 minute to completely remove the native oxide. The sample was then immediately transferred into the evaporation chamber followed by deposition of 1nm Ti and 15nm Au layers. Three devices D1, D2 and D3 were fabricated (Fig. 3.2a, b) with dimensions of L = 160nm, 170nm, 170nm and P = 320nm, 320nm, 340nm, respectively. The etching depth H for the three devices were all 120nm, which was measured using AFM.

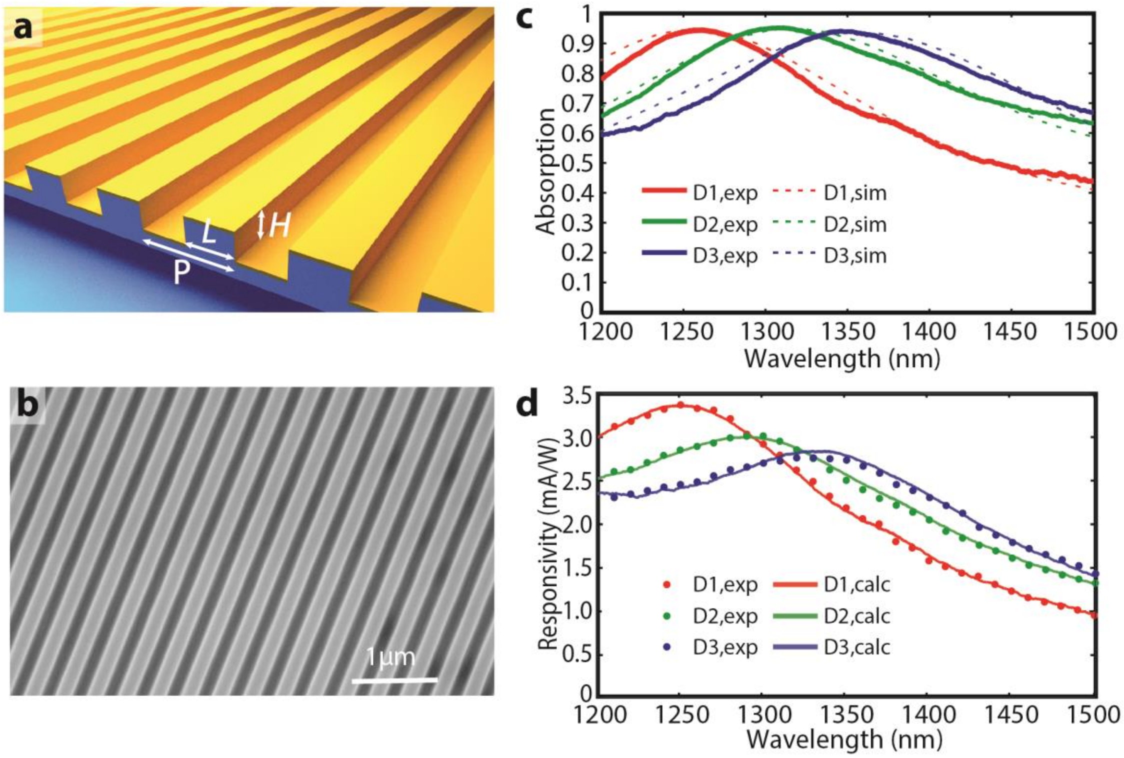

Figure 3.2. (a). Schematic of the fabricated 1D MPA detector including a thin metal coating on the sidewall. Dimensions of the MPA detectors D1, D2 and D3 are L = 160nm, 170nm, 170nm and P = 320nm, 320nm, 340nm, respectively. The etching depth, H, for the three devices was 120nm. (b) SEM image of a fabricated device. (c) Experimentally measured (solid lines) and simulated (dashed lines) absorption spectra of D1, D2 and D3 (red, green, and blue solid lines, respectively) (d) Experimentally measured (circles) and calculated (lines) photoresponsivity spectra of D1, D2 and D3 (red, green and blue, respectively).

3.3 Optical and Electrical Characterization

The optical absorption spectrum of the device was performed by measuring the reflection R and transmission T in an infrared microscope coupled to a grating spectrometer. The reflection spectra were normalized to a silver mirror and the transmission spectra were normalized to transmission through air and absorption was calculated as $A = 1 - T - R$. The optical absorption of these devices is shown in Fig. 3.2c. The devices show broadband optical absorption in the near IR region with a maximum value of 95% and a FWHM of 400nm. Furthermore, it is evident that the absorption and photoresponsivity spectrum can be readily varied by tuning the dimensions of the structure.

It should be noted that, although in the proposed structure the upper and lower metal constituents are electrically isolated, in the fabricated structure there is a thin coating of metal on the sidewall of the Si ridge due to the slight sidewall angle. As a result, the absorption peak positions of the fabricated structure are slightly blue shifted from the proposed structure without sidewall. However, good agreements were still observed between the simulated absorption spectrum with sidewall coating and the measured absorption spectrum (Fig. 3.2c). The connection between the upper and lower antennae also ensures both of the metal layers are included in the electrical circuit and can contribute to the total photocurrent.

To characterize the hot-electron transfer efficiency of the devices, the sample was wire bonded to a chip carrier and the photocurrent measurements were performed on the MPA detectors across a wavelength range of 1200nm to 1500nm (Fig. 3.2d). These MPA detectors show a broad photoresponsivity spectrum with a peak value of 3.37mA/W, 3.05mA/W and 2.75mA/W for devices D1, D2 and D3 without external bias, respectively. Furthermore, the current varies linearly with the incident power, indicating that non-linear processes are not playing a role in the response. These photoresponsivities are several orders of magnitude larger than previously demonstrated LSPR-based nanoantenna photodetectors[46] and over four times larger than the SPP-based metal grating photodetectors[48]. The photoresponsivities of the MPA detectors are comparable with the recently reported deep trench cavity structure[125] at short wavelengths. However, the MPA detectors show a broadband response with much larger photoresponsivities at longer wavelengths.

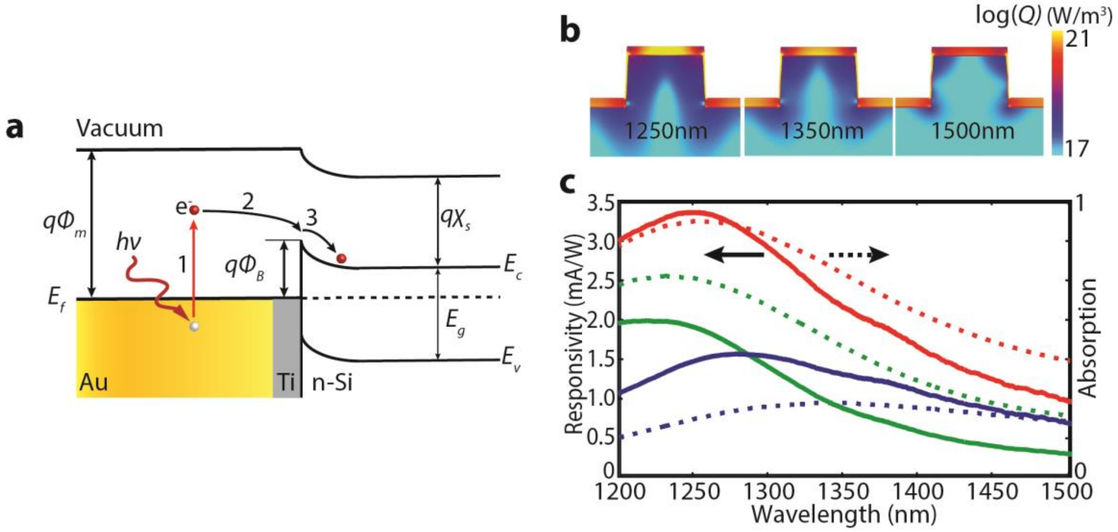

Figure 3.3. (a). Schematic of the hot electron transfer process over the Schottky barrier formed by the metal-semiconductor interface. Steps 1 to 3 correspond to hot electron generation, diffusion to the Schottky interface, and transmission to the conduction band of semiconductor. (b) FDTD simulation of absorbed power density in a 1D MPA device at 1250nm, 1350nm and 1500nm (plotted on a logarithmic scale for better visualization). (c) Calculated photoresponsivity (solid lines) and absorption (dash lines) in a MPA device. The total (red), upper resonator (green) and lower resonator (blue) contributions are plotted separately.

The photoresponsivity of the MPA detectors can be understood by considering the hot electron transfer process over the Schottky barrier which is dictated by a three-step model[58], [59] as shown in Fig. 3.3a: (1) Plasmons non-radiatively decay into hot electrons (optical absorption), (2) hot electrons transport to the metal/semiconductor interface before they thermalize, and (3) hot electrons inject into the conduction band of the semiconductor through internal photoemission. Here, we analyze the two different components in the MPA detectors separately, the upper antenna and the lower antenna, which yield different hot electron generation and quantum transmission probabilities. As a result, the photoresponsivity spectrum of MPA detectors can be calculated as:

$$R(v) = \sum_{i=u,l} A_1^i(v)\, \eta_2(v) \eta_3^i(v) \tag{3.1}$$

where u and l represent the upper and lower antenna, respectively, and v is frequency. $A_1^i(v)$ is the optical absorptivity of each component, which can be determined by the measured total absorption spectrum of the MPA detectors along with the absorption distribution in each antenna layer. The absorption distribution in the MPA devices (Fig 3.4b) were calculated numerically using the local ohmic loss, given by,

$$Q(r,\omega) = \frac{1}{2}\omega \mathrm{Im}(\varepsilon_m)\left|\vec{E}(r,\omega)\right|^2 \tag{3.2}$$

where $\left|\vec{E}(r,\omega)\right|$ is the local electric field and $\mathrm{Im}(\varepsilon_m)$ is the imaginary part of the metal permittivity. This allows us to determine the wavelength dependent absorptivity of the upper, A_1^u, and lower, A_1^l, antenna (dash lines in Fig. 3.3c). $\eta_2(v)$ is the probability that the hot electron will transport to the Schottky interface and is dependent on the spatial distribution and mean free path of the hot electrons[128]. $\eta_3^i(v)$ is the internal photoemission of hot electrons across the Schottky interface for the upper and lower antenna and is calculated using the modified Fowler equation[57], [60],

$$\eta_3^i(v) = C_F^i \frac{(hv - q\phi_B)^2}{hv} \tag{3.3}$$

where C_F^i is the device-specific Fowler emission coefficient, hv is the photon energy, and $q\phi_B = 0.54eV$ is the Schottky barrier height for the MPA devices which is extracted from the current-voltage characteristics of the device[60]. Fitting the experimentally measured photoresponsivity spectrum with equation (3.1), where $\eta_2(v)$ and C_F^i are treated as fitting parameters, results in good agreement with the experimental data as shown in Fig. 3.2d. The extracted ratio of C_F^l/C_F^u is around 3 for all three devices, indicating that hot electrons generated in the lower antenna have a higher quantum transmission probability compared with the upper antenna. This effect is mainly due to the formation of a 3D Schottky interface between the semiconductor and the embedded bottom antenna, allowing the hot electrons to cross the interface over a larger emission cone[123]. While total absorption drops at longer wavelengths, the bottom antenna layer's contribution remains relatively constant, resulting in photocurrent being dominated by the bottom layer at long wavelengths (Fig. 3.3c). Strong broadband absorption $A_1(v)$ and high transport efficiency $\eta_2(v)$ in the ultrathin metal film ultimately ensure high photoresponsivity over a large bandwidth.

3.4 Polarization-independent and Broadband Perfect Absorber Photodetector

In order to achieve a polarization-independent photoresponse, the 1D stripe antennae can be replaced by square antennae, forming a 2D MPA structure as shown in Fig. 3.4a and Fig. 3.4b. In this case, the upper antenna layer can still contribute to the photocurrent due to the thin metal sidewall coating. Experimental validation of this concept was accomplished using three devices D4, D5 and D6 with dimensions of L = 185nm, 195nm, 195nm and P = 340nm, 340nm, 360nm, respectively. The etching depth H for three devices are all 135nm, confirmed by AFM. These polarization-independent MPA structures still maintain near-unity absorption (Fig. 3.4c) over a large bandwidth. Furthermore, the LSPR based MPA maintains a peak absorptivity above 90% for incident angles of up to 75° and 60° under p- and s-polarized light, respectively (Fig.3.5d). This is in contrast to previously demonstrated metal grating[48] and the deep trench cavity[125] hot electron photodetectors which rely on the excitation of propagating SPP waves through grating coupling, resulting in an angularly sensitive response. As a result, these 2D MPA detectors show high photoresponsivities (Fig. 3.4e) while also preserving a broadband, omnidirectional, and polarization-independent response.

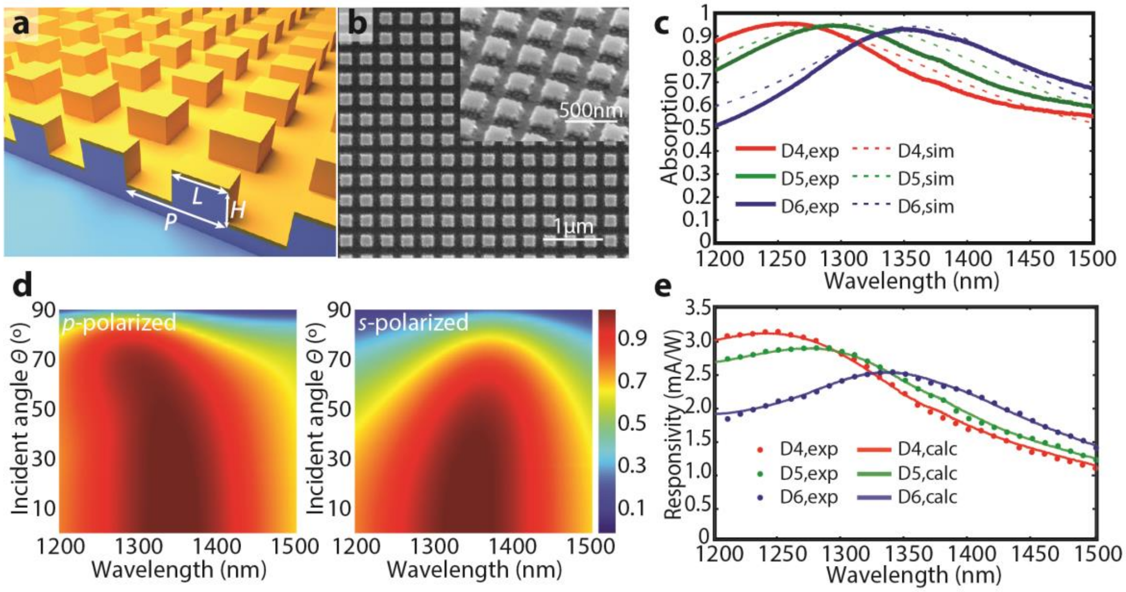

Figure 3.4. (a). Schematic of the polarization-independent MPA detectors. Dimensions of MPA detectors D4, D5 and D6 are L = 185nm, 195nm, 195nm and P = 340nm, 340nm, 360nm, respectively. The etching depth, H, for the three devices was 135nm. (b) SEM image of a fabricated device. (c) Experimentally measured (solid lines) and simulated (dashed lines) absorption spectra of D4, D5 and D6 (red, green and blue lines, respectively) (d) FDTD simulation of the angularly dependent optical absorption for p (left) and s-polarized light (right). (e) Experimentally measured (circles) and calculated (lines) photoresponsivity spectra of D4, D5 and D6 (red, green and blue, respectively).

Taking advantage of the high photoresponsivity and tunability of the 2D MPA structures, we can further enhance the absorption bandwidth by implementing MPAs with multiple resonator sizes. To demonstrate this, we combine two different 2D MPA unit cells, forming a bipartite checkerboard supercell, shown in Fig. 3.5a,b. In this case, the separate resonances of the two MPA unit cells result in bandwidth enhancement, though there is a slight decrease in peak absorption. However, the broadband MPA detector with dimensions L_1 = 185nm, L_2 = 225nm, P = 680nm, H = 160nm still maintains absorption over 80% from 1250nm to 1500nm (Fig. 3.5c). Although the FWHM of the absorption was not measurable due to our spectrometer's detection range, data from simulation shows a FWHM of over 800nm. The photoresponsivity of this broadband MPA detector is larger than 1.8mA/W from 1200nm to 1500nm (Fig. 3.5d), making it a candidate for broadband, polarization-independent and omnidirectional silicon based near-IR photodetectors.

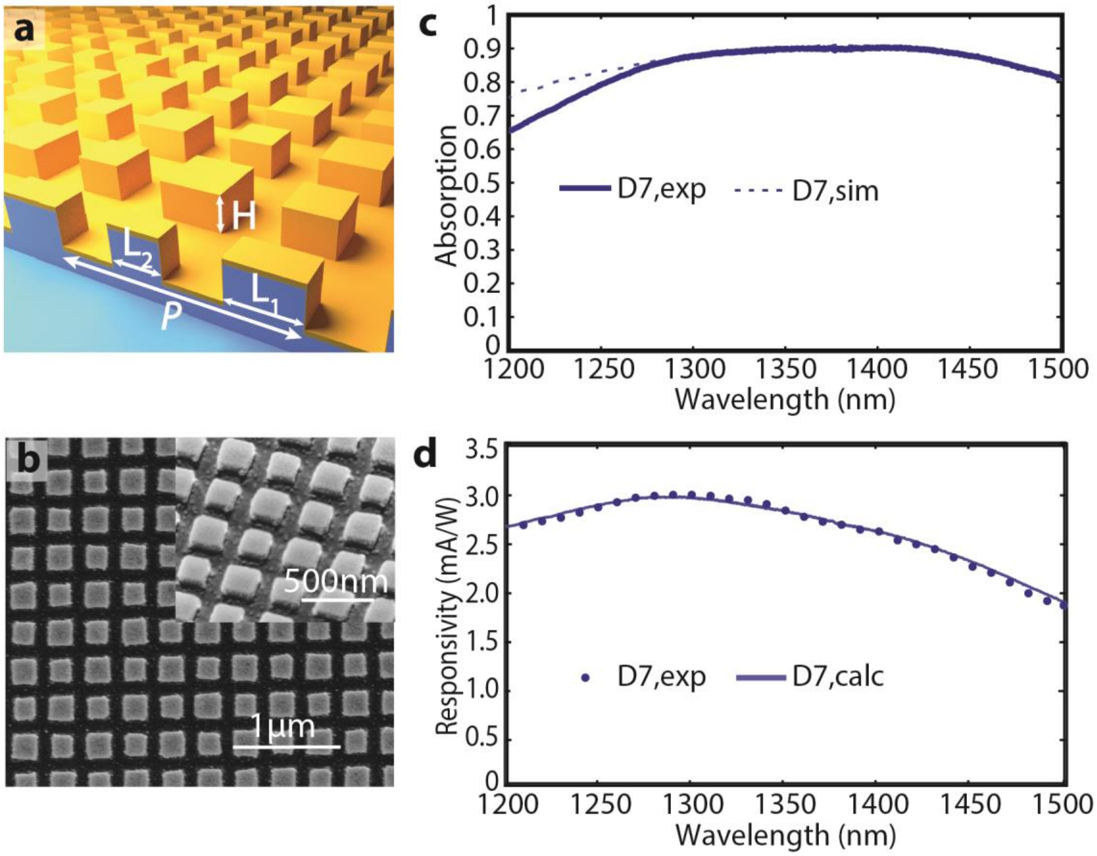

Figure 3.5. (a). Schematic of the broadband MPA photodetector. Dimensions of the MPA detector are L_1 = 185nm, L_2 = 225nm, P = 680nm, H = 160nm. (b) SEM image of the fabricated device. (c) Experimentally measured (solid) and simulated (dashed) absorption spectra of the broadband MPA detector. (d) Experimentally measured (circles) and calculated (line) photoresponsivity spectra of the broadband MPA detector.

The performance of the MPA detector could be further improved by engineering the Schottky barrier height, roughing the metal semiconductor interface[126], or embedding the top antenna layer within the semiconductor[123]. Also, while we have focused on maximizing the bandwidth of the photoresponse, the tunability of the MPA architecture also offers a possibility to achieve a narrowband photoresponse. For instance, a narrow Fano resonance can be realized in these structures by coupling a grating mode with the LSPR resonance, leading to an extremely narrowband absorption[132] which could potentially lead to a plasmonic spectrometer with direct electrical readout[48]. Furthermore, although the demonstrated MPA detectors work in the near IR region, they can be scaled to the visible regime by replacing Si with a higher bandgap semiconductor such as TiO_2. In the visible regime, the use of ultrathin metal layers in this type of MPA design could be particularly beneficial due to the drastically reduced hot electron diffusion length[128].

3.5 Plasmonic absorber design for hot-electron catalysis

In the previous sections, we have focused on how the plasmonic nanostructures were engineered to enhance the efficiency of hot electron based photodetection systems. It should be noted that similar design principles could be directly applied to hot electron catalysis systems[41], [42], [133], which can potentially provide better stability and a broader working wavelength compared to semiconductor-based water splitting systems[134]. However, the overall quantum efficiency of hot-electron catalysis systems has remained low due to the low hot electron transfer efficiency and low optical absorption. To overcome these challenges the MPA design can be readily modified for hot electron-based catalysis. In the proposed device, a commonly used photocatalysis material, TiO_2, is employed as the semiconductor and the plasmonic structures have been designed as circular disk resonators with a hexagonal lattice arrangement. This design

(Fig. 3.6a) offers the potential to realize large area devices with lost cost and high throughput techniques such as nanosphere lithography[135]–[139]. By correctly engineering the structure's dimensions, one can achieve strong resonant optical absorption (Fig. 3.6b) in the plasmonic structures. In this case, the hot electrons need to diffuse to the Schottky interface whereas the holes need to diffuse to the metal surface for the oxidation reaction. Key to the design is ultrathin plasmonic nanostructure with a thickness of 15nm. The thin metallic layer is extremely important because it provides efficient carrier transport for both electrons and holes. Therefore it can boost the overall system efficiency.

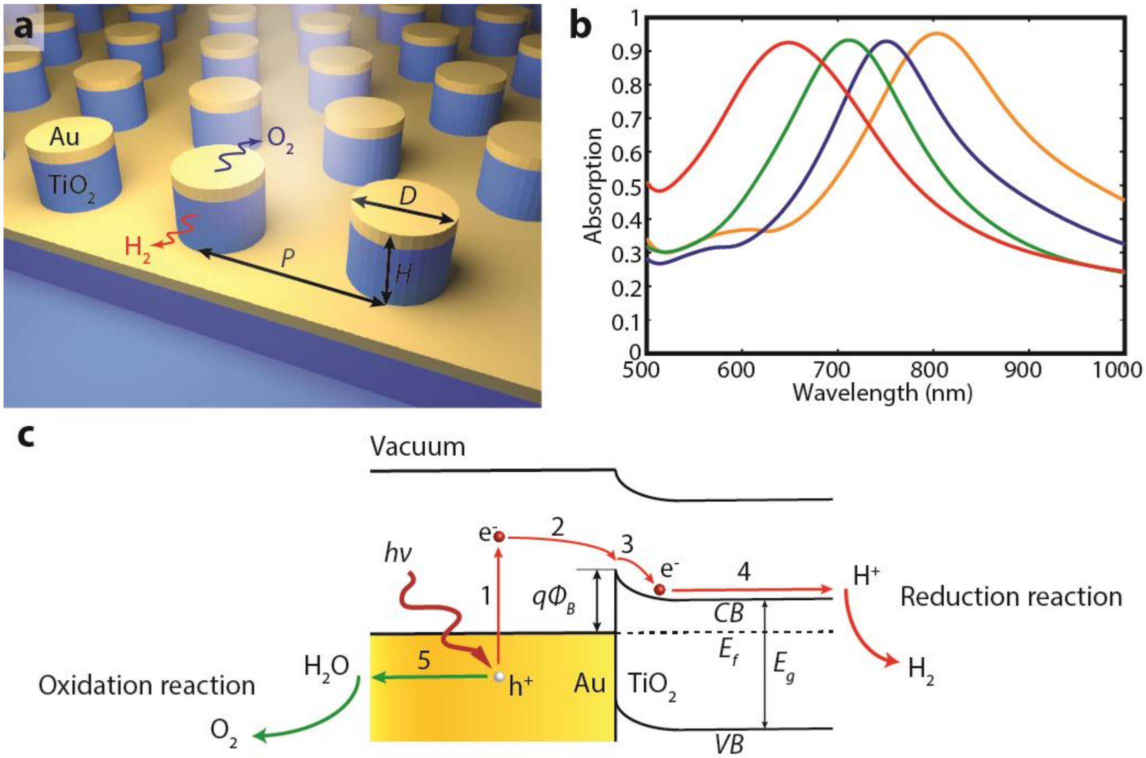

Figure 3.6. (a) Schematic of the proposed large-scale metamaterial perfect absorber. (b) Optical absorption spectra of the structure from FDTD simulation. The dimensions of the four simulated structures (red, green, blue, orange curves) are D=80nm, 80nm, 100nm, 120nm, P=165nm, 155nm, 200nm, 250nm, and H=100nm, 85nm, 80nm, 100nm respectively. The thickness of the gold layer is 15nm. (c). Band diagram schematic of a plasmonic solar water splitter, illustrating the process of hot-electron based water

splitting system. 1. Plasmon decay into electron-hole pair. 2. Hot electron diffuse into the metal-semiconductor interface. 3. Hot electron inject into the conduction band of TiO_2. 4. Hot electron transport to the semiconductor-water interface and lead to hydrogen reduction reaction. 5. Hot holes in gold can transport into the interface and lead to oxidation reaction.

3.6 Conclusions

To summarize chapter 3, we have demonstrated how hot electron photoelectrical energy conversion efficiency can be significantly enhanced by correctly engineering the plasmonic nanostructures. Realizing near unity absorption within ultrathin plasmonic nanostructures allows the efficiency of the hot electron transfer process to be significantly enhanced, resulting in hot electron photodetectors with photoresponsivities that are among the highest reported. Furthermore, the MPA architecture allows us to preserve a broadband, omnidirectional, and polarization invariant response. This ultra-compact, CMOS-compatible Si-based MPA detector can also be readily integrated into on-chip optoelectronics and can be scaled to the solar spectrum, potentially leading to enhanced efficiencies in hot-electron based photodetection, photovoltaic, and photocatalysis systems.

Chapter 4 Circularly Polarized Light Detection with Chiral Metamaterials

4.1 Introduction

In Chapter 3, we investigated photoelectrical conversion based on hot carrier generation and injection and demonstrated how plasmonic nanostructures can be engineered to enhance the efficiency of photodetection system. One of the unique benefits of hot electron-based detection is that the plasmonic geometry can be engineered to display a wide range of optical properties including polarization, wavelength, and angle of incidence selectivity. This opens up opportunities to tailor the response of a photodetector to realize unprecedented functionalities, such as the detection of circularly polarized light (CPL).

Circularly polarized light (CPL) is utilized in various optical techniques and devices, ranging from quantum computation[140]–[142] and spin optical communication[143] to circular dichroism (CD) spectroscopy[144] and magnetic recording[145]. In circularly polarized light the electric field vector travels along a helical trajectory, either clockwise or counterclockwise[146], and it can be generated from two linearly polarized light (LPL) waves with perpendicular electric field vectors that are oscillating with a 90° phase shift. Distinguishing between the two polarizations of CPL is inherently difficult with conventional photodetectors due to the fact that conventional semiconductors lack intrinsic chirality. Interestingly, in Nature some species of mantis shrimp can detect CPL and use it as a private channel of communication that is unavailable to both predators and potential competitors[147]. The origin of this ability comes from specialized cells in the retina that serve as quarter-wave plates that sit atop

LPL sensitive photoreceptors and convert CPL into LPL[147]. This is done in the same manner as CPL is detected using conventional optics, namely through the combination of a non-chiral photodetector with a quarter waveplate and a linear polarizer. While ultracompact optical elements and devices including CPL sources[148], [149], quarter waveplates[150], polarizers[151], and beam splitters[152], [153] have been successfully demonstrated, the use of multiple optical elements to distinguish CPL makes it challenging to realize miniature and integrated CPL detectors.

One alternative technique is the use of chiral media as the active material in a photodetector. A chiral medium, one in which the unit cell cannot be superimposed upon its mirror image, responds differently for left-handed circularly polarized (LCP) light and right-handed circularly polarized (RCP) light. Chiral media exists in nature, for example the iridescent metallic green beetle, *Chrysina gloriosa*, selectively reflects LCP light but absorbs RCP due to structural chirality[154] while sugar molecules, acids, and proteins exhibit intrinsic chirality. Recently, a chiral organic semiconductor transistor has been demonstrated for direct detection of circularly polarized light using the intrinsic chiral response of helicene at a wavelength of 365nm[155]. Though this technique shows promise, the organic semiconductor is unstable in ambient conditions. It also has a limited response time and the operational wavelength is limited to the ultraviolet regime.

Over the past decade, advances in plasmonics have provided a mechanism for strong light-matter interaction leading to strong field enhancement and resonant scattering and absorption. Furthermore, surface plasmon resonances offer new insights into creating artificial media, or metamaterials, with interesting optical properties such as strong chirality[156], [157] that is several orders of magnitude larger than that of chiral molecules. A number of chiral metamaterials based on plasmonic building blocks including spiral[158],[159], fish-scale metamaterials[160], helix[151], [161], [162], oligomers[163] and twisted metamaterials[164], [165] have been demonstrated to date using both bottom-up[161], [166] and top-down approaches[151], [163]–[165]. In addition, Archimedes spiral designs have been utilized to enable chiral-selective field enhancements in semiconductors, leading to selective photocurrent for LCP and RCP light, with an experimentally measured ratio of 1.13[158]. The use of plasmonic elements also opens the door to photon energy harvesting through hot carrier generation and injection[37], [38], leading to a new scheme for photodetection[3], [46], [48], [49], [126], [123], [124] and photocatalysis[40], [42]. Hot carriers generated from the non-radiative decay of surface plasmons can be captured with electron acceptors such as metal-semiconductor Schottky interfaces[3], [46], [48], [167], [126], [123] or metal-insulator-metal junctions[49], [124], resulting in photocurrent. This scheme enables direct conversion of light into an electrical signal based solely on the photo-excited carriers generated from the absorption in plasmonic nanostructures. The tunability of the plasmonic structures enables a straightforward tailoring of the response of a photodetector including the working wavelength, bandwidth, and polarization dependence[3], [46], [48], [124].

In this chapter, we propose and experimentally demonstrate an ultracompact circularly polarized light detector in which the ability to distinguish LCP and RCP comes from the engineered chirality in plasmonic nanostructures. Photodetection is based on hot electron injection into silicon with operation in the telecommunications band. Implementation of this CPL photodetector could lead to enhanced security in fiber and free-space communication as well as emission, imaging, and sensing applications for circularly polarized light.

4.2 Chiral metamaterial and device design

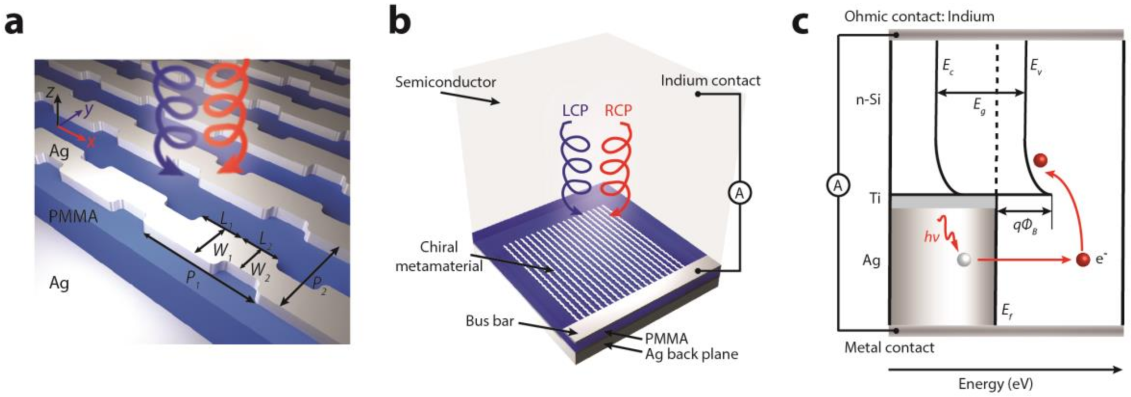

Figure 4.1. (a). Schematic of the chiral metamaterial and the CPL detector. a, Schematic of the chiral metamaterial consisting of the chiral plasmonic meta-molecules array, dielectric spacer, and metal back plane. The dimensions of the meta-molecules are L_1 = 125 nm, L_2 = 105 nm, W_1 = 115 nm, W_2 = 85 nm, P_1 = 335 nm, P_2 = 235 nm. The thickness of the antenna, dielectric spacer and the metal back plane are 40 nm, 160 nm, and 100 nm respectively. b, Schematic of the CPL detector consisting of a chiral metamaterial integrated with a semiconductor that serves as a hot electron acceptor. The Ohmic contact on Si is formed by soldering indium. The circuit is formed by wire bonding to the silver bus bar and indium. c, Energy band diagram of the CPL detector. A Schottky barrier is formed between Si and the Ti interfacial layer. Hot electrons photogenerated in the Ag metamaterial are then injected over this barrier into the Si.

Our proposed chiral metamaterial (Fig. 4.1a) is a periodic array of chiral meta-molecules, with a unit cell consisting of a ‘Z’ shaped silver (Ag) antenna on top of a PMMA spacer and an optically thick Ag backplane. The unit cell shape of this chiral metamaterial allows for an inherent electrical connection among all the elements, forming nanowires, while a silver bus bar is used to electrically connect the nanowires (Fig. 4.1b). The whole device is realized by placing an n-type silicon wafer in contact with the antenna layer, forming a Schottky barrier (Fig. 4.1c). Light is incident on the front side of the Si wafer, transmitting to the back side where the chiral metamaterial absorbs photons of a particular handedness, generating electrons within the metal at higher energy states. The energetic electrons (or hot electrons) with energy higher than the Schottky barrier can emit over the Schottky interface, leading to a detectable current (Fig. 4.1c).

To investigate the optical response of the device upon CPL illumination, full-wave electromagnetic simulations were performed using commercially available software (CST Microwave Studio 2013 and Lumerical). In all simulations, periodic boundary conditions were used along the x- and y-axis and perfectly matched layers were used along the propagation directions. LCP and RCP light are incident onto the front side of the silicon wafer, transmitting to the back side where the chiral metamaterial selectively absorbs light with a particular handedness while reflecting the other. For example, a left-handed (LH) chiral metamaterial acts as a perfect LCP light absorber at the resonant wavelength while reflecting nearly 90% of the RCP light (Fig. 4.2a) and vice versa for the right-handed (RH) chiral metamaterial (Fig. 4.2b), leading to a circular dichroism ($CD = A_{LCP} - A_{RCP}$) of almost 0.9 (Fig. 4.2c). Replacing the antenna layer with an unstructured Ag film results in 95% reflection, indicating we are nearly at the Drude damping limit. The chiral response can also be tuned across the entire telecommunication regime as shown in Fig. 4.2d. The minimum and maximum working wavelength are only limited by the semiconductor band gap energy and the Schottky barrier height, respectively. The limit imposed by silicon's bandgap is due to the fact that we are illuminating the device through the silicon wafer and must avoid direct absorption by the semiconductor.

To understand the origin of the strong circular dichroism, the CPL electric field vector can be decomposed as two orthogonal LPL electric field vectors, $\boldsymbol{E}_x$ and $\boldsymbol{E}_y$, that are oscillating with a 90° phase shift:

$$\mathbf{E}_{LCP} = \left(E_x, E_y\right)^T = \left(\frac{1}{\sqrt{2}}, \frac{1}{\sqrt{2}} exp\left(-\frac{\pi}{2}\mathbf{i}\right)\right)^T \tag{4.1}$$

$$\mathbf{E}_{RCP} = \left(E_x, E_y\right)^T = \left(\frac{1}{\sqrt{2}}, \frac{1}{\sqrt{2}} exp\left(\frac{\pi}{2}\mathbf{i}\right)\right)^T \tag{4.2}$$

These fields are input into a multiple reflection model in which we track the reflected electric field evolution as a function of the number of reflections (Fig. 4.2e,f) between the LH chiral metamaterial and the metal backplane. As seen in Fig. 2e and f, upon multiple reflections, both the reflected E_x and E_y fields for LCP are diminished (Fig. 4.2e), while the RCP fields grow (Fig. 4.2f). This highly asymmetric effect (Fig. 4.2g,h) comes from the destructive (LCP) and constructive (RCP) interference of the illumination beams and relies on the fact that the planar metamaterial is lossy, anisotropic, and results in linear polarization conversion. More details regarding these requirements, the response of this specific metamaterial, and general design guidelines for planar chiral metamaterials can be found in Section 4.3. It is also important to note that while the handedness of CPL is reversed at the metal backplane the reflected light will see the handedness of the planar chiral metamaterial reversed as well.

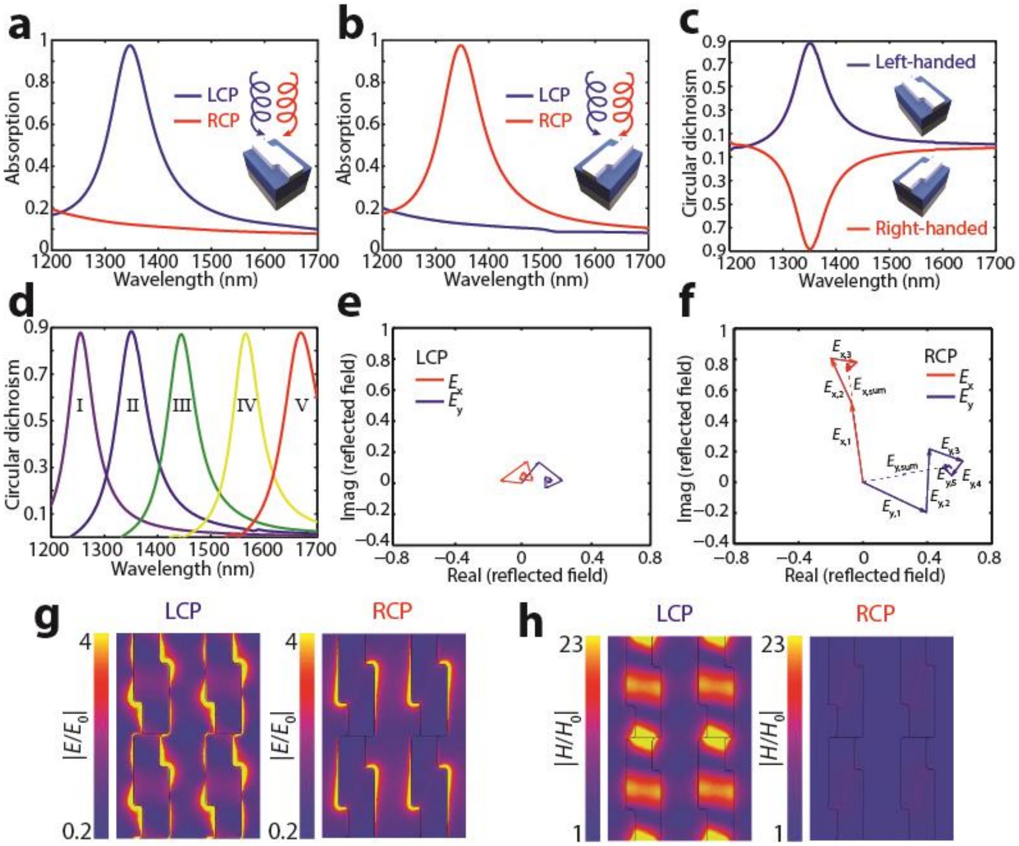

Figure 4.2. Simulated optical response of chiral metamaterial. a,b, Simulated optical absorption spectra under LCP (blue) and RCP (red) illumination for LH (a) and RH (b) metamaterials. c, Circular dichroism spectra for both the LH (blue) and RH (red) metamaterial. d, CD as a function of resonator size. Dimensions of the structures (I to V) are L_1 = 115, 125, 130, 150, 160 nm, L_2 = 95, 105, 120, 130, 140 nm, W_1 = 110, 115, 120, 120, 140 nm, W_2 = 85, 85, 90, 90, 100 nm, P_1 = 305, 335, 370, 410, 440 nm, P_2 = 230, 235, 240, 240, 260 nm, respectively. The other dimensions are the same as Fig.1a. e,f, For the LH metamaterial, the reflected LPL components, E_x (red) and E_y (blue), upon multiple reflections for LCP (e) and RCP (f) light at wavelength of 1350 nm. g,h, Simulated electric (g) and magnetic (h) fields for LCP and RCP illumination at wavelength of 1350 nm.

4.3 Circular dichroism design rationale

In Section 4.2, we have proposed a chiral metamaterial design with near perfect circular dichroism response. In this section, we aim to understand the chiral optical response from chiral metamaterial and provide a general design rationale for designing chiral metamaterial with strong circular dichroism. Due to the rotation of the electric field vector in circularly polarized light, directly relating the spectral position and magnitude of circular dichroism with the structure's geometry is usually challenging. Therefore, we will first investigate the system's optical response under linearly polarized light and then relate it to circularly polarized light, simply due to the fact that the CPL electric field vector can be decomposed into two perpendicular LPL electric field vectors, $\boldsymbol{E}_x$ and $\boldsymbol{E}_y$, that are oscillating with a 90° phase shift, as shown in equation 4.1 and 4.2.

First, we choose a system with an array of silver stripes, without a metal backplane, aligned in the *x* direction with a unit cell shown in Fig. 4.3a. To represent a more general situation, we choose the background material to be PMMA (n = 1.47) to avoid the substrate induced reflection and symmetry breaking. We examined the reflection coefficients of this system under two orthogonal linearly polarized light fields with electric field vectors of $\boldsymbol{E}_x$ and $\boldsymbol{E}_y$. Both the amplitude and the phase of the reflected light from this system are shown in Fig. 4.3c,d.

As can be seen in Fig. 4.3c,d, since this system is anisotropic in the *xy* plane, both the amplitude and the phase of the two reflection coefficients $\boldsymbol{r}_{xx}$ and $\boldsymbol{r}_{yy}$ are different. Under CPL illumination (Fig. 4.3e,f), the reflected field in the *x* direction, $\boldsymbol{r}_{xx}\boldsymbol{E}_x$, for LCP and RCP are exactly the same whereas the reflected fields in the *y* direction, $\boldsymbol{r}_{yy}\boldsymbol{E}_y$, have a 180° phase shift when comparing LCP to RCP. As a result, the total reflected field intensities are the same for LCP and RCP and the material exhibits no circular dichroism (Fig. 4.3b). This can also be confirmed by the fact that this system is non-chiral due to the existence of two mirror symmetry planes in the system.

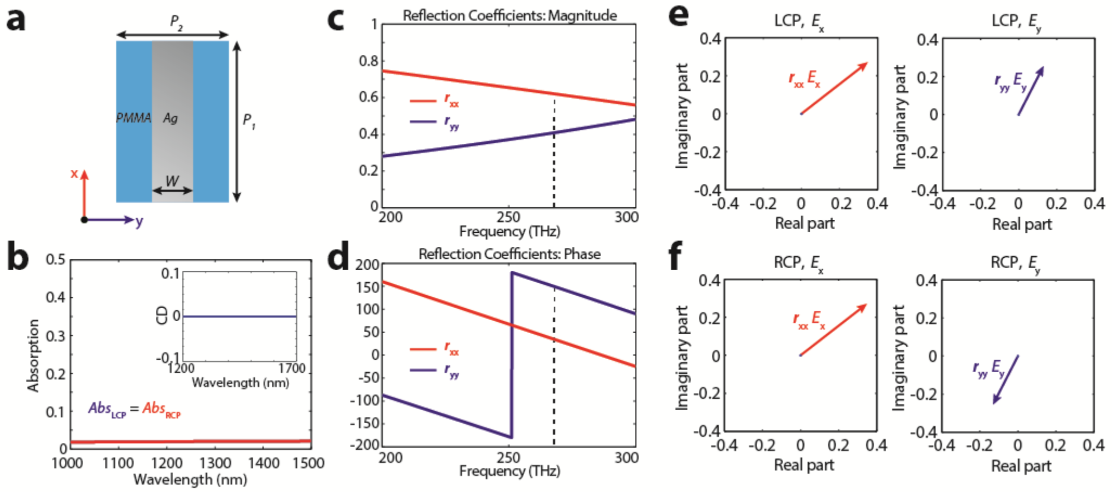

Figure 4.3. Optical response of silver stripes without a metal ground plane. a, Schematic of a unit cell consisting of a silver stripe. Dimensions are P_1 = 630 nm, P_2 = 440 nm, W = 160 nm and the thickness of the silver stripes is 40 nm. Background material is PMMA (n = 1.47). b, Absorption spectra of LCP and RCP light. Inset shows the CD spectra. c,d, Amplitude (c) and phase (d) of reflection coefficients for $\boldsymbol{E}_x$ and $\boldsymbol{E}_y$. e,f, Vector plots of the reflected fields $\boldsymbol{r}_{xx}\boldsymbol{E}_x$ and $\boldsymbol{r}_{yy}\boldsymbol{E}_y$ under LCP (e) and RCP (f) illumination at a frequency of f = 267 THz.

To break the mirror symmetry of system, we cut two rectangles from the two diagonal corners of the silver stripe in the unit cell, forming a ‘Z’ shaped antenna as shown in Fig. 4.4a. As a result, there is no mirror symmetry plane in the *xy* plane. Under linearly polarized light illumination (Fig. 4.4c,d), one can see that this system is capable of rotating a linear polarization state into its orthogonal one. The polarization conversion coefficients are labeled as $\boldsymbol{r}_{xy}$ and $\boldsymbol{r}_{yx}$ and represent the conversion from $\boldsymbol{E}_y$ to $\boldsymbol{E}_x$, and $\boldsymbol{E}_x$ to $\boldsymbol{E}_y$, respectively. The polarization conversion coefficients for two orthogonal fields are identical$\left(\boldsymbol{r}_{xy} = \boldsymbol{r}_{yx}\right)$. As a result, four reflected field components were observed: the unconverted scattered fields, $\boldsymbol{r}_{xx}\boldsymbol{E}_x$, $\boldsymbol{r}_{yy}\boldsymbol{E}_y$ and converted scattered fields, $\boldsymbol{r}_{yx}\boldsymbol{E}_x$, $\boldsymbol{r}_{xy}\boldsymbol{E}_y$(Fig. 4.4c,d).

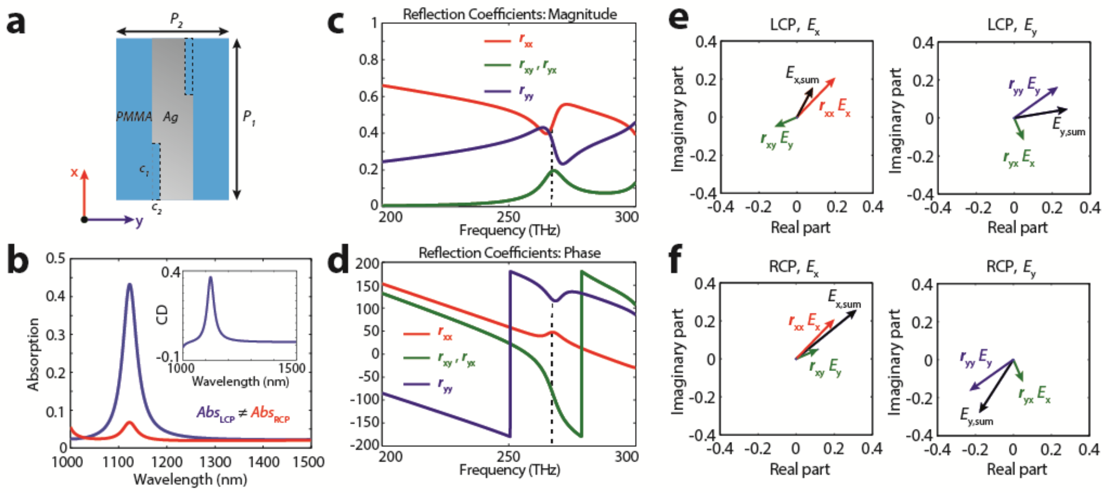

Figure 4.4. Optical response of 'Z' shaped metamaterial without a metal ground plane. a, Schematic of of a 'Z' shaped antenna unit cell. The dimensions are $C_1 = 220$ nm and $C_2 = 30$ nm. The other dimensions are the same as Fig. 4.3a. Background material is PMMA (n = 1.47). b, Absorption spectra of LCP and RCP light. Inset shows the CD spectra. c,d, Amplitude (c) and phase (d) of the reflection coefficients for $\boldsymbol{E}_x$ and $\boldsymbol{E}_y$. e,f, Interference between the unconverted scattered field, $\boldsymbol{r}_{xx}\boldsymbol{E}_x$,(or $\boldsymbol{r}_{yy}\boldsymbol{E}_y$) and the converted scattered field, $\boldsymbol{r}_{xy}\boldsymbol{E}_y$,(or $\boldsymbol{r}_{yx}\boldsymbol{E}_x$), under LCP (e) and RCP (f) illumination at a frequency of f = 267 THz.

When the structure is illuminated with circularly polarized light, the unconverted scattered field, $\boldsymbol{r}_{xx}\boldsymbol{E}_x$,(or $\boldsymbol{r}_{yy}\boldsymbol{E}_y$) will interfere with the converted scattered field, $\boldsymbol{r}_{xy}\boldsymbol{E}_y$,(or $\boldsymbol{r}_{yx}\boldsymbol{E}_x$). The reflected field with $\boldsymbol{E}_x$ or $\boldsymbol{E}_y$ polarization can be represented as,

$$E_{x,sum} = \boldsymbol{r}_{xx}\boldsymbol{E}_x + \boldsymbol{r}_{xy}\boldsymbol{E}_y \tag{4.3}$$

$$E_{y,sum} = \boldsymbol{r}_{yy}\boldsymbol{E}_y + \boldsymbol{r}_{yx}\boldsymbol{E}_x \tag{4.4}$$

Here, we use the vector field plots to illustrate the interference for both LCP and RCP. As can be seen in Fig. 4.4e, for the case of LCP illumination (the phase of $\boldsymbol{E}_x$ is 90° ahead of $\boldsymbol{E}_y$) the unconverted scattered field, $\boldsymbol{r}_{xx}\boldsymbol{E}_x$, will destructively interfere with the converted scattered field, $\boldsymbol{r}_{xy}\boldsymbol{E}_y$, resulting in a reduced total reflected field ($E_{x,sum}$). However, for the case of RCP illumination (the phase of $\boldsymbol{E}_y$ is 90° ahead of $\boldsymbol{E}_x$) as shown in Fig. 4.4f, the unconverted scattered field, $\boldsymbol{r}_{xx}\boldsymbol{E}_x$, will constructively interfere with the converted scattered field, $\boldsymbol{r}_{xy}\boldsymbol{E}_y$, resulting in an enhanced total reflected field ($E_{x,sum}$). The asymmetric interference results in different absorption for LCP and RCP as shown in Fig. 4.4b. As a result, a circular dichroism of about 0.35 for this single layer system is obtained.

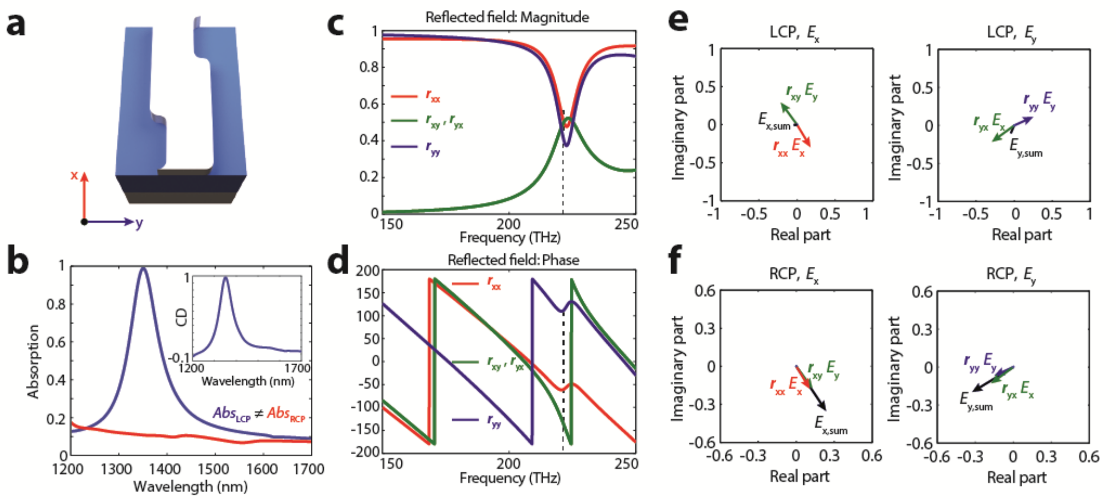

Figure 4.5. Optical response of the 'Z' shaped chiral metamaterial with a metal ground plane. a, Schematic of a unit cell of the chiral metamaterial with metal ground plane, same as Fig. 4.1a. b, Absorption spectra of LCP and RCP light. Inset shows the CD spectra. c,d, Amplitude (c) and phase (d) of the reflection coefficients for $\boldsymbol{E}_x$ and $\boldsymbol{E}_y$. e,f, Interference between the unconverted scattered field, $\boldsymbol{r}_{xx}\boldsymbol{E}_x$,(or $\boldsymbol{r}_{yy}\boldsymbol{E}_y$) and the converted scattered field, $\boldsymbol{r}_{xy}\boldsymbol{E}_y$,(or $\boldsymbol{r}_{yx}\boldsymbol{E}_x$), under LCP (e) and RCP (f) illumination at a frequency of f = 223 THz.

To further enhance the circular dichroism, we added a metal ground plane and a dielectric spacer to the 'Z' shaped chiral metamaterial. Meanwhile, the structure's dimensions were adjusted to account for the different background materials (silicon and PMMA), the wavelength of interest (1200 nm to 1500 nm) and the fabrication resolution (blend angle) as shown in Fig. 4.5a. The metal backplane blocks the transmission and forms a Fabry-Perot cavity leading to multiple reflections within the film. We tracked the reflected electric field evolution as a function of the number of reflections between the structure and the metal backplane as shown in Fig. 4.2e,f. The multiple reflections further enhance (LCP) or reduce (RCP) absorption, leading a circular dichroism up to 0.9 (Fig. 4.5b). This can also be confirmed by investigating the reflection coefficients (Fig. 4.5c,d) and the interference effects (Fig. 4.5e,f) as we consider the single layer 'Z' shaped chiral metamaterial along with the metal ground plane as a single system. As can be seen in Fig. 4.5e, for the case of LCP ($\boldsymbol{E}_x$ is 90° phase ahead of $\boldsymbol{E}_y$), the unconverted scattered field $\boldsymbol{r}_{xx}\boldsymbol{E}_x$,(or $\boldsymbol{r}_{yy}\boldsymbol{E}_y$) will destructively interference with converted scattered field $\boldsymbol{r}_{xy}\boldsymbol{E}_y$,(or $\boldsymbol{r}_{yx}\boldsymbol{E}_x$), esulting in a reduced total reflected field for both $E_{x,sum}$ and $E_{y,sum}$. An opposite situation is observed for the case of RCP ($\boldsymbol{E}_x$ is 90° phase after $\boldsymbol{E}_y$) as shown in Fig. 4.5f. The strong asymmetric interference effect results in different absorption for LCP and RCP. As a result, a circular dichroism of about 0.9 is obtained as shown in Fig. 4.5b.

In an ideal case, under LCP illumination, the unconverted scattered field, $\boldsymbol{r}_{xx}\boldsymbol{E}_x$(or $\boldsymbol{r}_{yy}\boldsymbol{E}_y$) should be exactly out of phase (180° phase shift) with the converted scattered field $\boldsymbol{r}_{xy}\boldsymbol{E}_y$(or $\boldsymbol{r}_{yx}\boldsymbol{E}_x$) while maintaining the same amplitude to completely cancel out the reflected field. Whereas for the case of RCP, the unconverted scattered field, $\boldsymbol{r}_{xx}\boldsymbol{E}_x$(or $\boldsymbol{r}_{yy}\boldsymbol{E}_y$) should be exactly in phase (0° phase shift) with the converted scattered field, $\boldsymbol{r}_{xy}\boldsymbol{E}_y$(or $\boldsymbol{r}_{yx}\boldsymbol{E}_x$), to achieve maximum reflection. The field vectors under these ideal conditions are illustrated in Fig. 4.6.

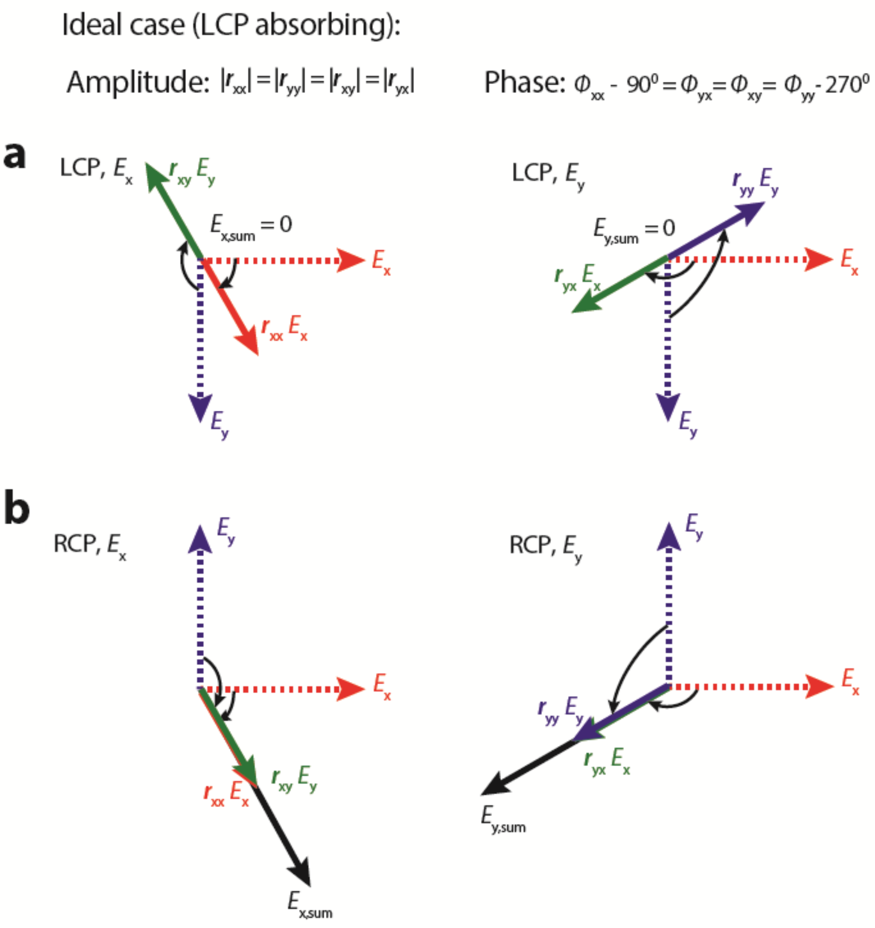

Figure 4.6. Ideal conditions for maximizing circular dichroism in planar chiral metamaterials. Completely destructive (a) and constructive (b) interference between the unconverted scattered field, $\boldsymbol{r}_{xx}\boldsymbol{E}_x$, (or $\boldsymbol{r}_{yy}\boldsymbol{E}_y$) and the converted scattered field, $\boldsymbol{r}_{xy}\boldsymbol{E}_y$,(or $\boldsymbol{r}_{yx}\boldsymbol{E}_x$) under LCP (a) and RCP (b) illumination. Dashed lines represent the initial incident field vectors $\boldsymbol{E}_x$ and $\boldsymbol{E}_y$ with a 90° phase shift. Solid lines represent the reflected field vectors.

From Fig. 4.6, we can summarize the ideal conditions for maximizing circular dichroism (maximizing LCP absorption, minimizing RCP absorption) in this planar chiral metamaterial as:

$$|\boldsymbol{r}_{xx}| = |\boldsymbol{r}_{xy}| = |\boldsymbol{r}_{yx}| = |\boldsymbol{r}_{yy}| \tag{4.5}$$

$$\phi_{xx} - 90° = \phi_{xy} = \phi_{yx} = \phi_{yy} - 270° \tag{4.6}$$

For the case of maximizing RCP absorption and minimizing LCP absorption, the ideal conditions will be:

$$|\boldsymbol{r}_{xx}| = |\boldsymbol{r}_{xy}| = |\boldsymbol{r}_{yx}| = |\boldsymbol{r}_{yy}| \tag{4.7}$$

$$\phi_{xx} + 90° = \phi_{xy} = \phi_{yx} = \phi_{yy} + 270° \tag{4.8}$$

These conditions set several requirements for the planar metamaterial. First, the metamaterial needs to possess linear polarization conversion to produce the converted field. Second, the metamaterial needs to be anisotropic in order to produce the phase difference. Third, the metamaterial needs to be lossy. Any planar metamaterial that fulfills these three requirements will exhibit circular dichroism.

It should be noted that the ‘Z’ shaped antenna array was chosen due to the fact that the array needs to be electrically connected for hot electron photodetection. There are many alternative geometries that can produce the same optical properties. For example a 45° tilted dipole antenna[168] can be combined with vertically aligned dipole antennas or three dipole antennas with varying relative displacements could be used. Each of these geometries can result in a circular dichroism up to 0.9. The circular dichroism is only limited by the material damping of the plasmonic materials.

4.4 Photodetector performance

The high circular dichroism in the chiral metamaterial directly leads to enhanced discrimination between LCP and RCP in the CPL photodetectors. To demonstrate this, we fabricated both LH and RH chiral metamaterial arrays (Fig. 4.7a,b) on the bottom side of a double side polished <100> n-type silicon (Si) wafer (500 μm thick, 1–10 Ωcm). The double-side polished wafer is chosen to allow light illumination from the front side of the wafer without inducing scattering. After spin coating the substrate with 130 nm thick PMMA, the antennas were defined using EBL. The LH and RH arrays had an overall area of 70 µm x 70 µm and the VU Logo array was 90 µm x 90 µm. After cold development in MIBK:IPA 1:3, the sample was cleaned with an IPA rinse and dried under a N_2 stream. The sample was immersed in 10:1 buffered oxide etchant (BOE) for 10s to completely remove the native oxide from the Si. It was then immediately transferred into an evaporation chamber followed by evaporation of 1 nm Ti and co-deposition of a 35 nm thick Al-doped silver film. Aluminum-doped silver was used due to the fact that it helps to reduce the silver film roughness and grain size while also facilitating the formation of an Al_2O_3 passivation layer that protects the silver from corrosion[169]. The silver deposition rate was 2 Å/s and the aluminum deposition rate was 0.2 Å/s, leading to an aluminum concentration of about 9%. After the co-deposition a lift-off process was used to yield the structures shown in Fig. 4.7a,b. The obtained meta-molecule dimensions are L_1 = 130 nm, L_2 = 110 nm, W_1 = 110 nm, W_2 = 80 nm, P_1 = 350 nm, P_2 = 230 nm. Finally, a 160 nm thick PMMA spacer layer was created by spin coating and followed by thermal evaporation of a 100 nm thick silver backplane.

The experimentally measured optical absorption spectrum of both the LH and RH metamaterial reveals the same absorption bands demonstrated in the simulations. For the LH metamaterial there is a resonance leading to near unity absorption of LCP light at 1340 nm, whereas RCP light is largely reflected (Fig. 4.7d). The RH metamaterial shows a nearly opposite optical response (Fig. 4.7e). One will notice that the off-resonant absorption is increased compared to the simulation. This is due to the increased material loss, induced by the aluminum doping of silver and an interfacial 1 nm Ti layer. Even with the slightly increased off-state absorption, the metamaterial still possesses a circular dichroism of 0.72 at 1340 nm (Fig. 4.7f), among the highest reported for chiral metamaterials.

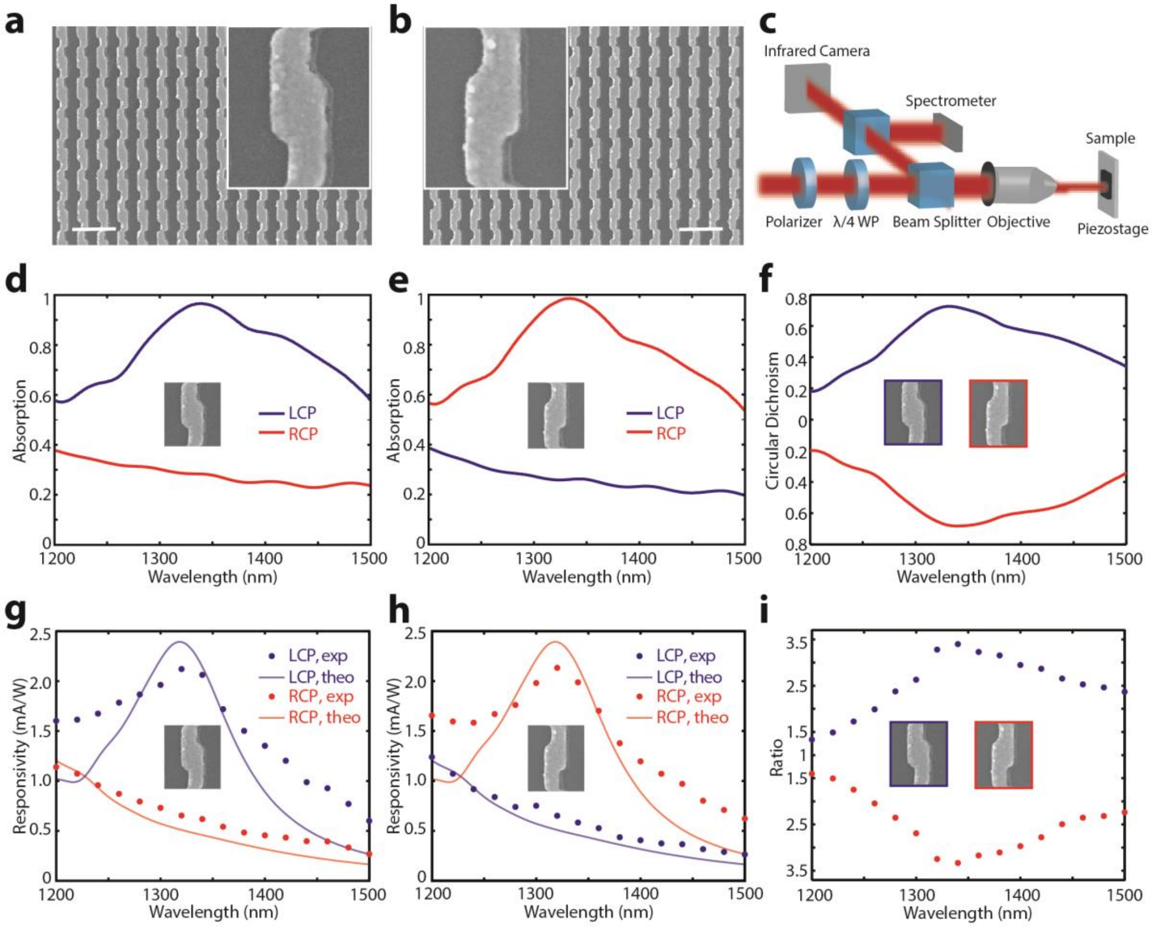

Figure 4.7. (a) Experimentally measured optical absorption and photoresponsivity spectra. a,b, SEM images of the LH (a) and RH (b) metamaterial before spin-coating the PMMA spacer layer. The inset shows a unit cell of the chiral metamaterial. The scale bar is 500 nm. c, Schematic of experimental setup. d,e, Experimentally measured optical absorption spectra under LCP (blue) and RCP (red) illumination for LH (d) and RH (e) metamaterials. f, Experimentally measured circular dichroism spectra for both LH (blue) and RH (red) metamaterials. g,h, Experimentally measured (dots) and theoretically calculated (solid curve) photoresponsivity spectra under LCP (blue) and RCP (red) illumination for LH (g) and RH (h) metamaterials. i, Photocurrent polarization discrimination ratio spectra of LH and RH metamaterials. The metamaterials measured have overall areas of 70 µm x 70 µm.

Photoresponse spectra of the devices were obtained by illuminating the metamaterials with a circularly polarized laser and measuring photocurrent as a function of the laser handedness and wavelength. The photoresponsivity spectrum (Fig. 4.7g,h) matches well with the measured absorption spectrum. The peak photoresponsivity of the resonant state reaches 2.2 mA/W, corresponding to a quantum efficiency of about 0.2% and it is comparable to other Schottky diode based LPL photodetectors working in this wavelength regime[3], [48]. This efficiency is two times that of chiral organic semiconductor transistors[155] and can be further improved with optimization[167], [123]. Furthermore, the large circular dichroism translates to a correspondingly large distinction in the photocurrent for LCP and RCP light with a polarization discrimination ratio of 3.4 (Fig. 4.7i) and a difference in photoresponsivity of 1.5 mA/W, demonstrating the ability to detect and distinguish between left and right hand CPL in an ultracompact detector geometry. It should be noted that the photoresponsivity of this device under non-CPL excitation is about 1.4 mA/W, which is the average value of the resonant and off-resonant polarization state responsivity due to the fact that LPL can be decomposed into two CPL beams with opposite handedness. It is also important to note that although our device responsivity is still low compare to the non-chiral, semiconductor InGaAs or Ge detector (~900 mA/W) in the similar regime, the later is not able to distinguish CPL. Similar functionality could also be done by integrating semiconductor with chiral metamaterial, leading to chiral-selective absorption in semiconductor. However, it does not necessarily produce high polarization selectivity[158] (Appendix B.3) even though higher quantum efficiency could be realized.

The theoretical photoresponsivity spectra were calculated (solid curve in Fig. 4.7g,h) based on the creation of energetic electrons due to the collisions with the interface potential wall between the metal and the silicon substrate[73], [74]. Local injection current maps were calculated and the total injected current is obtained by integrating over the Schottky interface (Appendix B.4). The general trend of the experimental measurements and the theoretically calculated photoresponsivity spectra agrees well, although a resonance broadening is observed in the experimental results. This follows well with the inhomogeneous broadening of the experimentally measured optical absorption spectra compared to simulations and is most likely due to fabrication imperfections in the metamaterial.

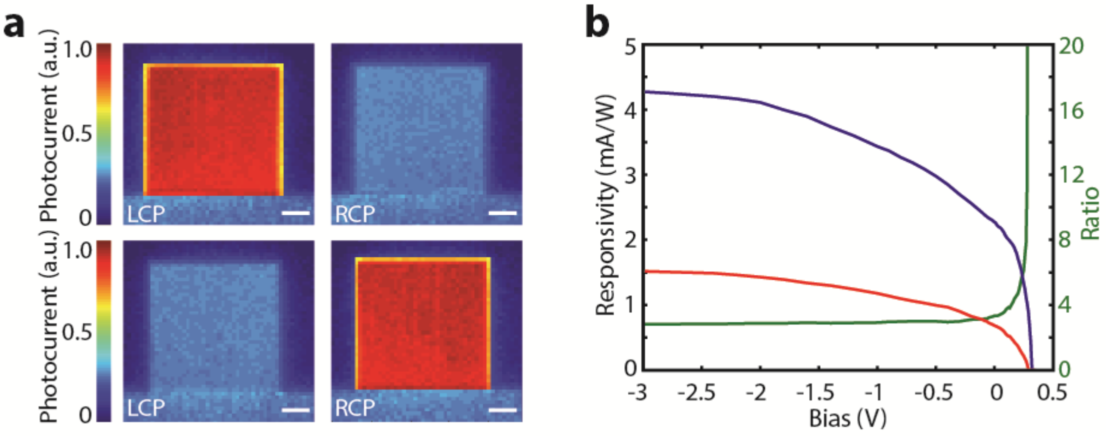

Figure 4.8. (a) Spatial scanning and bias dependent photocurrent. a, Scanning photocurrent map of LH (top) and RH (bottom) metamaterials under LCP and RCP illumination. The scale bar is 15 µm. b, Bias dependency of photocurrent of a LH metamaterial for LCP (blue) and RCP (red) light under a laser power of 1.5 mW. The green curve shows the polarization discrimination ratio versus bias.

Photocurrent maps were also measured by scanning a focused circularly polarized laser across the array and monitoring photocurrent as a function of spatial position. As can be seen in Fig. 4.8a, clear distinctions in photocurrent for LCP and RCP light are observed for both LH and RH metamaterials. The photocurrent of the chiral metamaterials under the off-resonant polarization is similar to the un-patterned silver bus bar which confirms the non-resonant behavior of the structure. The off-array photocurrent is within the noise level of the measurements which confirms that direct absorption in the silicon is negligible. Furthermore, photocurrent measurements under different laser powers (Appendix B.5) show good linearity, excluding any non-linear interactions. It also indicates the detector's ability to work over a wide range of incident power, overcoming saturation issues found in chiral organic semiconductors[155].

As an added benefit, Schottky-diode-based photodetectors can provide photocurrent tuning through the application of a source-drain bias to the device[49], [126], [123], [124] offering flexibility in controlling the polarization discrimination ratio and photoresponsivity. As shown in Fig. 4.8b, when a negative bias was applied, both the LCP and RCP photocurrent were increased, leading to an increased difference in photoresponsivity. When a positive bias was applied, despite the decrease in absolute photocurrent, the polarization discrimination ratio or the selectivity can be dramatically increased. These measurements indicate how one can generally trade photoresponsivity for a larger polarization discrimination ratio, or vice versa, to meet different application requirements.

4.5 Integrated device performance

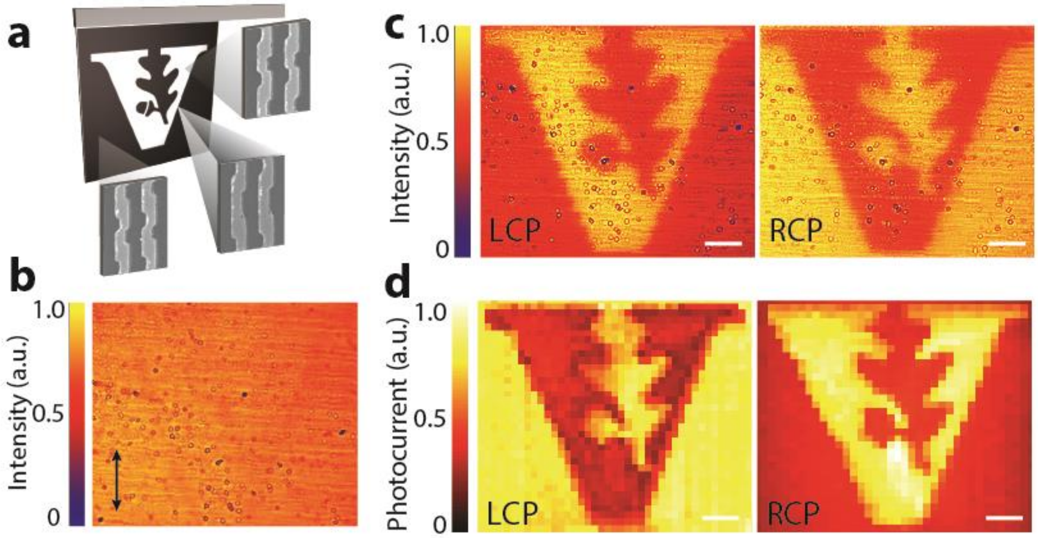

Figure 4.9. CPL detector with RH and LH elements patterned into the Vanderbilt University logo. a, Schematic of the pattern with the LH metamaterial filling the black region and the RH metamaterial filling the white region. b, Camera image of the metamaterial under linearly polarized light with polarization along the vertical direction. c, Camera images of the metamaterial under LCP (left) and RCP (right) illumination. d, Scanning photocurrent maps of the metamaterial under LCP (left) and RCP (right) illumination. The scale bar is 10 μm.

Since the chirality of our metamaterial originates from the structure of the antenna layer, instead of an intrinsic material chirality, multiple meta-molecules can be incorporated into a single device to achieve multiple functionalities including CPL, LPL, and wavelength selectivity, with only one patterning step. As a proof of concept, we placed LH and RH chiral meta-molecules into a single array to form a spatially non-uniform, pixelated photodetector. The fabricated array is 90 μm x 90 μm, containing roughly 100,621 unit cells. The array was implemented with both LH and RH enantiomers that were patterned to create the Vanderbilt University logo (Fig. 4.9a), where the LH and RH enantiomers fill the black and white regions of the logo, respectively. The shape of our chiral meta-molecules also allows for an electrically connected transition between the opposite-handed enantiomers. As a result, an image of the ‘V’ logo, which doesn’t appear under linearly polarized (Fig. 4.9b) or un-polarized light, shows a very clear contrast in reflection under LCP and RCP light (Fig. 4.9c). The performance of this integrated detector was evaluated using scanning photocurrent measurements with focused circularly polarized laser illumination. Good contrast is observed in the photocurrent scanning maps for LCP and RCP (Fig. 4.9d), indicating the ability to integrate multiple chiral plasmonic meta-molecules into a single ultracompact device.

4.6 Conclusion

In summary, we have demonstrated a circularly polarized light detector based on the engineered circular dichroism in plasmonic nanostructures and the hot electron transfer process. This solid-state hot electron based chiral metamaterial CPL detector holds the promise of integration, robust and tunable operation[3], [46], [48], and a large polarization discrimination. Combining our CPL detector with current existing linearly polarized light hot electron photodetectors[3], [46], [48], [124] could lead to an integrated hot electron polarimeter with the ability to determine the Stokes parameters or the states of polarization of an arbitrarily polarized beam[158]. These CPL detectors could be used in applications ranging from encoded fiber optic and free-space communications to polarimetric imaging, emission and sensing applications using circularly polarized light. In addition, the sub-wavelength thin planar chiral metamaterials we proposed here demonstrated the largest circular dichroism ever reported. We can understand the origin of this giant circular dichroism using interference theory and have proposed a design rationale for designing large circular dichroism in planar chiral metamaterials, which can potentially be useful in a variety of chiral selective applications.

Chapter 5 Conclusion and Outlook

The focus of this thesis research has been to show how one can harvest the loss of plasmonics, which was once thought to be parasitic, to use it in plasmonic photothermal and photoelectrical conversion systems and how the performance can be significantly improved by engineered plasmonic nanostructures. In this chapter, I will summarize my work as well as outline several promising research directions in the field.

5.1 Summary

In Chapter 2, we proposed a design rationale for converting plasmonic nanoparticles into efficient nanoscale heat sources. The design rationale is based on Babinet's principle, which allows one to readily convert any good electromagnetic antenna into a good thermal antenna. It provides a simple design criterion to realize both large heat source density and local temperatures in plasmonic nanostructures and can potentially be used in cancer therapy, heat-assisted magnetic recording and chemical catalysis processes. We also developed a nanoscale thermal microscopy technique based on thin film thermographic phosphors with a temperature dependent photoluminescence lifetime. This thermal microscopy method allows for probing large temperature changes in a robust measurement scheme and could potentially see widespread adoption in micro/nanoscale science.

In Chapter 3, we detailed our efforts to enhance the efficiency of hot electron devices by engineering the plasmonic nanostructures with strong resonant optical absorption and hot carrier generation at the Schottky interface. Specifically, we proposed and experimentally demonstrated a metamaterial perfect absorber geometry exhibiting near unity absorption of light within an ultrathin 15nm metal film. Realizing near unity absorption within ultrathin plasmonic nanostructures allows the efficiency of the hot electron transfer process to be significantly enhanced, resulting in hot electron detectors with photoresponsivity that are among the highest reported. The metamaterial perfect absorber geometry we proposed here also eliminates the need of a metal backplane, and therefore can potentially be used for enhancing light absorption in a wide range of substrate materials where a high temperature growing process is required, such as high quality semiconductors. The hot electron detector devices demonstrated here can also be translated into hot electron based photocatalysis and photovoltaic systems.

In Chapter 4, we demonstrated an ultracompact circularly polarized light detector by combining the engineered chirality of chiral metamaterials and the hot electron injection process. We experimentally demonstrated this integrated detector's ability to convert the handedness of circular polarization into electrical signals without the need for bulk optical elements such as a quaterwave plates and linear polarizers. This detector can potentially be used for chiral molecular sensing as well as enhanced bandwidth in optical communications. In addition, the sub-wavelength planar chiral metamaterials we proposed here demonstrated the largest circular dichroism ever reported. We interpreted this giant circular dichroism using interference theory and proposed a design rationale for designing large circular dichroism in planar chiral metamaterials, which can potentially be useful in a variety of chiral selective applications.

5.2 Future Outlook

Research on plasmonics has experienced much progress over the past decade in controlling and manipulating light emission, absorption and propagation. While ohmic loss was once thought to be parasitic, in recent years, as outlined in this thesis, the focus has shifted toward harvesting the loss of plasmonics in the form of hot electrons or local heating. Despite the success, there are still many open opportunities in this area to be explored. Here I will briefly discuss some opportunities and challenges.

One of the major challenges in this area is to further improve plasmonic hot electron energy conversion efficiency. Over the past several years, there have been significant efforts to improve the efficiency. However, further improvement in device performance is still needed to address practical applications. Progress will require improving the efficiency of hot carrier generation and the subsequent transport and injection processes. This involves both the intelligent design of plasmonic nanostructures as well as a better fundamental understanding of the hot carrier generation, transport and extraction processes.

In terms of plasmonic design, ways to further enhance the field concentration and absorption in ultra-thin or small nanoparticles are needed[3], [46], [170]. In terms of hot carrier transport, employing higher quality noble metals[171], [172] or exploring new plasmonic materials[77] could potentially result in longer hot carrier diffusion lengths. Hot electrons can also experience significant reflection as a result of the large wavevector contrast at the metal-dielectric interface. As such, more work is needed in the design of plasmonic nanostructures that support the generation of hot electrons with a momentum distribution that matches well with band structure of the semiconductor.

At the same time, a more fundamental understanding of hot carrier generation, transport and emission is still needed for designing efficient hot carrier devices. For hot carrier distribution, while much work has been devoted to providing theoretical predictions of hot carrier distribution in plasmonic nanostructures[72]–[74], [76], [77], more experimental work is needed to validate these models. There have also been experimental demonstrations indicating that plasmon-induced hot carriers result in higher-energy electrons than direct excitation[71], that are in need of a theoretical model. In addition, a better understanding of the hot carrier relaxation timescale[78], [128], [173] in various materials, as well as the transport dynamics in nanostructures would provide more valuable information for designing plasmonic devices with efficient hot carrier transport to the Schottky interface. Lastly, engineering the metal-semiconductor interface on the atomic level could also lead to improved hot electron transfer efficiencies[174], [175]. Recent report on efficient hot-electron transfer by a plasmon-induced interfacial charge-transfer transition has shown an internal quantum efficiency up to 20% independent of incident photon energy[174]. I believe that advances in these areas should lead to a wealth of opportunities and scientific breakthroughs in the future.

Appendix A: Perfect Absorber Hot Electron Detector

A.1 Device fabrication

In contrast with previously reported metamaterial perfect absorber structures[129], [130], [176] which require a pre-deposited dielectric spacer and optically thick metal backplane, our device was fabricated using single step planar lithography and reactive ion etching of the substrate. A double side polished <100> n-type silicon (Si) wafer (500mm thick, 1–10Ωcm) was used as substrate. After spin coating the substrate with 60nm PMMA, the reverse patterns were defined using EBL. Each metamaterial array was defined as 85um x 85um. After cold development in MIBK:IPA 3:1, the sample was cleaned with an IPA rinse and dried under an N_2 stream. The PMMA was then used as a mask for RIE with an (radio frequency) RF power of 70W, pressure 25mW and SF_6 gas flow of 10sccm. The sample was immersed in 10:1 buffered oxide etchant (BOE) for 1 minute to completely remove the native oxide. It was then immediately transferred into the evaporation chamber followed by evaporation of 1nm Ti and 15nm Au with a shadow mask. The entire process is summarized in Fig. A.1.

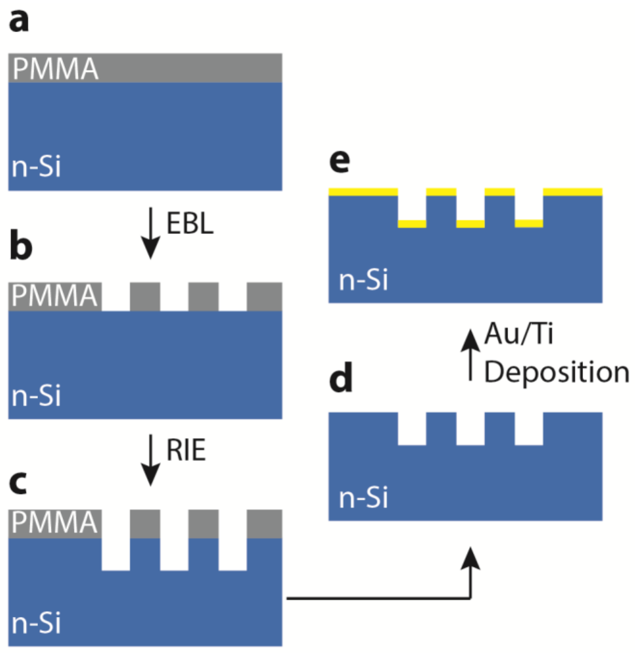

Figure A.1. (a) PMMA spin coating on the n-Si substrate. (b) EBL patterning using PMMA as the resist. (c) Reactive ion etching. (d) PMMA and native oxide removal. (e) Metal deposition.

A.2 Optical characterization of the metamaterial perfect absorber

The optical absorption spectrum of the device was performed by measuring the reflection *R* and transmission *T* in an infrared microscope coupled to a grating spectrometer (Horiba, iHR320). The reflection spectra are normalized to a silver mirror and the transmission spectra are normalized to air. The absorption spectra were obtained by subtracting reflection *R* and transmission *T* from unity. The experimentally measured reflection and transmission spectra for the 1D, 2D, and broadband MPA devices are shown in Fig. A.2.

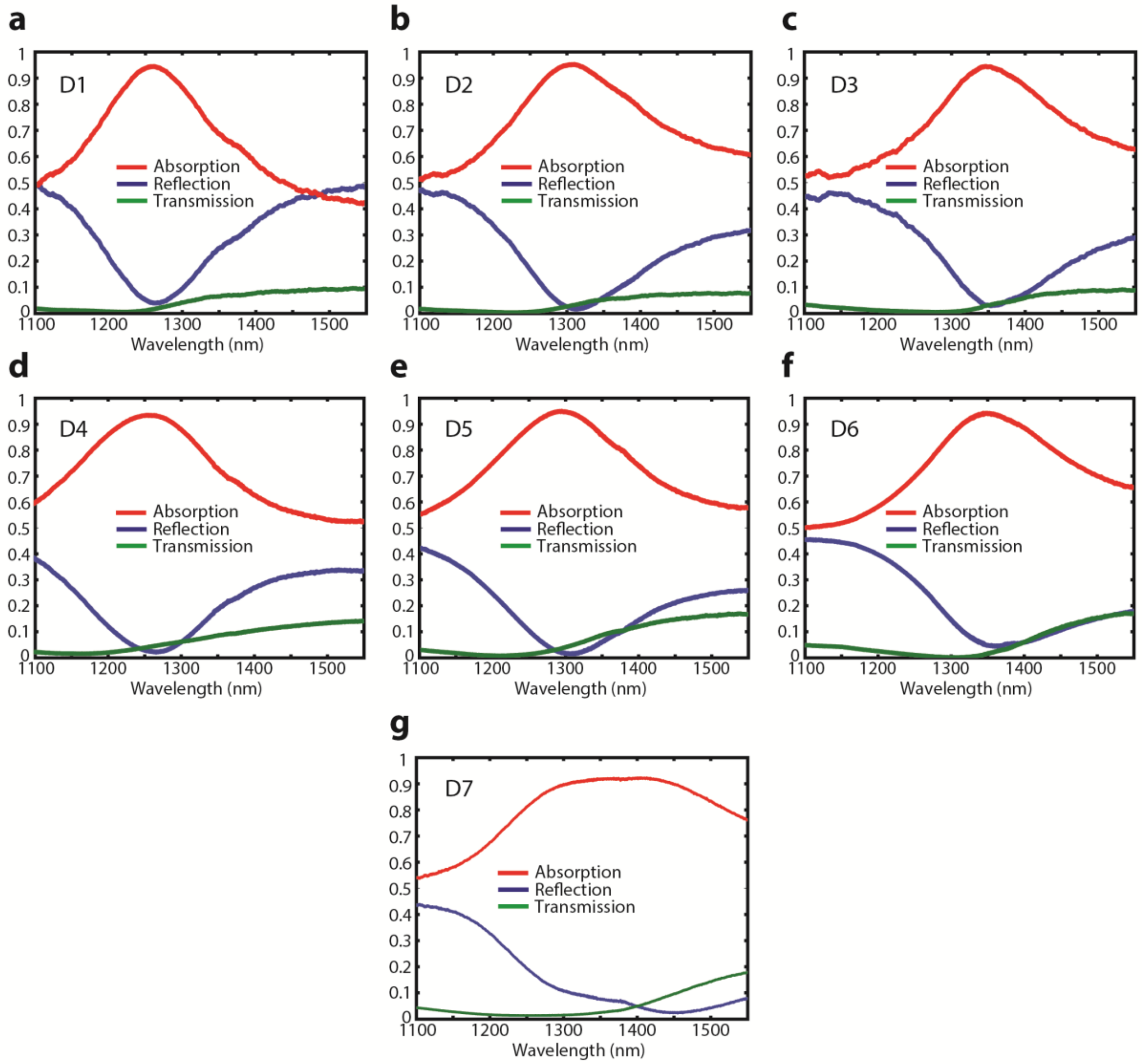

Figure A.2. Experimental measured reflection, transmission and absorption spectrum of (a)-(c) 1D MPA detectors D1, D2, D3, (d)-(f) 2D MPA detectors D4, D5, D6 and (g) broadband MPA detector D7.

A.3 Optical absorption and hot electron distribution calculation

Full-wave electromagnetic simulations were performed using a commercially available software (CST Microwave Studio 2013). The unit cell of 1D, 2D, and broadband MPA detectors were investigated. Periodic boundary conditions were used along the *x* and *y*-axis and perfectly matched layers were used along the propagation directions. The optical parameters for Au and Ti were taken from Johnson and Christy[177], [178] and the damping was increased by three times to better match experimental thin film parameters. The optical parameters of the n-type Si substrate were taken from ellipsometry measurements.

To understand the optical absorption and hot electron generation distribution in the upper resonator and lower resonator in the MPA devices, we calculated the local Ohmic loss in the metal resonator layers using,

$$Q(r,\omega) = \frac{1}{2}\omega \mathrm{Im}(\varepsilon_m)\left|\vec{E}(r,\omega)\right|^2 \tag{A.1}$$

where the local Ohmic loss $Q(r,\omega)$ is a function of the local electric field intensity, $\vec{E}(r,\omega)$ and the imaginary part of the metal permittivity, $\mathrm{Im}(\varepsilon_m)$. Using this treatment we can calculate the absorption of upper and lower resonator layers, respectively, as well as the total absorption of the MPA device (Fig. A.3). This data is used for the theoretical photoresponsivity calculation in equation 3.1 in Chapter 3. As an example, we plot the absorption of the device D1 (Fig. A.3a) and the contributions from the upper and lower resonators (Fig. A.3b). The total absorption, obtained from S-parameter calculation as $A = 1 - R - T$ is also shown in Fig. A.3a, showing an excellent agreement with the ohmic loss calculation.

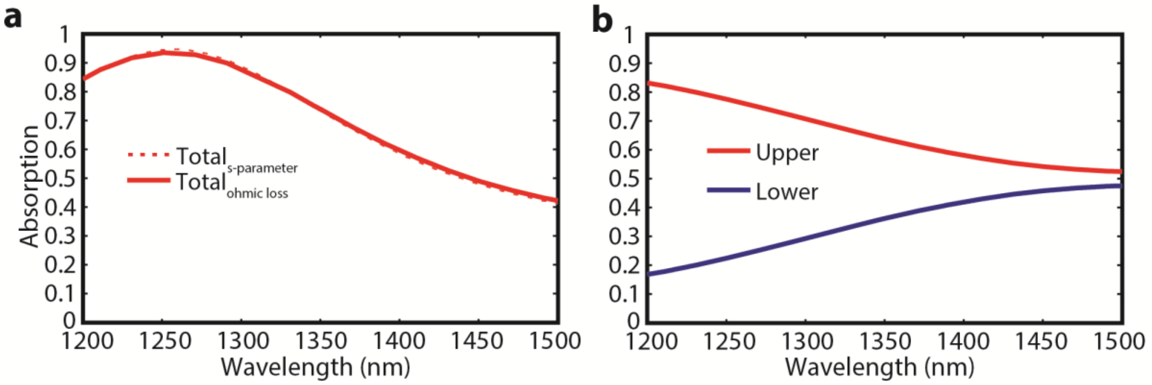

Figure A.3. Total optical absorption of MPA device obtained from ohmic loss and S-parameter calculation. (b) Absorption contribution in the MPA devices for the upper and lower resonator layers.

A.4 Incident angle dependent absorption spectra of MPA devices

We have shown the absorption spectrum of 2D MPA devices as a function of the incident angle in Fig. 3.4. Here, the absorption spectrum of the 1D MPA device (Fig. 3.1) for incident angles from 0 to 90 degrees for both *p* and *s*-polarized light are provided in Fig. A.4.

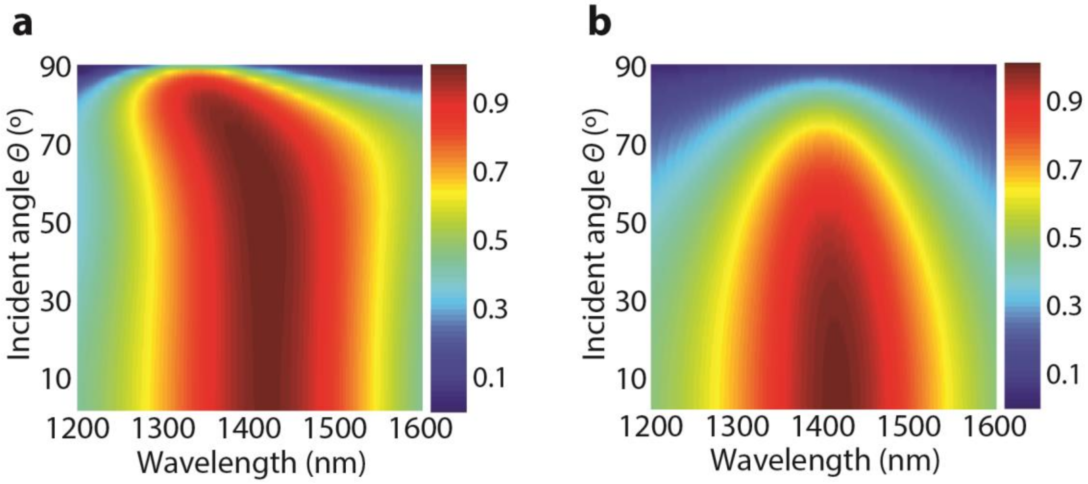

Figure A.4. Incident angle dependent absorption spectrum for the proposed 1D MPA for both (a) *p*-polarization and (b) *s*-polarization.

A.5 Electrical characterization

Here, we investigate the dependence of the photocurrent on the illumination power. The power-dependent photocurrent measurements was performed on device D2 with laser powers from 10uW to 5mW. A linear relation between the photocurrent and laser power was obtained as shown in Fig. A.5, indicating the absence of non-linear processes.

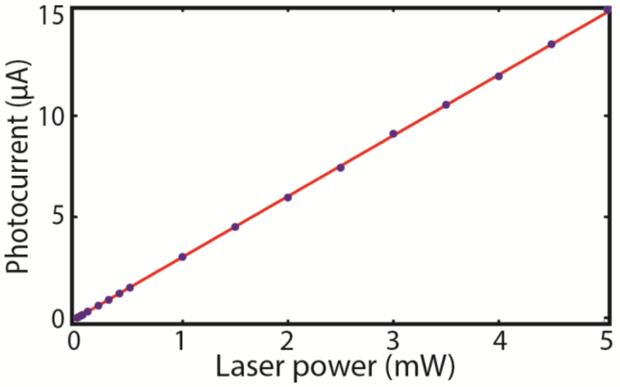

Figure A.5. Power dependent photocurrent of an MPA photodetector

An Ohmic contact on the n-type silicon substrate was achieved by indium soldering prior to the metal film deposition to prevent thermal damage to the thin metal film. After deposition, the sample was wire bonded to a chip carrier to perform the electrical characterization. The current-voltage measurements and photocurrent measurements were performed using a microscope, tunable laser, digital source meter (Keithley 2400), and lock-in amplifier (SR830). All of the photoresponsivity data reported in the manuscript were obtained without external bias. The Schottky barrier height, $q\phi_B$, is extracted as 0.54eV from current-voltage curve (Fig. A.6) of the MPA device using thermionic emission theory[60].

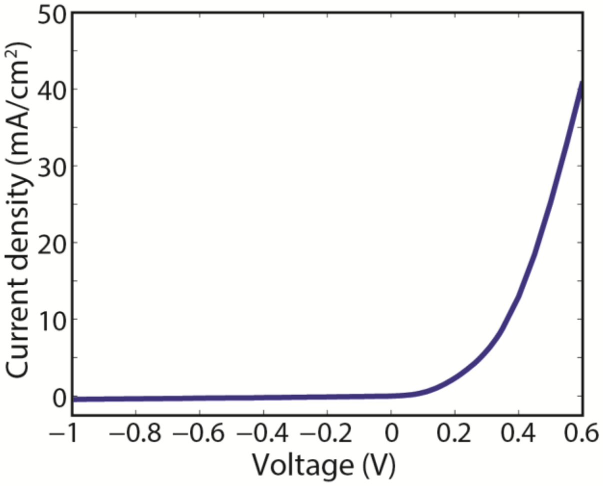

Figure A.6. Current-voltage characteristic of MPA device.

Appendix B: Circularly Polarized Light Detector

B.1 Circular conversion dichroism

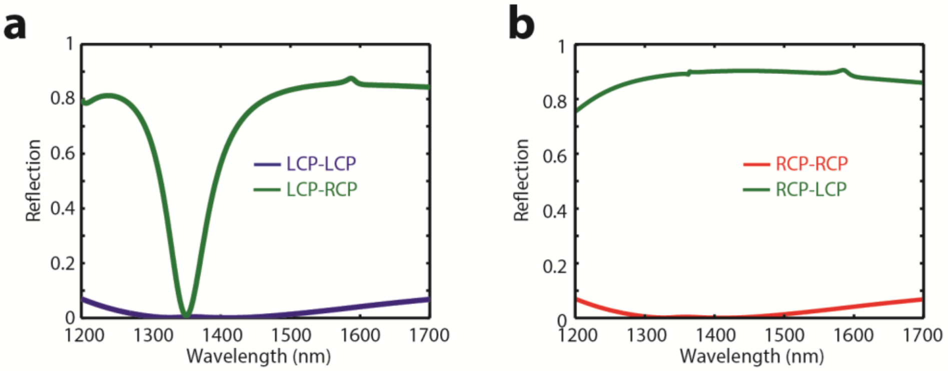

Figure B.1. Circular conversion dichroism of the chiral metamaterial. a, Under LCP illumination, the LCP reflection (blue) and LCP to RCP conversion (green) both go to minimum at the resonant wavelength, leading to the minimum total reflection field and maximum absorption. b, Under RCP illumination, the RCP reflection (green) is still minimum. However, there is a strong broadband polarization conversion from RCP to LCP (green). These simulations are performed on a LH metamaterial.

Here, we reexamine the proposed chiral metamaterial that is shown in Fig. 4.1a in Chapter 4. At the resonant frequency under RCP illumination ($\boldsymbol{E}_y$ is 90° phase ahead of $\boldsymbol{E}_x$) the phase of the reflected field, $E_{x,sum}$, will be about 90° ahead of $E_{y,sum}$ while the amplitudes of the two beams are roughly identical (Fig. 4.5f). As a result, the total reflected field becomes LCP. Therefore, there is a strong circular polarization conversion from RCP to LCP. However, in the case of LCP illumination, due to the destructive interference, conversion from LCP to RCP is not observed. Therefore, the strong asymmetric interference can also be viewed as the strong asymmetric conversion between LCP and RCP[160], [179], or circular conversion dichroism, as shown in Fig. B.1.

B.2 CD spectra versus incident angle

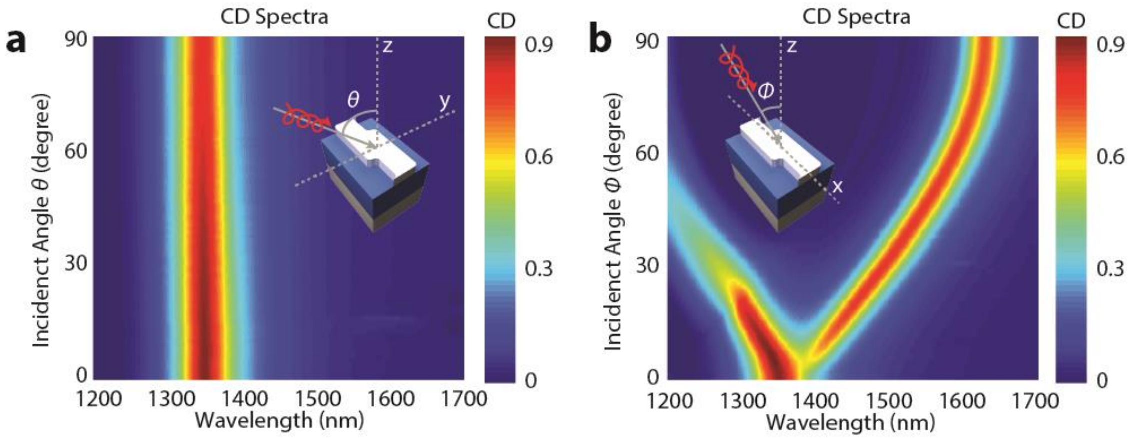

Figure B.2. Incident angle dependent circular dichroism for two different incidence directions. a, For incident light in the *yz* plane, the position of the CD peak is well maintained for all incident angles. b, For incident light in the *xz* plane, the CD spectra is maintained for a ~10° incident angle and further increasing the incident angle will shift the CD peak position. These simulations are performed on a LH metamaterial.

B.3 Chiral-selective absorption in semiconductor

It should be noted that the ability of distinguishing and detecting circularly polarized light can also be achieved by integrating a chiral metamaterial and a regular photodetector, leading to chiral-selective absorption and photocurrent in semiconductor. However, this approach does not necessarily produce high polarization selectivity even though higher quantum efficiency could be realized. To further expand on this point, we integrated our chiral metamaterial design with a semiconductor photodetector and investigated the direct absorption in the semiconductor. Specifically, we replaced the PMMA dielectric spacer with germanium, which serves as the semiconductor. We examined the total absorption as well as the absorption in germanium for LCP and RCP light, the simulation results are shown in Fig. B.3.

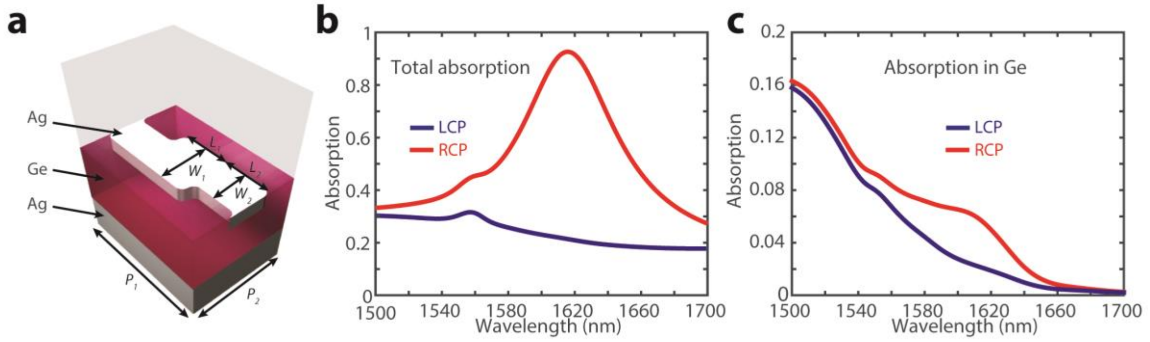

Figure B.3. Absorption spectra of the chiral metamaterial integrated with germanium. a, Schematic of the chiral metamaterial unit cell integrated with germanium. The dimensions are L_1 = 100 nm, L_2 = 110 nm, W_1 = 120 nm, W_2 = 80 nm, P_1 = 260 nm, P_2 = 340 nm. The thickness of the antenna, dielectric spacer and the metal back plane are 40 nm, 280 nm, and 100 nm respectively. b, Total absorption spectra of the chiral metamaterial for LCP (blue) and RCP (red) light. c, Absorption in germanium for LCP (blue) and RCP (red) light.

As we can see from Fig. B.3, the chiral metamaterial integrated with germanium can be designed to have the same type of resonance as we shown in Fig. 4.2 in Chapter 4. However, the absorption difference in germanium for LCP and RCP light is less than 0.05 at the resonance wavelength and the polarization selectivity is only about 2.5 based on the simulation. As a comparison, the simulated polarization selectivity of the chiral metamaterial (Fig. 4.2 in Chapter 4) is about 10. The relative low selectivity in this direction absorption mode compared to hot electron injection is mainly due to two reasons: 1) for the resonant polarization state, there is a competing process between the semiconductor absorption and the metal absorption. 2) for the non-resonant polarization state, there is still non-negligible direct absorption in semiconductor.

B.4 Photo-injection current calculation

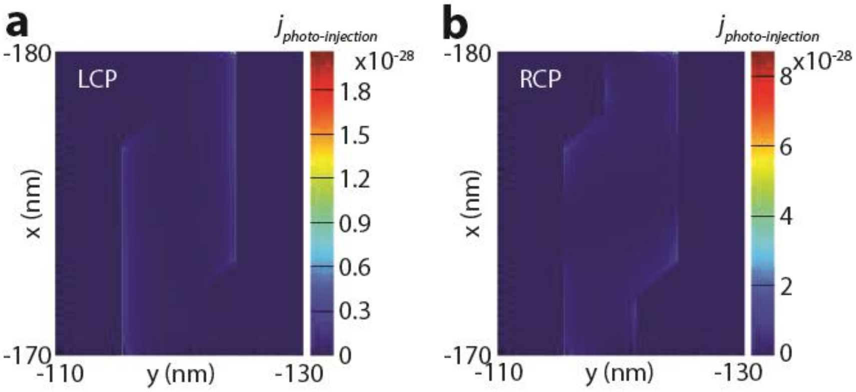

Figure B.4. Calculated maps of the local injection current. a, The local injection current map for a RH metamaterial under LCP illumination. b, The local injection current map for a RH metamaterial under RCP illumination. The theoretically modeled local injection current maps are given by the local normal electric field at the Schottky interface. The currents were calculated using, $j_{photo-injection}(r) \propto |E_{normal}|^2$. The total injection current is obtained by integrating over the Schottky interface. In this simulation, optical parameters for Al-doped silver were taken from ellipsometry measurements.

The photo-injection current calculation is carried out by our collaborator Professor Alexander Govorov at Ohio University. In the theoretical treatment, photocurrent arises from the hot electrons that are generated near the metal-semiconductor interface by the plasmonic electric field that is normal to the interface[73], [74]. The total injected current from the unit cell is given by

$$I_{photo-injection} = C \cdot (\hbar\omega - \Delta\phi_{Barrier})^2 \cdot \int_{injecting\ surface\ only} |E_{normal}|^2 ds \quad \text{(B.1)}$$

where the integral is taken over the metal-Si interface within the unit cell, C is a material constant depending on the Fermi energy and the injecting barrier height, and $(\hbar\omega - \Delta\phi_{Barrier})^2$ is a factor reflecting the Fowler law. The barrier height was measured to be 0.54 eV and the constant C is treated as a wavelength independent fitting parameter that takes into account non-idealities in the barrier.

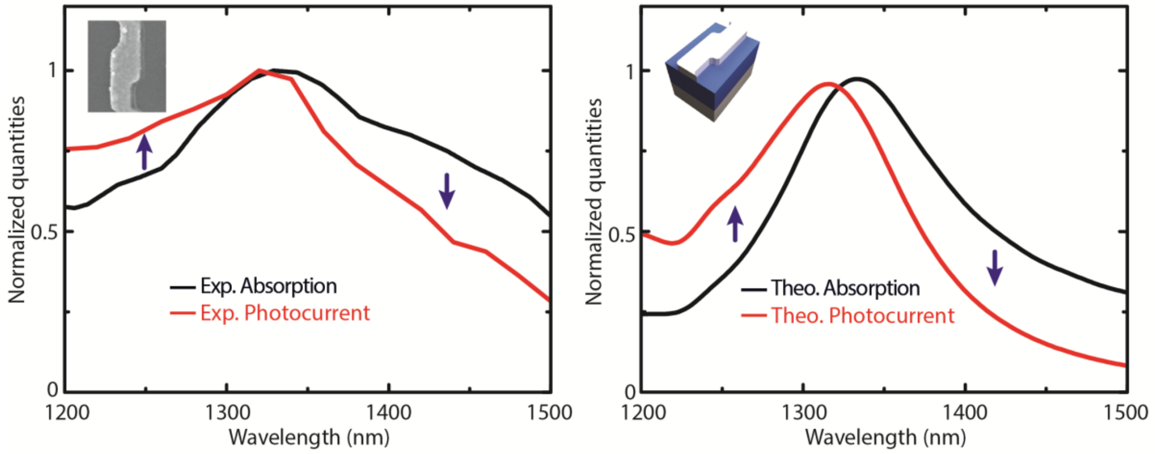

Figure B.5. Comparison of the absorption and photocurrent spectra. a, Normalized experimental measured absorption (black) and photocurrent (red) spectra for a RH metamaterial under RCP illumination. b, Normalized theoretical calculated absorption (black) and photocurrent (red) spectra for a RH metamaterial under RCP illumination.

As can be seen in Fig. B.5, we plot the normalized absorption and photocurrent spectra to compare their shapes. We see an interesting and strong effect of the asymmetry of the spectra. Both peaks in the absorption and photocurrent are somewhat asymmetric. The absorption peak exhibits relatively weak asymmetry and is slightly larger on the red side, whereas the photocurrent peak is clearly asymmetric and clearly smaller on the red side. Using our modeling, we can understand such asymmetries. The almost symmetric absorption peak comes from the strong plasmon resonance and was calculated from the Maxwell's equations incorporating the smooth Drude-like dielectric function of metal in this wavelength interval. The asymmetry of the photocurrent peak comes mostly from the involvement of the Fowler law in the equation for the photocurrent given in the Methods section. This equation for the photocurrent has the field factor and the Fowler-law factor, $(\hbar\omega - \Delta\phi_{Barrier})^2$, that is a strongly asymmetric function of the wavelength. The Fowler law takes into account the fact that some of the generated hot electrons do not have the proper momentum and energy to cross the interface into the silicon.

B.5 Linear relationship between photocurrent and incident laser power

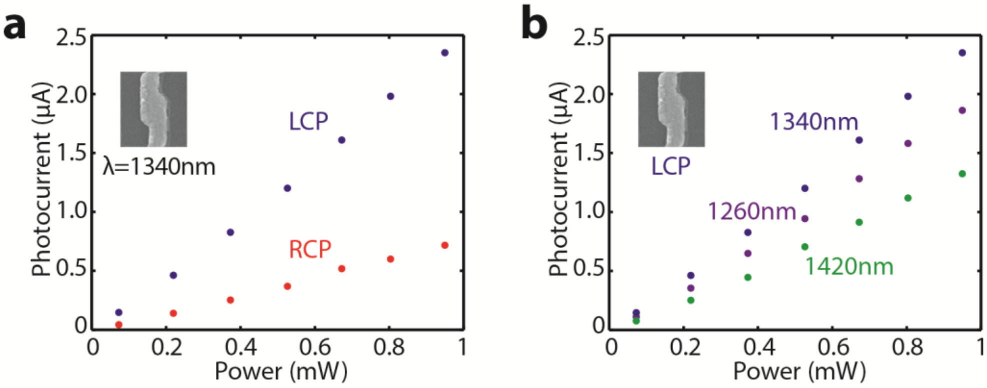

Figure B.6. Power dependent photocurrent for different polarization and wavelength. Unbiased photocurrent of the LH metamaterial was measured as a function of incident laser power for different polarization (a) and wavelength (b). Good linearity was observed in both cases, excluding any non-linear interactions. It also indicates the detector's ability to work over a wide range of incident power, overcoming saturation issues found in chiral organic semiconductors. The device area for this measurement is 70 μm x 70 μm.

B.6 Photoresponse under elliptical light illumination

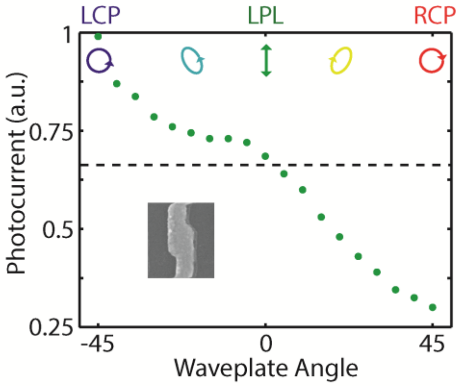

Figure B.7. Photocurrent response of the CPL detector under elliptical light.

BIBLIOGRAPHY

[1] W. Li and J. G. Valentine, "Harvesting the Loss: Surface Plasmon-Based Hot Electron Photodetection," *Nanophotonics*, 2016.

[2] W. Li, Z. J. Coppens, L. V. Besteiro, W. Wang, A. O. Govorov, and J. Valentine, "Circularly polarized light detection with hot electrons in chiral plasmonic metamaterials," *Nat. Commun.*, vol. 6, p. 8379, Sep. 2015.

[3] W. Li and J. Valentine, "Metamaterial Perfect Absorber Based Hot Electron Photodetection.," *Nano Lett.*, vol. 14, no. 6, pp. 3510–3514, May 2014.

[4] Z. J. Coppens, W. Li, D. G. Walker, and J. G. Valentine, "Probing and controlling photothermal heat generation in plasmonic nanostructures.," *Nano Lett.*, vol. 13, no. 3, pp. 1023–8, Mar. 2013.

[5] W. Li, Z. J. Coppens, D. Greg Walker, and J. G. Valentine, "Electron beam physical vapor deposition of thin ruby films for remote temperature sensing," *J. Appl. Phys.*, vol. 113, no. 16, p. 163509, Apr. 2013.

[6] I. Freestone, N. Meeks, M. Sax, and C. Higgitt, "The Lycurgus Cup — A Roman nanotechnology," *Gold Bull.*, vol. 40, no. 4, pp. 270–277, Dec. 2007.

[7] G. Mie, "Beitrzur Optik trMedien, speziell kolloidaler Metall"osungen," *Ann. Phys.*, vol. 330, no. 3, pp. 377–445, 1908.

[8] M. Faraday, "The Bakerian Lecture: Experimental Relations of Gold (and Other Metals) to Light," *Philos. Trans. R. Soc. London*, vol. 147, no. 0, pp. 145–181, 1857.

[9] J. C. Maxwell Garnett, "Colours in Metal Glasses, in Metallic Films, and in Metallic Solutions. II," *Philos. Trans. R. Soc. A Math. Phys. Eng. Sci.*, vol. 205, no. 387–401, pp. 237–288, 1906.

[10] R. Ritchie, "Plasma Losses by Fast Electrons in Thin Films," *Phys. Rev.*, vol. 106, no. 5, pp. 874–881, Jun. 1957.

[11] A. Otto, "Excitation of nonradiative surface plasma waves in silver by the method of frustrated total reflection," *Zeitschrift für Phys.*, vol. 216, no. 4, pp. 398–410, Aug. 1968.

[12] W. L. Barnes, A. Dereux, and T. W. Ebbesen, "Surface plasmon subwavelength optics.," *Nature*, vol. 424, no. 6950, pp. 824–30, Aug. 2003.

[13] J. A. Schuller, E. S. Barnard, W. Cai, Y. C. Jun, J. S. White, and M. L. Brongersma, “Plasmonics for extreme light concentration and manipulation.,” *Nat. Mater.*, vol. 9, no. 3, pp. 193–204, Mar. 2010.

[14] M. I. Stockman, “Nanoplasmonics: past, present, and glimpse into future.,” *Opt. Express*, vol. 19, no. 22, pp. 22029–106, Oct. 2011.

[15] D. K. Gramotnev and S. I. Bozhevolnyi, “Plasmonics beyond the diffraction limit,” *Nat. Photonics*, vol. 4, no. 2, pp. 83–91, Jan. 2010.

[16] J. A. Dionne, A. Baldi, B. Baum, C.-S. Ho, V. Janković, G. V. Naik, T. Narayan, J. A. Scholl, and Y. Zhao, “Localized fields, global impact: Industrial applications of resonant plasmonic materials,” *MRS Bull.*, vol. 40, no. 12, pp. 1138–1145, Nov. 2015.

[17] Z. Fang and X. Zhu, “Plasmonics in nanostructures.,” *Adv. Mater.*, vol. 25, no. 28, pp. 3840–56, Jul. 2013.

[18] J. Valentine, S. Zhang, T. Zentgraf, E. Ulin-Avila, D. A. Genov, G. Bartal, and X. Zhang, “Three-dimensional optical metamaterial with a negative refractive index.,” *Nature*, vol. 455, no. 7211, pp. 376–9, Sep. 2008.

[19] N. Yu, P. Genevet, M. A. Kats, F. Aieta, J.-P. Tetienne, F. Capasso, and Z. Gaburro, “Light propagation with phase discontinuities: generalized laws of reflection and refraction.,” *Science*, vol. 334, no. 6054, pp. 333–7, Oct. 2011.

[20] N. Fang, H. Lee, C. Sun, and X. Zhang, “Sub-diffraction-limited optical imaging with a silver superlens.,” *Science*, vol. 308, no. 5721, pp. 534–7, Apr. 2005.

[21] R. F. Oulton, V. J. Sorger, T. Zentgraf, R.-M. Ma, C. Gladden, L. Dai, G. Bartal, and X. Zhang, “Plasmon lasers at deep subwavelength scale.,” *Nature*, vol. 461, no. 7264, pp. 629–32, Oct. 2009.

[22] W. Cai, U. K. Chettiar, A. V. Kildishev, and V. M. Shalaev, “Optical cloaking with metamaterials,” *Nat. Photonics*, vol. 1, no. 4, pp. 224–227, Apr. 2007.

[23] H. A. Atwater and A. Polman, “Plasmonics for improved photovoltaic devices.,” *Nat. Mater.*, vol. 9, no. 3, pp. 205–13, Mar. 2010.

[24] S. V. Boriskina, H. Ghasemi, and G. Chen, “Plasmonic materials for energy: From physics to applications,” *Mater. Today*, vol. 16, no. 10, pp. 375–386, Oct. 2013.

[25] H. W. Lee, G. Papadakis, S. P. Burgos, K. Chander, A. Kriesch, R. Pala, U. Peschel, and H. A. Atwater, “Nanoscale conducting oxide PlasMOStor.,” *Nano Lett.*, vol. 14, no. 11, pp. 6463–8, Nov. 2014.

[26] N. Liu, T. Weiss, M. Mesch, L. Langguth, U. Eigenthaler, M. Hirscher, C. Sönnichsen, and H. Giessen, “Planar metamaterial analogue of electromagnetically induced transparency for plasmonic sensing.,” *Nano Lett.*, vol. 10, no. 4, pp. 1103–7, Apr. 2010.

[27] C. Wu, A. B. Khanikaev, R. Adato, N. Arju, A. A. Yanik, H. Altug, and G. Shvets, “Fano-resonant asymmetric metamaterials for ultrasensitive spectroscopy and identification of molecular monolayers.,” *Nat. Mater.*, vol. 11, no. 1, pp. 69–75, Jan. 2012.

[28] N. Yu and F. Capasso, “Flat optics with designer metasurfaces.,” *Nat. Mater.*, vol. 13, no. 2, pp. 139–50, Jan. 2014.

[29] A. G. Curto, G. Volpe, T. H. Taminiau, M. P. Kreuzer, R. Quidant, and N. F. van Hulst, “Unidirectional emission of a quantum dot coupled to a nanoantenna.,” *Science*, vol. 329, no. 5994, pp. 930–3, Aug. 2010.

[30] S. Kim, J. Jin, Y.-J. Kim, I.-Y. Park, Y. Kim, and S.-W. Kim, “High-harmonic generation by resonant plasmon field enhancement.,” *Nature*, vol. 453, no. 7196, pp. 757–60, Jun. 2008.

[31] J. Berthelot, S. S. Aćimović, M. L. Juan, M. P. Kreuzer, J. Renger, and R. Quidant, “Three-dimensional manipulation with scanning near-field optical nanotweezers.,” *Nat. Nanotechnol.*, vol. 9, no. 4, pp. 295–9, Apr. 2014.

[32] A. Melikyan, L. Alloatti, A. Muslija, D. Hillerkuss, P. C. Schindler, J. Li, R. Palmer, D. Korn, S. Muehlbrandt, D. Van Thourhout, B. Chen, R. Dinu, M. Sommer, C. Koos, M. Kohl, W. Freude, and J. Leuthold, “High-speed plasmonic phase modulators,” *Nat. Photonics*, vol. 8, no. 3, pp. 229–233, Feb. 2014.

[33] C. Sönnichsen, T. Franzl, T. Wilk, G. von Plessen, and J. Feldmann, “Drastic Reduction of Plasmon Damping in Gold Nanorods,” *Phys. Rev. Lett.*, vol. 88, no. 7, p. 077402, Jan. 2002.

[34] J. Endriz and W. Spicer, “Surface-Plasmon-One-Electron Decay and its Observation in Photoemission,” *Phys. Rev. Lett.*, vol. 24, no. 2, pp. 64–68, Jan. 1970.

[35] R. Fuchs and K. Kliewer, “Surface Plasmon in a Semi-Infinite Free-Electron Gas,” *Phys. Rev. B*, vol. 3, no. 7, pp. 2270–2278, Apr. 1971.

[36] T. Inagaki, K. Kagami, and E. Arakawa, “Photoacoustic observation of nonradiative decay of surface plasmons in silver,” *Phys. Rev. B*, vol. 24, no. 6, pp. 3644–3646, Sep. 1981.

[37] C. Clavero, “Plasmon-induced hot-electron generation at nanoparticle/metal-oxide

interfaces for photovoltaic and photocatalytic devices," *Nat. Photonics*, vol. 8, no. 2, pp. 95–103, Jan. 2014.

[38] M. L. Brongersma, N. J. Halas, and P. Nordlander, "Plasmon-induced hot carrier science and technology," *Nat. Nanotechnol.*, vol. 10, no. 1, pp. 25–34, Jan. 2015.

[39] G. Baffou and R. Quidant, "Thermo-plasmonics: using metallic nanostructures as nano-sources of heat," *Laser Photon. Rev.*, p. n/a–n/a, Apr. 2012.

[40] S. Linic, P. Christopher, and D. B. Ingram, "Plasmonic-metal nanostructures for efficient conversion of solar to chemical energy.," *Nat. Mater.*, vol. 10, no. 12, pp. 911–21, Dec. 2011.

[41] S. Mukherjee, F. Libisch, N. Large, O. Neumann, L. V Brown, J. Cheng, J. B. Lassiter, E. A. Carter, P. Nordlander, and N. J. Halas, "Hot electrons do the impossible: plasmon-induced dissociation of H2 on Au.," *Nano Lett.*, vol. 13, no. 1, pp. 240–7, Jan. 2013.

[42] S. Mubeen, J. Lee, N. Singh, S. Krämer, G. D. Stucky, and M. Moskovits, "An autonomous photosynthetic device in which all charge carriers derive from surface plasmons.," *Nat. Nanotechnol.*, vol. 8, no. 4, pp. 247–51, Apr. 2013.

[43] K. Appavoo, B. Wang, N. F. Brady, M. Seo, J. Nag, R. P. Prasankumar, D. J. Hilton, S. T. Pantelides, and R. F. Haglund, "Ultrafast phase transition via catastrophic phonon collapse driven by plasmonic hot-electron injection.," *Nano Lett.*, vol. 14, no. 3, pp. 1127–33, Mar. 2014.

[44] Y. Kang, S. Najmaei, Z. Liu, Y. Bao, Y. Wang, X. Zhu, N. J. Halas, P. Nordlander, P. M. Ajayan, J. Lou, and Z. Fang, "Plasmonic hot electron induced structural phase transition in a MoS2 monolayer.," *Adv. Mater.*, vol. 26, no. 37, pp. 6467–71, Oct. 2014.

[45] G. V. Naik and J. A. Dionne, "Photon upconversion with hot carriers in plasmonic systems," *Appl. Phys. Lett.*, vol. 107, no. 13, p. 133902, Sep. 2015.

[46] M. W. Knight, H. Sobhani, P. Nordlander, and N. J. Halas, "Photodetection with active optical antennas.," *Science*, vol. 332, no. 6030, pp. 702–704, May 2011.

[47] I. Goykhman, B. Desiatov, J. Khurgin, J. Shappir, and U. Levy, "Locally oxidized silicon surface-plasmon Schottky detector for telecom regime.," *Nano Lett.*, vol. 11, no. 6, pp. 2219–24, Jun. 2011.

[48] A. Sobhani, M. W. Knight, Y. Wang, B. Zheng, N. S. King, L. V Brown, Z. Fang, P. Nordlander, and N. J. Halas, "Narrowband photodetection in the near-infrared with a plasmon-induced hot electron device.," *Nat. Commun.*, vol. 4, p. 1643, Jan. 2013.

[49] F. Wang and N. A. Melosh, “Power-independent wavelength determination by hot carrier collection in metal-insulator-metal devices.,” *Nat. Commun.*, vol. 4, p. 1711, Jan. 2013.

[50] J.-H. Kim and J.-S. Yeo, “Enhanced detection of broadband incoherent light with nanoridge plasmonics.,” *Nano Lett.*, vol. 15, no. 4, pp. 2291–7, Apr. 2015.

[51] C. Loo, A. Lowery, N. Halas, J. West, and R. Drezek, “Immunotargeted nanoshells for integrated cancer imaging and therapy.,” *Nano Lett.*, vol. 5, no. 4, pp. 709–711, Apr. 2005.

[52] E. C. Garnett, W. Cai, J. J. Cha, F. Mahmood, S. T. Connor, M. Greyson Christoforo, Y. Cui, M. D. McGehee, and M. L. Brongersma, “Self-limited plasmonic welding of silver nanowire junctions.,” *Nat. Mater.*, vol. 11, no. 3, pp. 241–9, 2012.

[53] O. Neumann, C. Feronti, A. D. Neumann, A. Dong, K. Schell, B. Lu, E. Kim, M. Quinn, S. Thompson, N. Grady, P. Nordlander, M. Oden, and N. J. Halas, “Compact solar autoclave based on steam generation using broadband light-harvesting nanoparticles.,” *Proc. Natl. Acad. Sci. U. S. A.*, vol. 110, no. 29, pp. 11677–81, Jul. 2013.

[54] Z. Fang, Y.-R. Zhen, O. Neumann, A. Polman, F. J. García de Abajo, P. Nordlander, and N. J. Halas, “Evolution of light-induced vapor generation at a liquid-immersed metallic nanoparticle.,” *Nano Lett.*, vol. 13, no. 4, pp. 1736–42, Apr. 2013.

[55] W. A. Challener, C. Peng, A. V. Itagi, D. Karns, W. Peng, Y. Peng, X. Yang, X. Zhu, N. J. Gokemeijer, Y.-T. Hsia, G. Ju, R. E. Rottmayer, M. A. Seigler, and E. C. Gage, “Heat-assisted magnetic recording by a near-field transducer with efficient optical energy transfer,” *Nat. Photonics*, vol. 3, no. 4, pp. 220–224, Mar. 2009.

[56] B. C. Stipe, T. C. Strand, C. C. Poon, H. Balamane, T. D. Boone, J. A. Katine, J.-L. Li, V. Rawat, H. Nemoto, A. Hirotsune, O. Hellwig, R. Ruiz, E. Dobisz, D. S. Kercher, N. Robertson, T. R. Albrecht, and B. D. Terris, “Magnetic recording at 1.5 Pb m−2 using an integrated plasmonic antenna,” *Nat. Photonics*, vol. 4, no. 7, pp. 484–488, May 2010.

[57] R. H. Fowler, “The Analysis of Photoelectric Sensitivity Curves for Clean Metals at Various Temperatures,” *Phys. Rev.*, vol. 38, no. 1, pp. 45–56, Jul. 1931.

[58] W. Spicer, “Photoemissive, Photoconductive, and Optical Absorption Studies of Alkali-Antimony Compounds,” *Phys. Rev.*, vol. 112, no. 1, pp. 114–122, Oct. 1958.

[59] W. E. Spicer, “Negative affinity 3–5 photocathodes: Their physics and technology,” *Appl. Phys.*, vol. 12, no. 2, pp. 115–130, Feb. 1977.

[60] S. M. Sze and K. K. Ng, “Physics of Semiconductor Devices, 3rd Edition - Simon M. Sze, Kwok K. Ng,” in *Physics of Semiconductor Devices, 3rd Edition.; John Wiley & Sons, Inc.; NJ*, 2007, pp. 164, 682.

[61] C. Henkel, S. Abermann, O. Bethge, G. Pozzovivo, S. Puchner, H. Hutter, and E. Bertagnolli, “Reduction of the PtGe/Ge Electron Schottky-Barrier Height by Rapid Thermal Diffusion of Phosphorous Dopants,” *J. Electrochem. Soc.*, vol. 157, no. 8, p. H815, Aug. 2010.

[62] R. R. Lieten, V. V. Afanas’ev, N. H. Thoan, S. Degroote, W. Walukiewicz, and G. Borghs, “Mechanisms of Schottky Barrier Control on n-Type Germanium Using Ge_3N_4 Interlayers,” *J. Electrochem. Soc.*, vol. 158, no. 4, p. H358, Apr. 2011.

[63] X. Wang, C. Liow, D. Qi, B. Zhu, W. R. Leow, H. Wang, C. Xue, X. Chen, and S. Li, “Programmable photo-electrochemical hydrogen evolution based on multi-segmented CdS-Au nanorod arrays.,” *Adv. Mater.*, vol. 26, no. 21, pp. 3506–12, Jun. 2014.

[64] Hailin Xue, W. Chen, Caixia Liu, X. Kong, Pengfei Qu, Ziran Liu, Jingran Zhou, L. Shen, Zhicheng Zhong, and S. Ruan, “Fabrication of TiO_2 Schottky barrier diodes by RF magnetron sputtering,” in *2008 3rd IEEE International Conference on Nano/Micro Engineered and Molecular Systems*, 2008, pp. 108–111.

[65] J.-J. Huang, C.-W. Kuo, W.-C. Chang, and T.-H. Hou, “Transition of stable rectification to resistive-switching in Ti/TiO_2/Pt oxide diode,” *Appl. Phys. Lett.*, vol. 96, no. 26, p. 262901, Jun. 2010.

[66] D. L. Carroll, M. Wagner, M. Rühle, and D. A. Bonnell, “Schottky-barrier formation at nanoscale metal-oxide interfaces,” *Phys. Rev. B*, vol. 55, no. 15, pp. 9792–9799, Apr. 1997.

[67] H. Lee, Y. K. Lee, E. Hwang, and J. Y. Park, “Enhanced Surface Plasmon Effect of Ag/TiO_2 Nanodiodes on Internal Photoemission,” *J. Phys. Chem. C*, vol. 118, no. 11, pp. 5650–5656, Mar. 2014.

[68] Y. K. Lee, C. H. Jung, J. Park, H. Seo, G. A. Somorjai, and J. Y. Park, “Surface plasmon-driven hot electron flow probed with metal-semiconductor nanodiodes.,” *Nano Lett.*, vol. 11, no. 10, pp. 4251–5, Oct. 2011.

[69] T. P. White and K. R. Catchpole, “Plasmon-enhanced internal photoemission for photovoltaics: Theoretical efficiency limits,” *Appl. Phys. Lett.*, vol. 101, no. 7, p. 073905, Aug. 2012.

[70] C. F. Bohren, “How can a particle absorb more than the light incident on it?,” *Am. J. Phys.*, vol. 51, no. 4, p. 323, Apr. 1983.

[71] B. Y. Zheng, H. Zhao, A. Manjavacas, M. McClain, P. Nordlander, and N. J. Halas, "Distinguishing between plasmon-induced and photoexcited carriers in a device geometry," *Nat. Commun.*, vol. 6, p. 7797, Jul. 2015.

[72] A. Manjavacas, J. G. Liu, V. Kulkarni, and P. Nordlander, "Plasmon-induced hot carriers in metallic nanoparticles.," *ACS Nano*, vol. 8, no. 8, pp. 7630–8, Aug. 2014.

[73] A. O. Govorov, H. Zhang, and Y. K. Gun'ko, "Theory of photoinjection of hot plasmonic carriers from metal nanostructures into semiconductors and surface molecules," *J. Phys. Chem. C*, vol. 117, no. 32, pp. 16616–16631, Aug. 2013.

[74] A. O. Govorov and H. Zhang, "Kinetic Density Functional Theory for Plasmonic Nanostructures: Breaking of the Plasmon Peak in the Quantum Regime and Generation of Hot Electrons," *J. Phys. Chem. C*, vol. 119, no. 11, pp. 6181–6194, Mar. 2015.

[75] X. Li, D. Xiao, and Z. Zhang, "Landau damping of quantum plasmons in metal nanostructures," *New J. Phys.*, vol. 15, no. 2, p. 023011, Feb. 2013.

[76] H. Zhang and A. O. Govorov, "Optical Generation of Hot Plasmonic Carriers in Metal Nanocrystals: The Effects of Shape and Field Enhancement," *J. Phys. Chem. C*, vol. 118, no. 14, pp. 7606–7614, Apr. 2014.

[77] T. Gong and J. N. Munday, "Materials for hot carrier plasmonics," *Opt. Mater. Express*, vol. 5, no. 11, p. 2501, Oct. 2015.

[78] C. S. Kumarasinghe, M. Premaratne, Q. Bao, and G. P. Agrawal, "Theoretical analysis of hot electron dynamics in nanorods.," *Sci. Rep.*, vol. 5, p. 12140, Jan. 2015.

[79] R. Sundararaman, P. Narang, A. S. Jermyn, W. A. Goddard III, and H. A. Atwater, "Theoretical predictions for hot-carrier generation from surface plasmon decay," *Nat. Commun.*, vol. 5, p. 5788, Dec. 2014.

[80] M. Bernardi, J. Mustafa, J. B. Neaton, and S. G. Louie, "Theory and computation of hot carriers generated by surface plasmon polaritons in noble metals," *Nat. Commun.*, vol. 6, p. 7044, Jun. 2015.

[81] S. V. Boriskina, J. Zhou, W.-C. Hsu, B. Liao, and G. Chen, "Limiting efficiencies of solar energy conversion and photo-detection via internal emission of hot electrons and hot holes in gold," in *SPIE Optical Engineering + Applications*, 2015, p. 960816.

[82] A. M. Brown, R. Sundararaman, P. Narang, W. A. Goddard Iii, and H. A. Atwater, "Non-Radiative Plasmon Decay and Hot Carrier Dynamics: Effects of Phonons,

Surfaces and Geometry.," *ACS Nano*, Dec. 2015.

[83] A. O. Govorov and H. H. Richardson, "Generating heat with metal nanoparticles," *Nano Today*, vol. 2, no. 1, pp. 30–38, Feb. 2007.

[84] G. Baffou, R. Quidant, and C. Girard, "Heat generation in plasmonic nanostructures: Influence of morphology," *Appl. Phys. Lett.*, vol. 94, no. 15, p. 153109, Apr. 2009.

[85] G. Baffou, C. Girard, and R. Quidant, "Mapping Heat Origin in Plasmonic Structures," *Phys. Rev. Lett.*, vol. 104, no. 13, p. 136805, Apr. 2010.

[86] G. Baffou, R. Quidant, and F. J. G. de Abajo, "Nanoscale Control of Optical Heating in Complex Plasmonic Systems," *ACS Nano*, vol. 4, pp. 709–716, Jan. 2010.

[87] J. R. Adleman, D. A. Boyd, D. G. Goodwin, and D. Psaltis, "Heterogenous Catalysis Mediated by Plasmon Heating," *Nano Lett.*, vol. 9, pp. 4417–4423, Dec. 2009.

[88] L. Cao, D. N. Barsic, A. R. Guichard, and M. L. Brongersma, "Plasmon-assisted local temperature control to pattern individual semiconductor nanowires and carbon nanotubes.," *Nano Lett.*, vol. 7, no. 11, pp. 3523–7, Nov. 2007.

[89] P. Christopher, H. Xin, and S. Linic, "Visible-light-enhanced catalytic oxidation reactions on plasmonic silver nanostructures.," *Nat. Chem.*, vol. 3, no. 6, pp. 467–472, Jun. 2011.

[90] L. Wang and B. Li, "Thermal Memory: A Storage of Phononic Information," *Phys. Rev. Lett.*, vol. 101, no. 26, p. 267203, Dec. 2008.

[91] R. Huschka, J. Zuloaga, M. W. Knight, L. V Brown, P. Nordlander, and N. J. Halas, "Light-induced release of DNA from gold nanoparticles: nanoshells and nanorods.," *J. Am. Chem. Soc.*, vol. 133, no. 31, pp. 12247–12255, Aug. 2011.

[92] P. K. Jain, I. H. El-Sayed, and M. A. El-Sayed, "Au nanoparticles target cancer," *Nano Today*, vol. 2, no. 1, pp. 18–29, Feb. 2007.

[93] A. O. Govorov, W. Zhang, T. Skeini, H. Richardson, J. Lee, and N. A. Kotov, "Gold nanoparticle ensembles as heaters and actuators: melting and collective plasmon resonances," *Nanoscale Res. Lett.*, vol. 1, no. 1, pp. 84–90, Jul. 2006.

[94] A. Majumdar, "Scanning Thermal Microscopy," *Annu. Rev.*, vol. 29, pp. 505–585, 1999.

[95] G. Baffou, P. Bon, J. Savatier, J. Polleux, M. Zhu, M. Merlin, H. Rigneault, and S.

Monneret, “Thermal imaging of nanostructures by quantitative optical phase analysis.,” *ACS Nano*, vol. 6, no. 3, pp. 2452–2458, Mar. 2012.

[96] G. Abstreiter, “Micro-Raman spectroscopy for characterization of semiconductor devices,” *Appl. Surf. Sci.*, vol. 50, no. 1–4, pp. 73–78, Jun. 1991.

[97] M. T. Carlson, A. Khan, and H. H. Richardson, “Local temperature determination of optically excited nanoparticles and nanodots.,” *Nano Lett.*, vol. 11, no. 3, pp. 1061–1069, Mar. 2011.

[98] G. Baffou, M. P. Kreuzer, F. Kulzer, and R. Quidant, “Temperature mapping near plasmonic nanostructures using fluorescence polarization anisotropy,” *Opt. Express*, vol. 17, no. 5, pp. 3291–3298, Feb. 2009.

[99] N. Zhou, E. C. Kinzel, and X. Xu, “Complementary bowtie aperture for localizing and enhancing optical magnetic field,” *Opt. Lett.*, vol. 36, no. 15, p. 2764, Jul. 2011.

[100] T. Grosjean, M. Mivelle, F. I. Baida, G. W. Burr, and U. C. Fischer, “Diabolo nanoantenna for enhancing and confining the magnetic optical field.,” *Nano Lett.*, vol. 11, no. 3, pp. 1009–1013, Mar. 2011.

[101] S. W. Allison and G. T. Gillies, “Remote thermometry with thermographic phosphors: Instrumentation and applications,” *Rev. Sci. Instrum.*, vol. 68, no. 7, p. 2615, Jul. 1997.

[102] C. Pflitsch, D. Viefhaus, and B. Atakan, “CVD of Thin Ruby Films on Si(100) and Stainless Steel for Surface Temperature Sensor Applications,” *Chem. Vap. Depos.*, vol. 13, no. 8, pp. 420–426, Aug. 2007.

[103] B. Atakan, C. Eckert, and C. Pflitsch, “Light emitting diode excitation of Cr^{3+} :Al_2O_3 as thermographic phosphor: experiments and measurement strategy,” *Meas. Sci. Technol.*, vol. 20, no. 7, p. 075304, Jul. 2009.

[104] H. C. Seat and J. H. Sharp, “Dedicated Temperature Sensing With C-Axis Oriented Single-Crystal Ruby (Cr^{3+}:Al_2O_3) Fibers: Temperature and Strain Dependences of R-Line Fluorescence,” *IEEE Trans. Instrum. Meas.*, vol. 53, no. 1, pp. 140–154, Feb. 2004.

[105] H. Aizawa, N. Ohishi, S. Ogawa, T. Katsumata, S. Komuro, T. Morikawa, and E. Toba, “Fabrication of ruby sensor probe for the fiber-optic thermometer using fluorescence decay,” *Rev. Sci. Instrum.*, vol. 73, no. 10, pp. 3656–3658, Oct. 2002.

[106] Z. Ghassemlooy, K. T. V. Grattan, and D. Lynch, “Probe design aspects of ruby decay-time fluorescent sensors,” *Rev. Sci. Instrum.*, vol. 60, no. 1, pp. 87–89, Jan. 1989.

[107] Z. Zhang, K. Grattan, and A. Palmer, “Temperature dependences of fluorescence lifetimes in Cr^{3+}-doped insulating crystals,” *Phys. Rev. B*, vol. 48, no. 11, pp. 7772–7778, Sep. 1993.

[108] R. C. R. C. Powell, *Physics of Solid State Laser Materials*. New York: Springer-Verlag, 1998.

[109] D. D. Ragan, R. Gustavsen, and D. Schiferl, “Calibration of the ruby R1 and R2 fluorescence shifts as a function of temperature from 0 to 600 K,” *J. Appl. Phys.*, vol. 72, no. 12, pp. 5539–5544, Dec. 1992.

[110] J. J. Kingsley, N. Manickam, and K. C. Patil, “Combustion synthesis and properties of fine particle fluorescent aluminous oxides,” *Bull. Mater. Sci.*, vol. 13, no. 3, pp. 179–189, Jun. 1990.

[111] C. Pflitsch, R. A. Siddiqui, and B. Atakan, “Phosphorescence properties of sol–gel derived ruby measured as functions of temperature and Cr^{3+} content,” *Appl. Phys. A*, vol. 90, no. 3, pp. 527–532, Nov. 2007.

[112] I. Petrov, P. B. Barna, L. Hultman, and J. E. Greene, “Microstructural evolution during film growth,” *J. Vac. Sci. Technol. A Vacuum, Surfaces, Film.*, vol. 21, no. 5, pp. S117–S128, Sep. 2003.

[113] Q. Y. Zhang, W. J. Zhao, P. S. Wang, L. Wang, J. J. Xu, and P. K. Chu, “Microstructure, morphology and their annealing behaviors of alumina films synthesized by ion beam assisted deposition,” *Nucl. Instruments Methods Phys. Res. Sect. B Beam Interact. with Mater. Atoms*, vol. 206, pp. 357–361, May 2003.

[114] C. Pflitsch, R. A. Siddiqui, C. Eckert, and B. Atakan, “Sol–Gel Deposition of Chromium Doped Aluminium Oxide Films (Ruby) for Surface Temperature Sensor Application,” *Chem. Mater.*, vol. 20, no. 8, pp. 2773–2778, Apr. 2008.

[115] S. ITO, N. Umehara, H. Takata, and T. Fujii, “Phase transition of γ-Al_2O_3 under hot isostatic pressure,” *Solid State Ionics*, vol. 172, no. 1–4, pp. 403–406, Aug. 2004.

[116] K. Shimizu, W. Woo, B. Fisher, H. Eisler, and M. Bawendi, “Surface-Enhanced Emission from Single Semiconductor Nanocrystals,” *Phys. Rev. Lett.*, vol. 89, no. 11, p. 117401, Aug. 2002.

[117] P. Anger, P. Bharadwaj, and L. Novotny, “Enhancement and Quenching of Single-Molecule Fluorescence,” *Phys. Rev. Lett.*, vol. 96, no. 11, p. 113002, Mar. 2006.

[118] J. N. Farahani, D. W. Pohl, H.-J. Eisler, and B. Hecht, “Single Quantum Dot Coupled to a Scanning Optical Antenna: A Tunable Superemitter,” *Phys. Rev. Lett.*, vol. 95, no. 1, p. 17402, Jun. 2005.

[119] F. P. Incropera and D. P. DeWitt, *Introduction To Heat Transfer*, 5th ed. Hoboken: Wiley, 2007.

[120] Z. Liu, J. M. Steele, W. Srituravanich, Y. Pikus, C. Sun, and X. Zhang, "Focusing surface plasmons with a plasmonic lens.," *Nano Lett.*, vol. 5, no. 9, pp. 1726–1729, Sep. 2005.

[121] G. Baffou, R. Quidant, and C. Girard, "Thermoplasmonics modeling: A Green's function approach," *Phys. Rev. B*, vol. 82, no. 16, p. 165424, Oct. 2010.

[122] K. Ueno and H. Misawa, "Plasmon-enhanced photocurrent generation and water oxidation from visible to near-infrared wavelengths," *NPG Asia Mater.*, vol. 5, no. 9, p. e61, Sep. 2013.

[123] M. W. Knight, Y. Wang, A. S. Urban, A. Sobhani, B. Y. Zheng, P. Nordlander, and N. J. Halas, "Embedding plasmonic nanostructure diodes enhances hot electron emission.," *Nano Lett.*, vol. 13, no. 4, pp. 1687–1692, Apr. 2013.

[124] H. Chalabi, D. Schoen, and M. L. Brongersma, "Hot-electron photodetection with a plasmonic nanostripe antenna.," *Nano Lett.*, vol. 14, no. 3, pp. 1374–1380, Feb. 2014.

[125] K.-T. Lin, H.-L. Chen, Y.-S. Lai, and C.-C. Yu, "Silicon-based broadband antenna for high responsivity and polarization-insensitive photodetection at telecommunication wavelengths," *Nat. Commun.*, vol. 5, p. 3288, Feb. 2014.

[126] I. Goykhman, B. Desiatov, J. Khurgin, J. Shappir, and U. Levy, "Waveguide based compact silicon Schottky photodetector with enhanced responsivity in the telecom spectral band.," *Opt. Express*, vol. 20, no. 27, pp. 28594–28602, Dec. 2012.

[127] M. Casalino, M. Iodice, L. Sirleto, I. Rendina, and G. Coppola, "Asymmetric MSM sub-bandgap all-silicon photodetector with low dark current," *Opt. Express*, vol. 21, no. 23, p. 28072, Nov. 2013.

[128] S. M. Sze, J. L. Moll, and T. Sugano, "Range-energy relation of hot electrons in gold," *Solid. State. Electron.*, vol. 7, no. 7, pp. 509–523, Jul. 1964.

[129] X. Liu, T. Starr, A. F. Starr, and W. J. Padilla, "Infrared Spatial and Frequency Selective Metamaterial with Near-Unity Absorbance," *Phys. Rev. Lett.*, vol. 104, no. 20, p. 207403, May 2010.

[130] N. Liu, M. Mesch, T. Weiss, M. Hentschel, and H. Giessen, "Infrared perfect absorber and its application as plasmonic sensor.," *Nano Lett.*, vol. 10, no. 7, pp. 2342–8, Jul. 2010.

[131] X. Liu, T. Tyler, T. Starr, A. F. Starr, N. M. Jokerst, and W. J. Padilla, "Taming

the Blackbody with Infrared Metamaterials as Selective Thermal Emitters," *Phys. Rev. Lett.*, vol. 107, no. 4, p. 045901, Jul. 2011.

[132] Y. Shen, J. Zhou, T. Liu, Y. Tao, R. Jiang, M. Liu, G. Xiao, J. Zhu, Z.-K. Zhou, X. Wang, C. Jin, and J. Wang, "Plasmonic gold mushroom arrays with refractive index sensing figures of merit approaching the theoretical limit.," *Nat. Commun.*, vol. 4, p. 2381, Jan. 2013.

[133] S. Mukherjee, L. Zhou, A. M. Goodman, N. Large, C. Ayala-Orozco, Y. Zhang, P. Nordlander, and N. J. Halas, "Hot-Electron-Induced Dissociation of H_2 on Gold Nanoparticles Supported on SiO_2.," *J. Am. Chem. Soc.*, vol. 136, no. 1, pp. 64–7, Jan. 2014.

[134] S. Cattarin, P. Guerriero, N. Dietz, and H. J. Lewerenz, "Electrodissolution and corrosion of $CuInS_2$ photoanodes with lamellar morphology," *Electrochim. Acta*, vol. 40, no. 8, pp. 1041–1049, Jun. 1995.

[135] J. C. Hulteen, "Nanosphere lithography: A materials general fabrication process for periodic particle array surfaces," *J. Vac. Sci. Technol. A Vacuum, Surfaces, Film.*, vol. 13, no. 3, p. 1553, May 1995.

[136] J. Rybczynski, U. Ebels, and M. Giersig, "Large-scale, 2D arrays of magnetic nanoparticles," *Colloids Surfaces A Physicochem. Eng. Asp.*, vol. 219, no. 1–3, pp. 1–6, Jun. 2003.

[137] C.-C. Ho, P.-Y. Chen, K.-H. Lin, W.-T. Juan, and W.-L. Lee, "Fabrication of monolayer of polymer/nanospheres hybrid at a water-air interface.," *ACS Appl. Mater. Interfaces*, vol. 3, no. 2, pp. 204–8, Feb. 2011.

[138] J.-T. Zhang, L. Wang, D. N. Lamont, S. S. Velankar, and S. A. Asher, "Fabrication of large-area two-dimensional colloidal crystals.," *Angew. Chem. Int. Ed. Engl.*, vol. 51, no. 25, pp. 6117–20, Jun. 2012.

[139] J.-T. Zhang, L. Wang, X. Chao, S. S. Velankar, and S. A. Asher, "Vertical spreading of two-dimensional crystalline colloidal arrays," *J. Mater. Chem. C*, vol. 1, no. 38, p. 6099, Sep. 2013.

[140] J. F. Sherson, H. Krauter, R. K. Olsson, B. Julsgaard, K. Hammerer, I. Cirac, and E. S. Polzik, "Quantum teleportation between light and matter.," *Nature*, vol. 443, no. 7111, pp. 557–560, Oct. 2006.

[141] C. Wagenknecht, C.-M. Li, A. Reingruber, X.-H. Bao, A. Goebel, Y.-A. Chen, Q. Zhang, K. Chen, and J.-W. Pan, "Experimental demonstration of a heralded entanglement source," *Nat. Photonics*, vol. 4, no. 8, pp. 549–552, May 2010.

[142] E. Togan, Y. Chu, A. S. Trifonov, L. Jiang, J. Maze, L. Childress, M. V. G. Dutt,

A. S. Sørensen, P. R. Hemmer, A. S. Zibrov, and M. D. Lukin, “Quantum entanglement between an optical photon and a solid-state spin qubit.,” *Nature*, vol. 466, no. 7307, pp. 730–4, Aug. 2010.

[143] R. Farshchi, M. Ramsteiner, J. Herfort, A. Tahraoui, and H. T. Grahn, “Optical communication of spin information between light emitting diodes,” *Appl. Phys. Lett.*, vol. 98, no. 16, p. 162508, Apr. 2011.

[144] N. J. Greenfield, “Using circular dichroism spectra to estimate protein secondary structure.,” *Nat. Protoc.*, vol. 1, no. 6, pp. 2876–2890, Jan. 2006.

[145] C. D. Stanciu, F. Hansteen, A. Kimel, A. Kirilyuk, A. Tsukamoto, A. Itoh, and T. Rasing, “All-optical magnetic recording with circularly polarized light,” *Phys. Rev. Lett.*, vol. 99, no. 4, p. 047601, Jul. 2007.

[146] R. P. Feynman, R. B. Leighton, and M. Sands, *The Feynman Lectures on Physics (Addison Wsley Longman, 1970)*. 1970.

[147] T.-H. Chiou, S. Kleinlogel, T. Cronin, R. Caldwell, B. Loeffler, A. Siddiqi, A. Goldizen, and J. Marshall, “Circular polarization vision in a stomatopod crustacean.,” *Curr. Biol.*, vol. 18, no. 6, pp. 429–434, Mar. 2008.

[148] Y. J. Zhang, T. Oka, R. Suzuki, J. T. Ye, and Y. Iwasa, “Electrically switchable chiral light-emitting transistor.,” *Science*, vol. 344, no. 6185, pp. 725–728, May 2014.

[149] S. Zhang, H. Wei, K. Bao, U. Håkanson, N. J. Halas, P. Nordlander, and H. Xu, “Chiral surface plasmon polaritons on metallic nanowires,” *Phys. Rev. Lett.*, vol. 107, no. 9, p. 096801, Aug. 2011.

[150] N. Yu, F. Aieta, P. Genevet, M. A. Kats, Z. Gaburro, and F. Capasso, “A broadband, background-free quarter-wave plate based on plasmonic metasurfaces.,” *Nano Lett.*, vol. 12, no. 12, pp. 6328–6333, Dec. 2012.

[151] J. K. Gansel, M. Thiel, M. S. Rill, M. Decker, K. Bade, V. Saile, G. von Freymann, S. Linden, and M. Wegener, “Gold helix photonic metamaterial as broadband circular polarizer.,” *Science*, vol. 325, no. 5947, pp. 1513–1515, Sep. 2009.

[152] M. D. Turner, M. Saba, Q. Zhang, B. P. Cumming, G. E. Schröder-Turk, and M. Gu, “Miniature chiral beamsplitter based on gyroid photonic crystals,” *Nat. Photonics*, vol. 7, no. 10, pp. 801–805, Sep. 2013.

[153] F. J. Rodríguez-Fortuño, I. Barber-Sanz, D. Puerto, A. Griol, and A. Martínez, “Resolving light handedness with an on-chip silicon microdisk,” *ACS Photonics*, vol. 1, no. 9, pp. 762–767, Sep. 2014.

[154] V. Sharma, M. Crne, J. O. Park, and M. Srinivasarao, “Structural origin of circularly polarized iridescence in jeweled beetles.,” *Science*, vol. 325, no. 5939, pp. 449–451, Jul. 2009.

[155] Y. Yang, R. C. da Costa, M. J. Fuchter, and A. J. Campbell, “Circularly polarized light detection by a chiral organic semiconductor transistor,” *Nat. Photonics*, vol. 7, no. 8, pp. 634–638, Jul. 2013.

[156] V. K. Valev, J. J. Baumberg, C. Sibilia, and T. Verbiest, “Chirality and chiroptical effects in plasmonic nanostructures: fundamentals, recent progress, and outlook.,” *Adv. Mater.*, vol. 25, no. 18, pp. 2517–34, May 2013.

[157] A. Ben-Moshe, B. M. Maoz, A. O. Govorov, and G. Markovich, “Chirality and chiroptical effects in inorganic nanocrystal systems with plasmon and exciton resonances,” *Chem. Soc. Rev.*, vol. 42, no. 16, p. 7028, Jul. 2013.

[158] F. Afshinmanesh, J. S. White, W. Cai, and M. L. Brongersma, “Measurement of the polarization state of light using an integrated plasmonic polarimeter,” *Nanophotonics*, vol. 1, no. 2, pp. 125–129, Jan. 2012.

[159] J. I. Ziegler and R. F. Haglund, “Plasmonic response of nanoscale spirals.,” *Nano Lett.*, vol. 10, no. 8, pp. 3013–8, Aug. 2010.

[160] V. A. Fedotov, A. S. Schwanecke, N. I. Zheludev, V. V. Khardikov, and S. L. Prosvirnin, “Asymmetric transmission of light and enantiomerically sensitive plasmon resonance in planar chiral nanostructures,” *Nano Lett.*, vol. 7, no. 7, pp. 1996–1999, Jul. 2007.

[161] A. Kuzyk, R. Schreiber, Z. Fan, G. Pardatscher, E.-M. Roller, A. Högele, F. C. Simmel, A. O. Govorov, and T. Liedl, “DNA-based self-assembly of chiral plasmonic nanostructures with tailored optical response.,” *Nature*, vol. 483, no. 7389, pp. 311–314, Mar. 2012.

[162] M. Schäferling, X. Yin, N. Engheta, and H. Giessen, “Helical Plasmonic Nanostructures as Prototypical Chiral Near-Field Sources,” *ACS Photonics*, vol. 1, no. 6, pp. 530–537, Jun. 2014.

[163] B. Hopkins, A. N. Poddubny, A. E. Miroshnichenko, and Y. S. Kivshar, “Circular dichroism induced by Fano resonances in planar chiral oligomers,” p. 23, Dec. 2014.

[164] Y. Zhao, M. A. Belkin, and A. Alù, “Twisted optical metamaterials for planarized ultrathin broadband circular polarizers.,” *Nat. Commun.*, vol. 3, p. 870, Jan. 2012.

[165] Y. Cui, L. Kang, S. Lan, S. Rodrigues, and W. Cai, “Giant chiral optical response from a twisted-arc metamaterial.,” *Nano Lett.*, vol. 14, no. 2, pp. 1021–1025, Feb.

2014.

[166] A. Ben-Moshe, S. G. Wolf, M. Bar Sadan, L. Houben, Z. Fan, A. O. Govorov, and G. Markovich, “Enantioselective control of lattice and shape chirality in inorganic nanostructures using chiral biomolecules.,” *Nat. Commun.*, vol. 5, p. 4302, Jan. 2014.

[167] A. Giugni, B. Torre, A. Toma, M. Francardi, M. Malerba, A. Alabastri, R. Proietti Zaccaria, M. I. Stockman, and E. Di Fabrizio, “Hot-electron nanoscopy using adiabatic compression of surface plasmons.,” *Nat. Nanotechnol.*, vol. 8, no. 11, pp. 845–852, Nov. 2013.

[168] N. K. Grady, J. E. Heyes, D. R. Chowdhury, Y. Zeng, M. T. Reiten, A. K. Azad, A. J. Taylor, D. A. R. Dalvit, and H.-T. Chen, “Terahertz Metamaterials for Linear Polarization Conversion and Anomalous Refraction,” *Science*, vol. 340, no. 6138, pp. 1304–1307, May 2013.

[169] D. Gu, C. Zhang, Y.-K. Wu, and L. J. Guo, “Ultrasmooth and thermally stable silver-based thin films with subnanometer roughness by aluminum doping.,” *ACS Nano*, vol. 8, no. 10, pp. 10343–10351, Oct. 2014.

[170] B. Desiatov, I. Goykhman, N. Mazurski, J. Shappir, J. B. Khurgin, and U. Levy, “Plasmonic enhanced silicon pyramids for internal photoemission Schottky detectors in the near-infrared regime,” *Optica*, vol. 2, no. 4, p. 335, Apr. 2015.

[171] Y.-J. Lu, J. Kim, H.-Y. Chen, C. Wu, N. Dabidian, C. E. Sanders, C.-Y. Wang, M.-Y. Lu, B.-H. Li, X. Qiu, W.-H. Chang, L.-J. Chen, G. Shvets, C.-K. Shih, and S. Gwo, “Plasmonic Nanolaser Using Epitaxially Grown Silver Film,” *Science*, vol. 337, no. 6093, pp. 450–453, Jul. 2012.

[172] A. A. High, R. C. Devlin, A. Dibos, M. Polking, D. S. Wild, J. Perczel, N. P. de Leon, M. D. Lukin, and H. Park, “Visible-frequency hyperbolic metasurface,” *Nature*, vol. 522, no. 7555, pp. 192–196, Jun. 2015.

[173] H. Harutyunyan, A. B. F. Martinson, D. Rosenmann, L. K. Khorashad, L. V Besteiro, A. O. Govorov, and G. P. Wiederrecht, “Anomalous ultrafast dynamics of hot plasmonic electrons in nanostructures with hot spots.,” *Nat. Nanotechnol.*, vol. advance on, Aug. 2015.

[174] K. Wu, J. Chen, J. R. McBride, and T. Lian, “Efficient hot-electron transfer by a plasmon-induced interfacial charge-transfer transition,” *Science*, vol. 349, no. 6248, pp. 632–635, Aug. 2015.

[175] F. Pelayo García de Arquer, A. Mihi, and G. Konstantatos, “Molecular interfaces for plasmonic hot electron photovoltaics.,” *Nanoscale*, vol. 7, no. 6, pp. 2281–8, Feb. 2015.

[176] K. Aydin, V. E. Ferry, R. M. Briggs, and H. A. Atwater, "Broadband polarization-independent resonant light absorption using ultrathin plasmonic super absorbers.," *Nat. Commun.*, vol. 2, p. 517, Jan. 2011.

[177] P. B. Johnson and R. W. Christy, "Optical Constants of the Noble Metals," *Phys. Rev. B*, vol. 6, no. 1970, pp. 4370–4379, 1972.

[178] P. Johnson and R. Christy, "Optical constants of transition metals: Ti, V, Cr, Mn, Fe, Co, Ni, and Pd," *Phys. Rev. B*, vol. 9, no. 12, pp. 5056–5070, 1974.

[179] V. Fedotov, P. Mladyonov, S. Prosvirnin, A. Rogacheva, Y. Chen, and N. Zheludev, "Asymmetric Propagation of Electromagnetic Waves through a Planar Chiral Structure," *Phys. Rev. Lett.*, vol. 97, no. 16, p. 167401, Oct. 2006.